Ultra-wideband Narrowband Interference Cancellation and Channel Modeling for Communications

Brian Michael Donlan

Thesis submitted to the Faculty of the
Virginia Polytechnic Institute and State University
in partial fulfillment of the requirements for the degree of

MASTER OF SCIENCE

in

Electrical Engineering

Dr. R. Michael Buehrer (Co-chair)
Dr. Jeffrey H. Reed (Co-chair)
Dr. Dong S. Ha

January 31, 2005
Blacksburg, Virginia

Keywords: Ultra-wideband, interference cancellation, transform domain processing, transversal filter, channel modeling

Ultra-wideband Narrowband Interference Cancellation and Channel Modeling for Communications

Brian Michael Donlan

(ABSTRACT)

Interest in Ultra-wideband (UWB) has surged since the FCC's approval of a First Report and Order in February 2002 which provides spectrum for the use of UWB in various application areas. Because of the extremely large bandwidth UWB is currently being touted as a solution for high data rate, short-range wireless networks. An integral part of designing systems for this application or any application is an understanding of the statistical nature of the wireless UWB channel. This thesis presents statistical characterizations for the large and small scale indoor channel. Specifically, for large scale modeling channel frequency dependence is investigated in order to justify the application of traditional narrowband path loss models to UWB signals. Average delay statistics and their distributions are also presented for small scale channel modeling.

The thesis also investigates narrowband interference cancellation. To protect legacy narrowband systems the FCC requires any UWB transmission to maintain a very low power spectral density. However, a UWB system may therefore be hampered by the presence of a higher power narrowband signal. Narrowband interferers have a much greater power spectral density than UWB signals and can negatively affect signal acquisition, demodulation, and ultimately lead to poor bit error performance. It is therefore desirable to mitigate any in-band narrowband interference. If the interferer's frequency is known then it may simply be removed using a notched filter. It is however of more interest to develop an adaptive solution capable of canceling interference at any frequency across the band. Solutions which are applied in the analog front end are preferable to digital backend solutions since the latter require extremely high rate sampling. The thesis therefore discusses two analog front-end interference cancellation techniques. The first technique digitally estimates the narrowband interference (this is possible because the UWB signal is not being sampled) and produces an RF estimate to perform the narrowband cancellation in the analog domain. Two estimation techniques, an LMS algorithm and a transversal filter, are compared according to their error performances. The second solution performs real-time Fourier analysis using transform domain processing. The signal is converted to the frequency domain using chirp Fourier transforms and filtered according to the UWB spectrum. This technique is also characterized in terms of bit error rate performance. Further discussion is provided on chirp filter bandwidths, center frequencies, and the applicability of the technology to UWB.

TABLE OF CONTENTS

LIST OF FIGURES

LIST OF TABLES

Chapter 1
Background and Motivation

1.1 Introduction

In February 2002 the Federal Communications Commission (FCC) approved a First Report and Order allowing the production and operation of unlicensed ultra-wideband (UWB) devices [FCC]. The report specified three target application areas and provided corresponding operating frequency ranges and power limitations. The application areas included vehicular radar systems, communications and measurement systems, and imaging systems. The imaging systems class consists of several radar implementations and is divided into the following subclasses: ground penetrating radar, wall imaging, through-wall imaging, medical and surveillance systems [FCC]. Of all the systems mentioned, measurement and communications systems are currently receiving the most attention in industry and academia alike. Communications and measurements are the focus of this thesis and all discussion henceforth will be in that context (Note that parts of the discussion will be applicable to other UWB systems as well.)

According to the FCC, a UWB system is classified using one of two different measures of bandwidth. A system can either have an instantaneous bandwidth in excess of 500 MHz or have a fractional bandwidth that exceeds 0.20 (by comparison a narrowband signal typically has a fractional bandwidth which is less than 0.01). Both metrics are defined according to the -10 dB points of the signal's spectrum. Fractional bandwidth is defined as the signal's bandwidth divided by its center frequency or more precisely as $BW_f = 2\frac{f_H - f_L}{f_H + f_L}$ where f_H is the highest frequency and f_L is the lowest frequency of the signal at the -10 dB points [FCC]. These definitions specify that systems with a center frequency greater than 2.5 GHz must have a bandwidth greater than 500 MHz and a system with a center frequency less than 2.5 GHz must have a fractional bandwidth greater than 0.20. Figure 1.1 below provides an illustration comparing the fractional bandwidth of a narrowband signal and a UWB signal, BW_{NB} is the narrowband signal bandwidth, BW_{UWB} is the UWB signal bandwidth, and f_c is the signal's center frequency.

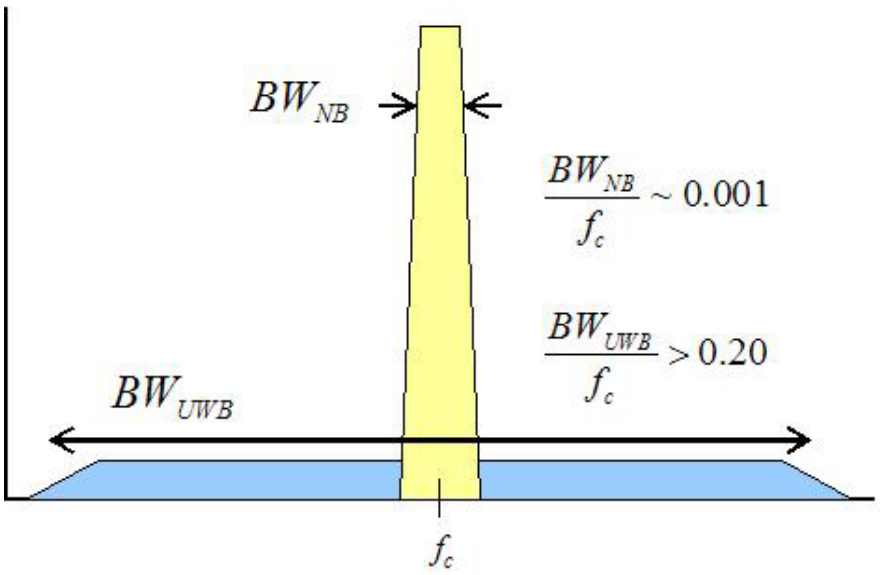

Figure 1.1 Fractional bandwidth comparison of a narrowband and UWB signal

As Figure 1.1 demonstrates a UWB signal's bandwidth can cover a large range of frequencies. It is therefore important that UWB devices use a low transmit power spectral density in order to not interfere with existing narrowband communications systems. For this reason the FCC has provided a preliminary "conservative" spectral mask for all UWB systems. The spectral mask for communications and measurement systems is given in Figure 1.2 below [FCC].

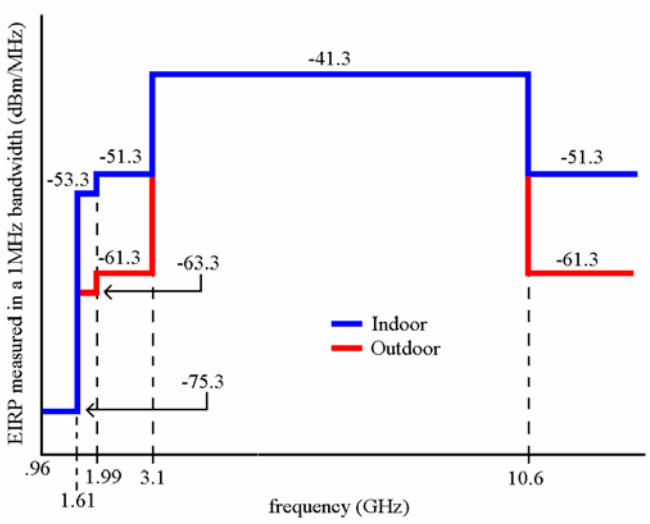

Figure 1.2 FCC Spectral Mask for Communications and Measurements Applications

1.2 Impulse Radio

The FCC's UWB classifications and specifications provide the opportunity for several technologies to be used for UWB communications applications. Specifically in the area of wireless personal area networks (WPAN), modulation techniques such as multi-band orthogonal frequency division multiplexing (OFDM) and a direct sequence version of the pulse based UWB (sometimes referred to as DS-UWB) are being considered for UWB devices. However these technologies have not traditionally been associated with UWB. UWB is typically synonymous with the transmission of ultra short duration (usually subnanosecond) pulses, with bandwidths in the gigahertz range. In fact, impulse radio and UWB radar have been in existence since the early 1970's. The use of these pulses provides many potential advantages for communications. First, the sharp "rise" and "fall" of the pulse causes the pulse's energy to be spread over a large bandwidth. This provides a low power spectral density for any given frequency and therefore provides the possibility for low probability of detection/intercept (LPD/I) communications. The narrow pulses also offer the capability for precise ranging and improved multipath resolution. This fine multipath resolution means that UWB is relatively immune to multipath fading and thus can have a much lower fading margin than traditional narrowband systems.

The following provides an introduction into the basics of pulse-based UWB or impulse radio. First some common UWB pulses are examined. Many researchers typically consider a Gaussian pulse or a derivative of the Gaussian pulse as the theoretical pulse shape for UWB communications systems. A Gaussian pulse can be simply described by the following function

$$p(t) = e^{-\frac{1}{2}(t/t_p)^2} \qquad -\infty < t < \infty \tag{1.1}$$

where t_p is approximately the width of the pulse in seconds. Figure 1.3 below displays an example of a Gaussian pulse with $t_p = 1\ ns$ and its corresponding magnitude spectrum. The -10 dB bandwidth of this signal is approximately 2 GHz.

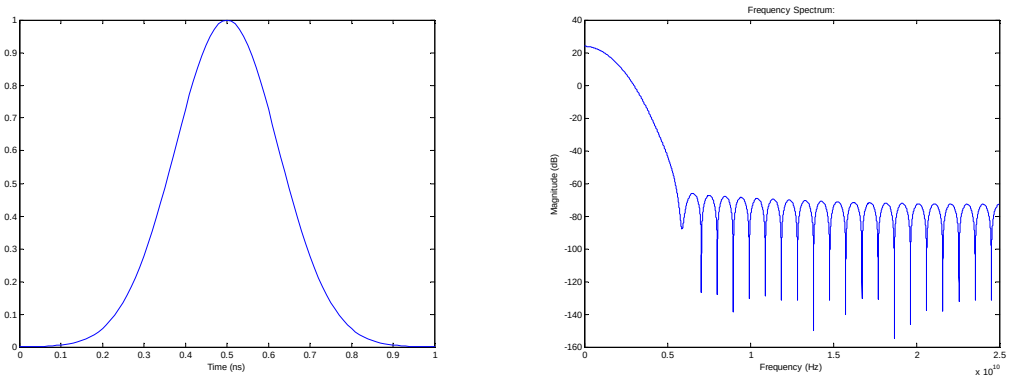

(a) (b)

Figure 1.3 (a) Gaussian Pulse and (b) Magnitude Spectrum

It is also of interest to consider the derivatives of the Gaussian pulse since it is possible to generate these pulses by filtering the original Gaussian pulse or through the use of wideband antennas. The antennas employed in a UWB system can have a significant impact on the shape of the UWB waveform and many times results in the differentiation of the generated pulse. For instance, because of the DC energy in the pulse shown above the transmitted version of this waveform would have a modified shape. Most wideband antennas have a lower cutoff frequency in the 100's of MHz and is one reason why transmitted pulses are sometimes differentiated. Antennas are an extremely important component of a UWB system and a great deal of consideration should be given to this area when designing a UWB system. A brief mention will be given concerning this in Chapter 2 but it is not the focus of the work presented. For a detailed analysis please see [Bueh04][Reed04]. Here we provide examples of the first and second derivatives of the Gaussian pulse which are given by

$$\frac{d}{dt}p(t) = \frac{t}{t_p^2} e^{-\frac{1}{2}(t/t_p)^2} \tag{1.2}$$

and

$$\frac{d}{dt^2}p(t) = \frac{1}{t_p^2} e^{-\frac{1}{2}(t/t_p)^2} - \frac{t^2}{t_p^4} e^{-\frac{1}{2}(t/t_p)^2} \tag{1.3}$$

Figures 1.4 and 1.5 provide example plots of the first and second derivatives with their corresponding magnitude spectrums, for t_p = *1 ns*. Here the -10 dB bandwidths are approximately 2.5 GHz and 2.7 GHz.

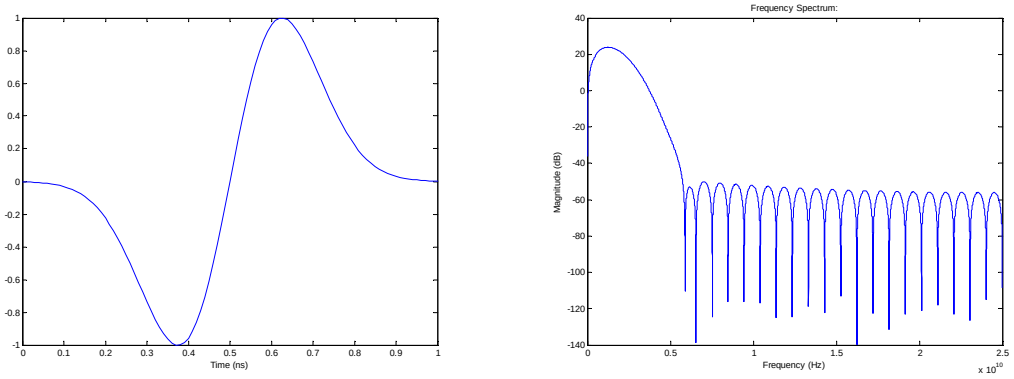

(a) (b)

Figure 1.4 (a) Gaussian Pulse First Derivative and (b) Magnitude Spectrum

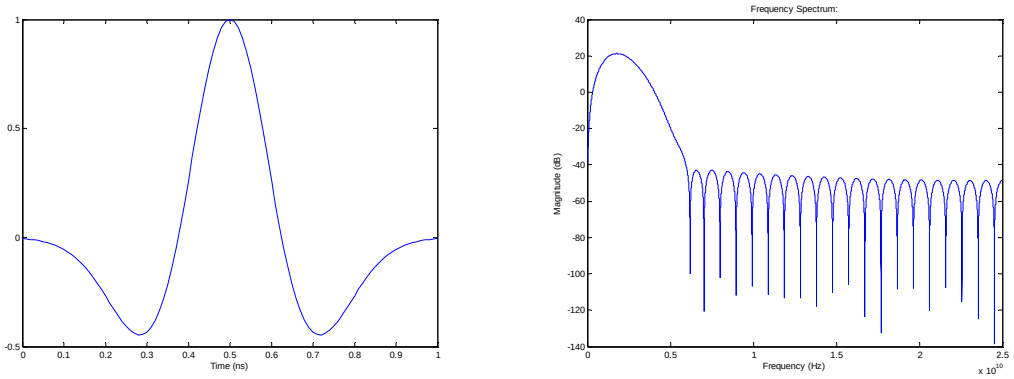

(a) (b)

Figure 1.5 (a) Gaussian Pulse Second Derivative and (b) Magnitude Spectrum

As shown in Figure 1.2, the FCC spectral mask specifies both the frequency range and power limitations for UWB communications devices. Therefore the baseband pulses in equations (1.1) – (1.3) could not be used for communications as they do not meet the 3.1-10.6 GHz specifications. However it is possible to modulate a sinusoid using a Gaussian pulse, shifting the pulse into the proper frequency range. Such an RF pulse can be described by

$$p(t) = e^{-\frac{1}{2}(t/t_p)^2} \cdot \sin\left(2\pi f_{c,UWB} t\right) \tag{1.4}$$

where $f_{c,UWB}$ is the center frequency of the RF pulse. Figure 1.6 gives an example of the RF pulse and its corresponding spectrum for $t_p = 1\ ns$ and $f_{c,UWB} = 6\ GHz$. The -10 dB bandwidth for this pulse is approximately from 4 – 8 GHz.

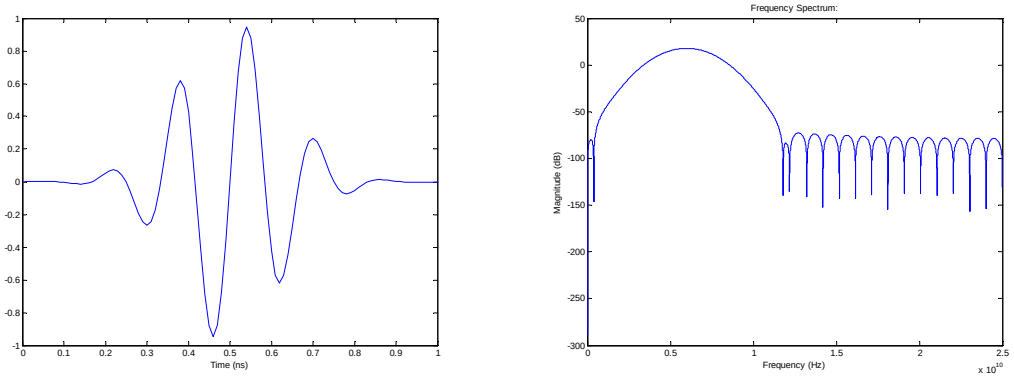

(a) (b)

Figure 1.6 (a) Gaussian Modulated RF Pulse and (b) Spectrum

1.3 Modulation

Any of the pulses described in equations (1.1) – (1.3) can be incorporated into several different *M*-ary or binary modulation schemes. Of the many possible modulation techniques, two are predominately considered in research and industry. These are pulse position modulation (PPM) and biphase modulation. Note that biphase is somewhat of a misnomer as a baseband Gaussian pulse does not have a phase parameter associated with it, just polarity.

PPM is an *M*-ary modulation format that conveys information using pulses placed at specified delays. This modulation scheme is typically orthogonal and in the binary case its performance is identical to binary frequency shift keying (BFSK) in a purely AWGN channel. Consider Figure 1.7 which gives an illustration of 4-ary PPM modulation. Here T_c is associated with the amount time allocated to transmit one UWB pulse. T_c is therefore divided into M (in this case 4) different time slots of width δ. The bit or symbol which is being transmitted determines which time slot the pulse occupies.

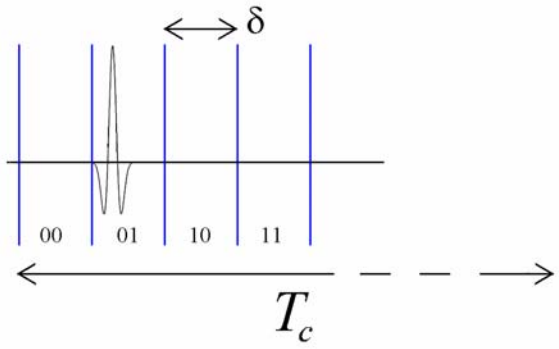

Figure 1.7 4-ary Pulse Position Modulation (PPM)

The other prevalent modulation format, biphase, is strictly a binary scheme and encodes information into the polarity of the pulse. Biphase is therefore antipodal and in a purely AWGN channel has error performance that is identical to binary phase shift keying (BPSK). Figure 1.8 provides an illustration of biphase modulation where a negative pulse represents a 0 and a positive pulse represents a 1.

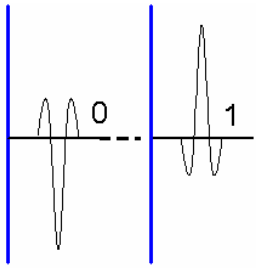

Figure 1.8 Biphase Modulation

It is also worth mentioning several other possible UWB modulation techniques. These include pulse amplitude modulation (PAM) and on-off keying (OOK). PAM is an *M*-ary modulation format where the information is encoded into the amplitude of the pulse. Figure 1.9 gives an example of 4-ary PAM. PAM however is not a particularly attractive modulation scheme since it is increasingly energy inefficient with increasing *M* and UWB systems are typically power limited. Another possible modulation type, OOK, is a binary scheme. In this case the presence or absence of a pulse determines whether a 1 or a 0 was sent. This technique is also not very energy efficient but may be attractive for a low cost, low complexity system. Figure 1.10 provides an example of OOK.

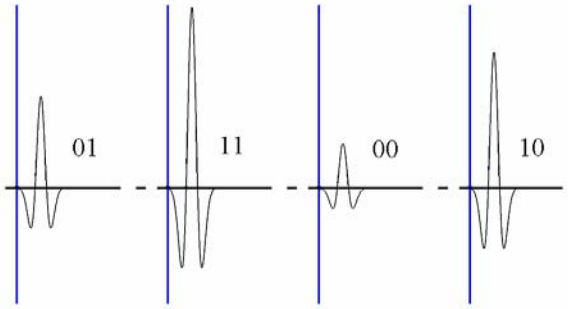

Figure 1.9 4-ary Pulse Amplitude Modulation (PAM)

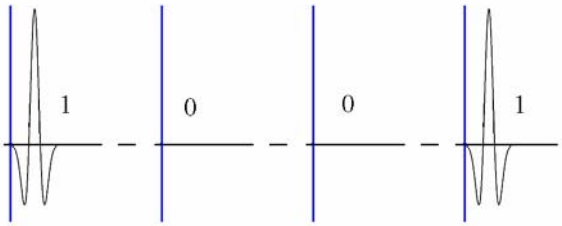

Figure 1.10 On-Off Keying Modulation (OOK)

1.4 Multiple Access

Some system designs also incorporate time hopping to provide multiple access (time hopping also provides some other advantages which will be discussed shortly). Time hopping is variation of traditional time division multiple access (TDMA). In traditional TDMA a frame is divided into N time slots allowing N users to share a single link. A user is assigned a time slot and transmits in the same time slot each frame. Time hopping adds a variation to this by changing the time slot from frame to frame according to the user's code. Also when used with UWB more than one pulse is typically used to represent a data symbol. Note that frequency division multiple access (FDMA) is impractical for UWB systems. The large bandwidths of UWB signals preclude this option and would also result in a much more complicated receiver design. Any of the above modulation types could be used in conjunction with time hopping but PPM is

typically considered in the literature and will be the basis of the following discussion. An example of a time hopping PPM (TH-PPM) system was presented in [Mart02][McKi03a] and is given by

$$s^{(k)}(t) = \sum_j A\, p\left(t - jT_f - c_j^{(k)}T_c - \delta d_{[j/N_s]}^{(k)}\right) \tag{1.5}$$

where

- $s^{(k)}(t)$ is the transmitted signal for the k^{th} user
- A is the amplitude of the pulse, equal to $\sqrt{E_p}$ where E_p is the energy per pulse,
- N_s is the number of pulses used to represent one data symbol, i.e. the pulse repetition number
- $p()$ is the received pulse shape with normalized energy (this assumes all pulses received have experienced the same distortion due to the channel),
- T_f is the frame repetition time (a UWB frame is defined as the time interval in which one pulse is transmitted),
- $c_j^{(k)}$ is the time hopping sequence, often pseudorandom and/or repetitive,
- T_c is the granularity of the time hop delay (together $c_j^{(k)}$ and T_c determine the 'coarse' time dithering)
- δ is the PPM time delay parameter, and
- $d_{[\ ]}^{(k)}$ is a function of the data sequence (the [ ] notation represents the integer portion of the argument).

The total received signal is given by

$$r(t) = \sum_k s^{(k)}(t) * h^{(k)}(t) \tag{1.6}$$

where $h^{(k)}(t)$ is the channel impulse response between the k-th user and the receiver of interest [McKi03a].

Figure 1.11 provides a depiction of an undmodulated pulse train without time hopping in which the frame, T_f, represents the time between pulses and T_p represents the pulse width.

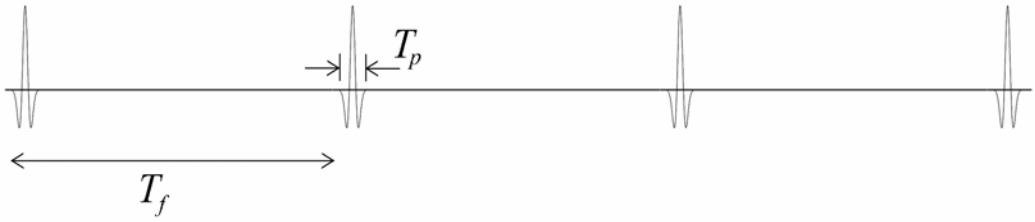

Figure 1.11 UWB Pulse Train (no modulation and no time hopping)

In contrast, Figure 1.12 provides an example of a time hopping frame where T_f is considered the time in which one pulse is sent and is divided into time slots of period T_c. Relating back to the earlier discussion of PPM T_c is the same as depicted in Figure 1.7. A pulse is then transmitted in any one of the time slots. In a multiple access scenario the k^{th} user would have a unique code, $c_j^{(k)}$, which is usually pseudorandom, and specifies the

time hopping location of the pulse from frame to frame. Modulation then occurs independently within the time slot. Note that if synchronization were possible then orthogonal codes could be used. Regarding modulation, the variable N_s specifies the number of pulses that are used to transmit one symbol or bit. Using $N_s > 1$ introduces time diversity over the period of one symbol. This provides the system with a processing or spreading gain equal to N_s. This in turn improves the ability to properly detect a symbol for a given received power at the cost of reducing the data rate.

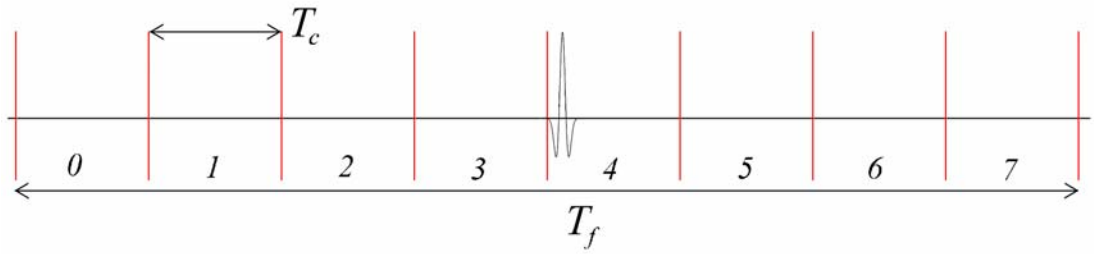

Figure 1.12 Example Frame for Time Hopping UWB

As previously stated, time hopping actually serves a dual purpose. Besides multiple access, it can also be used to smooth the spectrum of the UWB pulse. Consider again the pulse train represented in Figure 1.11. Because of the periodic nature of the pulse train, transmitting a signal of this nature introduces spectral lines in the pulse's spectrum. Figure 1.13 provides an example of such a signal's spectrum. In contrast Figure 1.14 shows the spectrum of a time hopped sequence created using 16 different time slots. Observing Figure 1.13(a) and Figure 1.14 there is a noticeable difference in the magnitude of the pulse train's spectrum. By employing time hopping the periodicities can be greatly reduced.

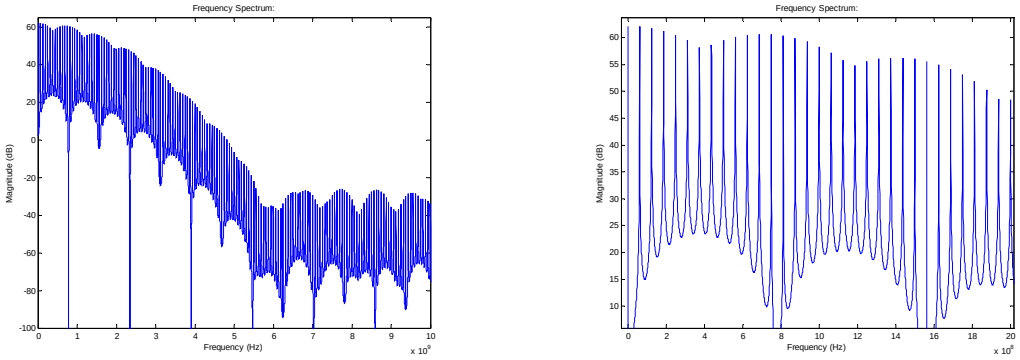

Figure 1.13 (a) Spectrum of Undithered Pulse Train and (b) a Magnified Portion of the Spectrum

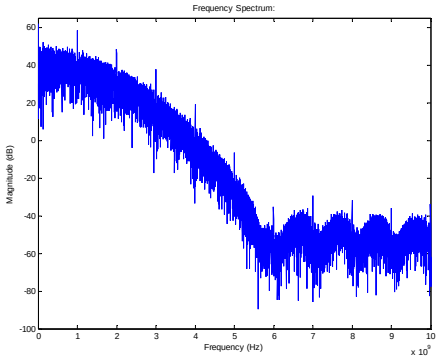

Figure 1.14 Spectrum of Time Hopped Pulse Train

Another possible UWB multiple access technique is direct sequence spread spectrum (DS-SS), sometimes called DS-UWB. DS-UWB is similar in principle to more traditional DS-SS systems such as cellular CDMA (code division multiple access). Note that time-hopping is also a type of CDMA since codes are used to separate user. DS-UWB based CDMA uses a binary pseudo-random code, typically with good cross correlation properties, to facilitate multiple access. Each user is therefore assigned a unique pseudo-random code and multiple access is achieved by correlating the received signal with the correct pseudo-random code. Note that pseudo-random codes are also used with time hopping but the codes are not typically binary sequences. In DS-UWB the code is used to modulate a stream of UWB pulses using biphase modulation. Note that since this is a form a spread spectrum (i.e. a large number of pulses are being used to represent a single bit) it also offers some interference suppression since the pulse is "compressed" when the code is correlated at the receiver (The same holds true for time-hopping if multiple pulses are used per data symbol).

1.5 Interference

Lastly, a brief commentary is provided on the interference inflicted and observed by a UWB system. As shown by the spectral mask given in Figure 1.2, UWB communications systems are required to maintain a low transmit power spectral density. This is primarily a criterion to protect legacy narrowband systems, especially GPS and navigation systems. The interference seen by a narrowband system is expected to be minor especially since a majority of the UWB signal's energy is outside of the narrowband signal's bandwidth. There have been several research efforts investigating the impact of a UWB signal on existing systems. [Ligh03] presented test results examining the effects of UWB signals on many different legacy military systems. They found that UWB transmissions did interfere with some devices more than others and that many factors impact the level of interference, including pulse shape and pulse repetition frequency. They found that some devices were susceptible to interference at power spectral densities below the FCC spectral mask. One of the biggest concerns is the impact of UWB on GPS since air traffic relies heavily on this technology. For this reason no UWB transmissions are currently allowed in the spectrum allocated to GPS. The bottom line is there still needs to be much characterization done in this area.

Regardless of future changes to the spectral mask, UWB will still be susceptible to interference from in-band narrowband systems and hence will suffer from limited range. There will therefore likely be the need for signal processing techniques which perform front end interference cancellation. Since the problem is similar to that of spread spectrum hopefully there will be some crossover from previous spread spectrum front end interference cancellation techniques. Spread spectrum has received considerable research attention and will hopefully offer numerous ideas. Unfortunately techniques such as linear prediction filters, which are purely digital, are not yet viable solutions since the current state of the art does not allow for a cost effective entirely digital UWB system. Some possible solutions include the use of transform domain processing, a combination analog-digital cancellation circuit, the use of antenna arrays, and the use of Rake receivers to exploit the temporal diversity of the UWB channel. Explicit interference cancellation focuses on front end techniques because narrowband interference could easily prevent signal acquisition. Without acquisition traditional spread spectrum rejection techniques can not be applied. Currently there are no existing techniques which are employed in UWB systems and investigations of such techniques are just beginning to appear in the literature. This is discussed in greater detail in later chapters and is a major portion of the work presented here.

1.6 Thesis Outline

The crux of this thesis focuses on two subject areas related to UWB radio performance, channel modeling and interference cancellation. Chapter 2 discusses analysis conducted on UWB indoor propagation measurements, focusing specifically on large scale modeling. The effect of bandwidth is discussed as it relates to path loss, and general path loss statistics are discussed. Chapter 3 discusses narrowband interference and its affects on a UWB signal, and introduces existing cancellation techniques, predominately in the context of spread spectrum. The interference cancellation sections discuss two different front end interference cancellation techniques. Chapter 4 concentrates on a combination analog and digital cancellation circuit. The circuit uses a digital algorithm to estimate the narrowband interference and subsequently cancels it in the analog domain. Both a least-mean-squares (LMS) and a two-sided transversal filter are investigated. Chapter 5 analyzes transform domain processing using chirp filters. This is a purely analog technique and is also performed in the front end. The received signals are transformed into the “frequency” domain allowing the narrowband energy contribution to be cancelled. Finally Chapter 6 provides conclusions and the direction of future work.

Chapter 2
Ultra-Wideband Channel Modeling

2.1 Introduction

Accurate channel models are extremely important for efficient communication system design. The calculation of large and small scale statistics facilitates the creation of such a model. Specifically large scale models are necessary for network planning and link budget design and small scale models are necessary for efficient receiver design. This chapter discusses the statistical characterization and modeling of the Ultra-Wideband (UWB) indoor channel based on a recent measurement campaign as part of the DARPA NETEX program [Muqa03a][Bueh03][Bueh04][Reed04][Donl05][McKi03a].

Many researchers have presented UWB measurement results investigating both the residential and office environments. Ghassemazdeh and Tarokh reported line-of-sight (LOS) and non-line-of-sight (NLOS) path loss results for a residential environment using a vector network analyzer (VNA) [Ghas03] for a frequency range from 4.375 – 5.625 GHz. Rusch et. al. also investigated the residential setting, presenting large and small scale, LOS and NLOS results for 2-8 GHz [Rusc04]. Other campaigns investigated the indoor office environment. Kunisch and Pamp's measurements used a VNA to investigate the frequency range from of 1-11 GHz, reporting path loss and amplitude statistics for LOS and NLOS environments [Kuni02]. Yano reported large and small scale findings using a time domain (pulse) measurement system with a center frequency of 2 GHz and a bandwidth of 1.5 GHz [Yano02]. Cassoli, Win, and Molisch also presented large and small scale results using a time domain measurement system [Cass02]. There are many other existing measurement results including [Alva03], [Hovi02], [Keig03], and [Paga03]. The current work is based on both time domain and to a lesser extent frequency domain measurements from the DARPA NETEX project. We build on the existing work by (a) providing additional measurement results, (b) providing a detailed discussion of path loss for UWB, (c) discussing link budget ramifications, and (d) examining the impact of the common tap delay line small scale modeling approach.

Note that statistics for a large part of the data used in this work was previously presented in [Muqa03a]. The current work differs in several ways. First, the previous large scale characterization, did not examine frequency depdendency and used a different reference point (i.e., included multipath in the reference). Secondly, the current work discusses in some detail the applicability of the Friis transmission formula to UWB path loss calculations and link budget concerns for UWB. Additionally, the current small scale characterization is based on an assumption of a discrete channel model, whereas [Muqa03a] simply examined the continuous time impulse response. Thus, we consider

additional information such as the number of paths seen in the channel, the impact of discrete channel modeling assumptions and the energy capture of different receiver structures. Finally, it should be noted that the data set considered here is is approximately 25% larger than the data set presented in [Muqa03a] due to additional measurements being taken by the authors.

Section 2.2 provides a brief introduction to the data set and the measurement procedure. Section 2.3 discusses large scale channel modeling, presents the motivation and justification for the path loss model used and provides the path loss results. Section 2.4 describes the analysis methodology and results for the small scale statistics. Additionally, the impact of the discrete channel model assumption on the results is also discussed. Section V presents conclusions.

2.2 Measurement Procedure

The indoor measurement data represents various indoor LOS and NLOS environments. Measurements were taken with both a wideband biconical and a TEM horn antenna. Additionally, both time domain and frequency domain measurements were taken using a digital sampling oscilloscope and vector network analyzer respectively. A large portion of the time domain measurements and all the frequency domain measurements were conducted by Virginia Tech's Time Domain Laboratory (TDL). For a complete description of their measurement procedure and locations see [Muqa03a][Bueh04]. The additional measurements associated with this thesis, taken by the author and Vivek Bharadwaj, are now described in detail.

Time domain indoor NLOS measurements were taken as part of the DARPA NETEX project. These measurements supplement the measurements taken by TDL and together they are the foundation of the analysis presented in this chapter.

The measurements were taken using a Tektronix CSA 800 Digital Sampling Oscilloscope (DSO), a Gaussian pulse generator, and two wideband Bicone antennas. The setup is diagrammed in Figure 2.1.

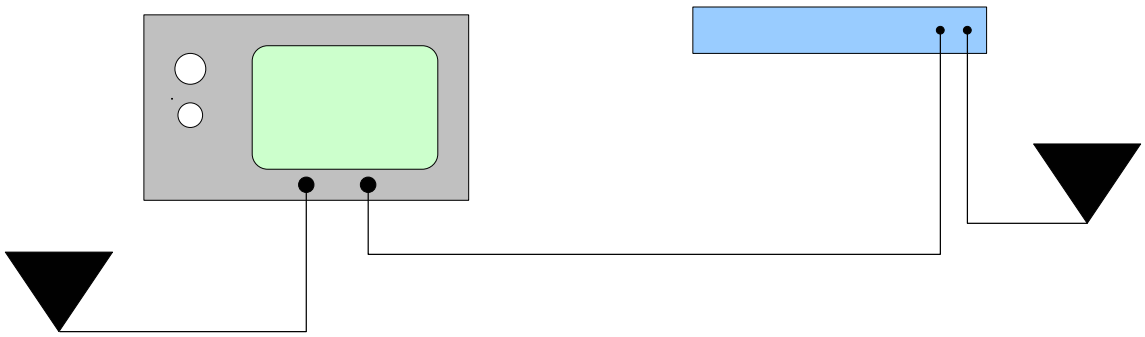

Figure 2.1 Measurement Setup

The Gaussian pulse generator is manufactured by Picosecond Labs. The pulse generator allows control of the pulse repetition frequency and also generates a trigger signal. The trigger signal generation is synchronized with the pulse generation and is therefore used by the DSO as a reference to begin recording samples. The trigger signal is used by the DSO to perform averaging and therefore must be very stable. The averaging is performed on successive received signals thus is contingent on having a good reference. This averaging improves the overall SNR of the recorded signal.

Measurements were taken at various NLOS locations throughout the MPRG student lab in Durham Hall. A single measurement location consisted of a group of local area measurements taken on a 1-m by 1-m grid. The points on the grid were separated by 15 cm in both the horizontal and vertical direction and contained a total of 49 points. A measurement record was therefore taken at each point and record consisted of 100 ns worth of data sampled at an effective rate of 400 GHz. Note that these measurements were taken in the evening to provide as static an environment as possible.

The two antennas used, the TEM and Bicone, affect the received pulse shape and spectrum in unique ways. Here we summarize the antenna effects with respect to the indoor measurements and modeling. The generated is Gaussian in shape with a pulse width of approximately of 200 picoseconds. The 10 dB point of the resulting spectrum is approximately 7 GHz. Figure 2.2 and Figure 2.3 provide the time domain generated pulse and magnitude spectrum, respectively.

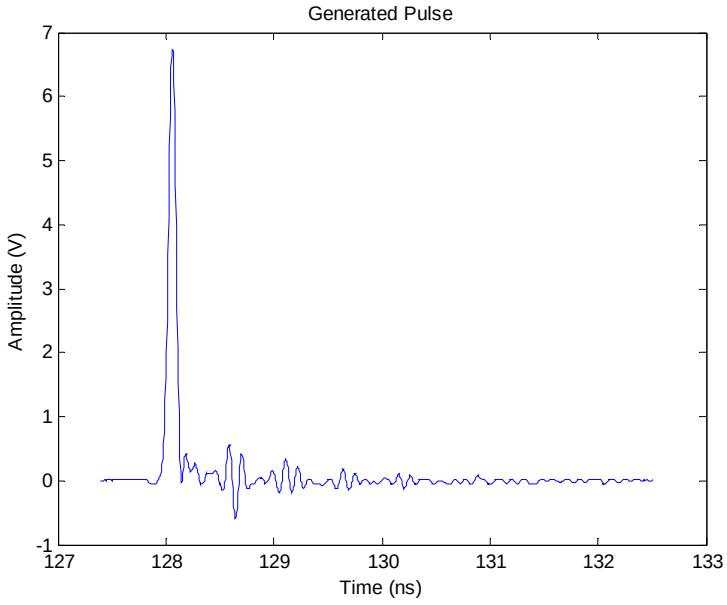

Figure 2.2 Generated Gaussian Pulse

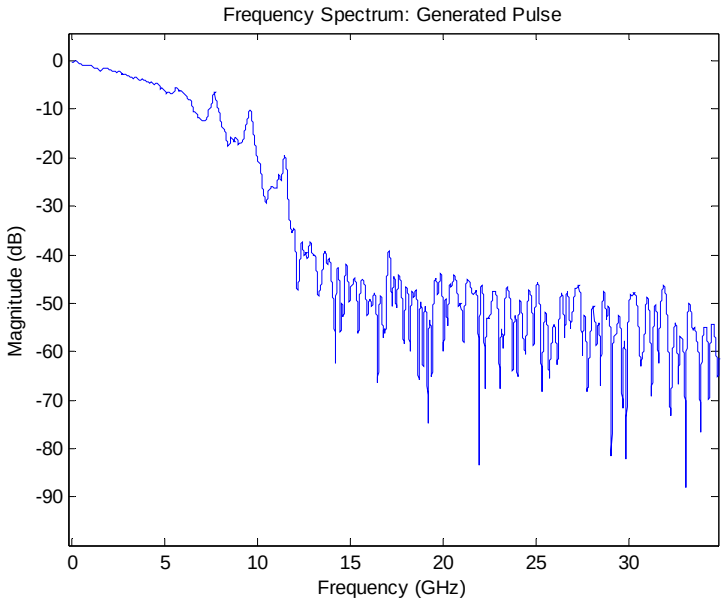

Figure 2.3 Generated Gaussian Pulse Spectrum

The received LOS pulse may have a different shape than this generated pulse based on the antennas used in the system. The measurements presented here were conducted using similar antennas at the transmitter and receiver. With the Bicone antennas the received pulse was observed to be a partial derivative of the generated pulse and for the TEM horn antennas the received pulse was observed to be the derivative of the generated pulse. This pulse distortion impacts both path loss calculations and the extraction of the channel impulse response using the CLEAN algorithm (the CLEAN algorithm is described in [McKi03a][Hogb74]). Consequently a separate LOS measurement, containing only a single path, is needed for each antenna configuration and is used for both the large and small scale calculations. These LOS pulses were extracted from reference measurements taken at a distance of 1 meter. The LOS measurements for the Bicone and TEM antennas are given in Figure 2.4 and 2.5 respectively.

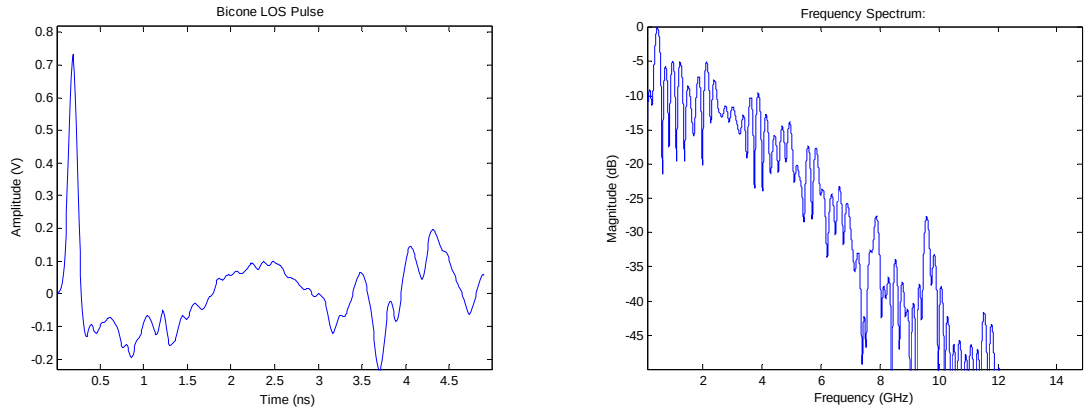

(a) (b)

Figure 2.4 (a) Bicone LOS Received Pulse and (b) Magnitude Spectrum

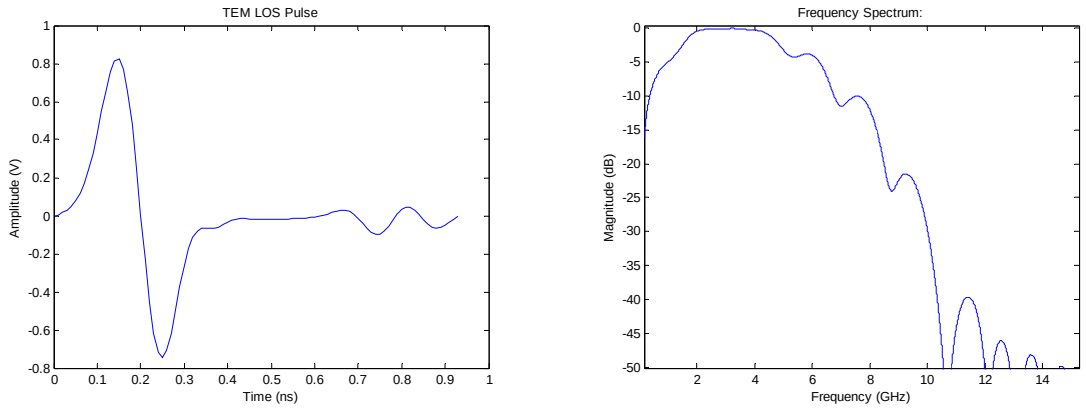

(a) (b)

Figure 2.5 (a) TEM LOS Received Pulse and (b) Magnitude Spectrum

2.3 Large Scale Channel Modeling

Path loss is a fundamental characteristic of electromagnetic wave propagation and is used in system design (i.e. link budgets), in order to predict system coverage. Traditionally path loss is examined using the Friis Transmission Formula which provides a means for predicting the received power. The formula in general predicts that received signal power will decrease with the square of increasing frequency, which has little effect on narrowband systems. However, the large bandwidths of ultra-wideband (UWB) signals (typically > 500 MHz), coupled with the general form of the Friis Transmission Formula, would tend to suggest that the channel will introduce frequency dependent distortion and thus distort the pulse shape. Thus the Friis Transmission Formula needs to be examined more closely to justify its application to UWB.

The Friis transmission formula is based on the flux density of a transmitting source.

The flux density is given by

$$F = \frac{EIRP}{4\pi d^2} \qquad watts/m^2 \tag{2.1}$$

where *EIRP* is the Effective Isotropic Radiated Power, which assumes that the power is radiated equally in all directions by the transmitter, and *d* is the radius of the sphere for which the flux density is being calculated.

Equation (2.1) illustrates that the flux density assumes no frequency dependence and shows that with a doubling of distance the flux decreases by a factor of four. This flux density can then be used to determine received power, P_r, by multiplying by A_e, the effective aperture of the receive antenna resulting in

$$P_r = \frac{EIRP}{4\pi d^2} A_e \qquad watts \tag{2.2}$$

The Friis formula is typically quoted in terms of the gains of the antennas where the gain is related to the antenna's effective aperture, A_e, by

$$G = \frac{4\pi}{\lambda^2} A_e \tag{2.3}$$

Rearranging (2.3) by solving for A_e, and substituting the result into (2.2) gives

$$P_r = \frac{EIRP}{4\pi d^2}\left(\frac{\lambda^2}{4\pi}\right) G_r = EIRP \cdot G_r \left(\frac{\lambda}{4\pi d}\right)^2 \tag{2.4}$$

Further, EIRP can be expressed as

$$EIRP = P_t G_t \tag{2.5}$$

where P_t, is the transmit power and G_t, is transmit antenna gain. This results in the standard Friis Transmission Formula given as

$$P_r = \frac{P_t G_t G_t \lambda^2}{(4\pi d)^2} \tag{2.6}$$

The term $\left(\frac{\lambda}{4\pi d}\right)^2$ is typically termed the path loss. The existence of λ in the path loss equation is thus interpreted as frequency dependence in the path loss. However, this term is explicitly an antenna effect. To make this more obvious, it is instructive to consider another type of antenna, a constant aperture antenna. A constant aperture antenna has a flux density which is a function of wavelength given as .

$$F = P_t\left(\frac{4\pi A_{et}}{\lambda^2}\right)\left(\frac{1}{4\pi d^2}\right) = \frac{P_t A_{et}}{\lambda^2 d^2} \qquad watts/m^2 \tag{2.7}$$

This flux density can be used in the same manner as above to obtain the expected received power:

$$P_r = P_t A_{et}\left(\frac{1}{\lambda d}\right)^2 A_{er} \tag{2.8}$$

This result shows frequency dependence, but here the received power increases with frequency. For systems with a constant gain antenna on one end of the link and a constant aperture antenna on the other end of the link, the received power can be shown to be independent of frequency [Bueh03]. The bottom line in this analysis is that while the received power may be dependent on frequency, the path loss (or more accurately the spreading loss) is not. Frequency dependence is an antenna effect. To verify this result, LOS measurements were taken to examine the received signal power, and consequently path loss with distance. The first measurements consider a case most closely related to equation (1-6). Wideband biconical antennas can be considered to be roughly constant gain over the frequency band of interest and were used in many of the measurements. The second set of measurements used TEM horn antennas at both the transmitter and receiver. This scenario is somewhere between constant gain and constant aperture antennas. Both analyses used frequency domain measurements, taken using a vector network analyzer, and time domain measurements, taken using a digital sampling scope. The measurement procedures are described in [Muqa03a].

Figure 2.6 compares a group of received time domain LOS pulses using biconical antennas. This plot shows received time domain voltage signals that are normalized

according to their respective distances[1]. It is expected that if no frequency dependence exists in the path then all the pulses will retain the same pulse shape. A few pulses exhibit slight variations but otherwise the pulses do indeed maintain the same shape. A complimentary analysis was performed in the frequency domain by comparing the slope of the received power for several frequency domain measurements of increasing distance. This is depicted in Figure 2.7. The slopes reveal that there is a frequency dependence in the received power as predicted by the Friis equation in (2.6). However this dependence is consistent across all distances examined. Thus we conclude that the frequency dependence is related to the antenna in the LOS channel.

This analysis was repeated for the TEM horn antennas producing similar results. Figure 2.8 plots several timed domain LOS TEM pulses that are normalized according to their respective distances. As with the Bicone case, no distortion is observed. Again an analysis was performed in the frequency domain. Figure 2.9 plots the slope of the received power for several distances. The measurement taken at 14 m is a little noisy but in general the slopes are similar.

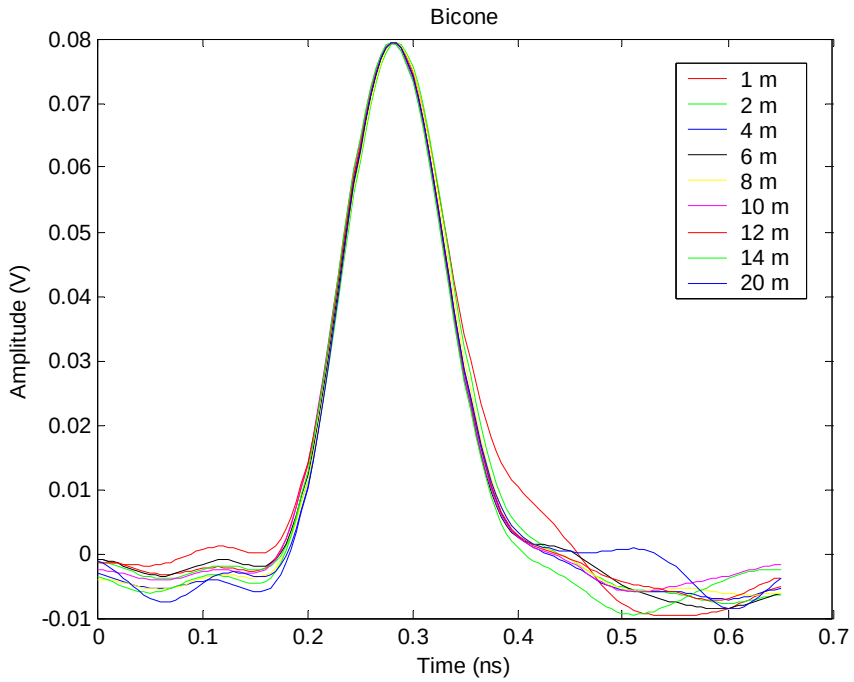

Figure 2.6 LOS Received Pulses Normalized According to Their Respective Distances Using Bicone Antennas

[1] Since power spreading loss is relative to the square of distance, the loss in voltage is expected to be relative to distance. Thus, normalizing the received signal values with respect to distance should result in similar voltage levels.

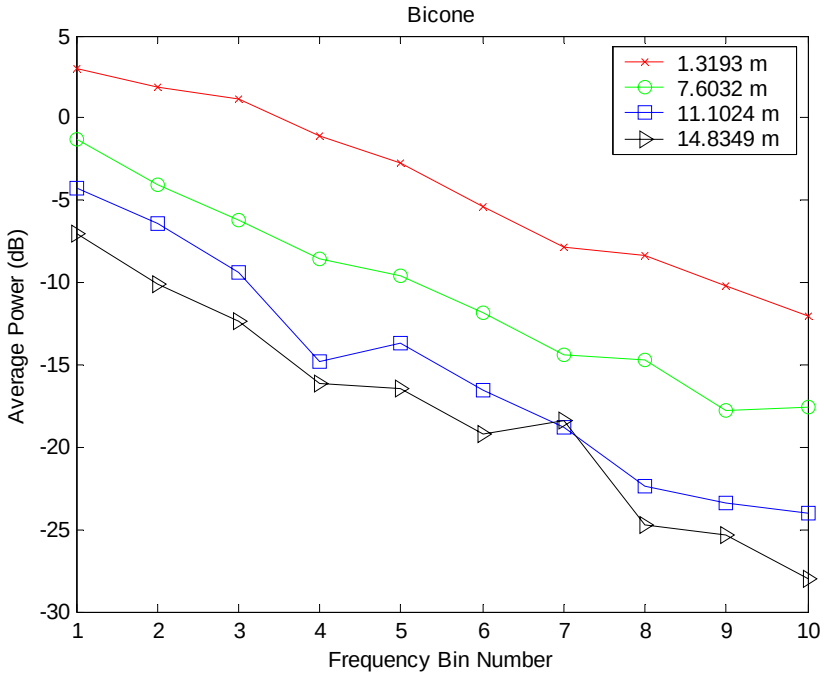

Figure 2.7 Example Received Powers for Frequency Domain Measurements at Different Distances Using Bicone Antennas (in 1 GHz increments)

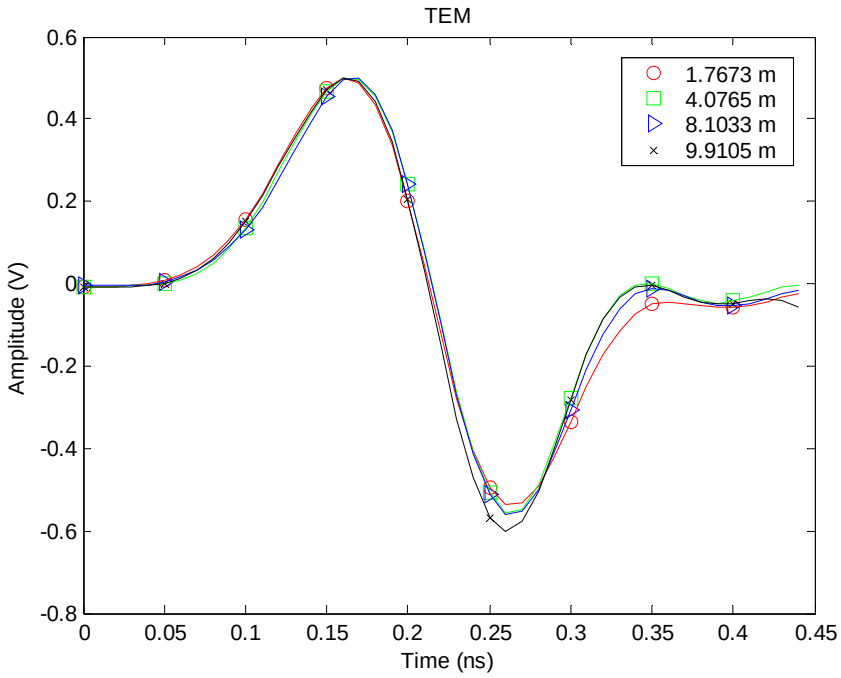

Figure 2.8 LOS Received Pulses Normalized According to Their Respective Distances Using TEM Antennas

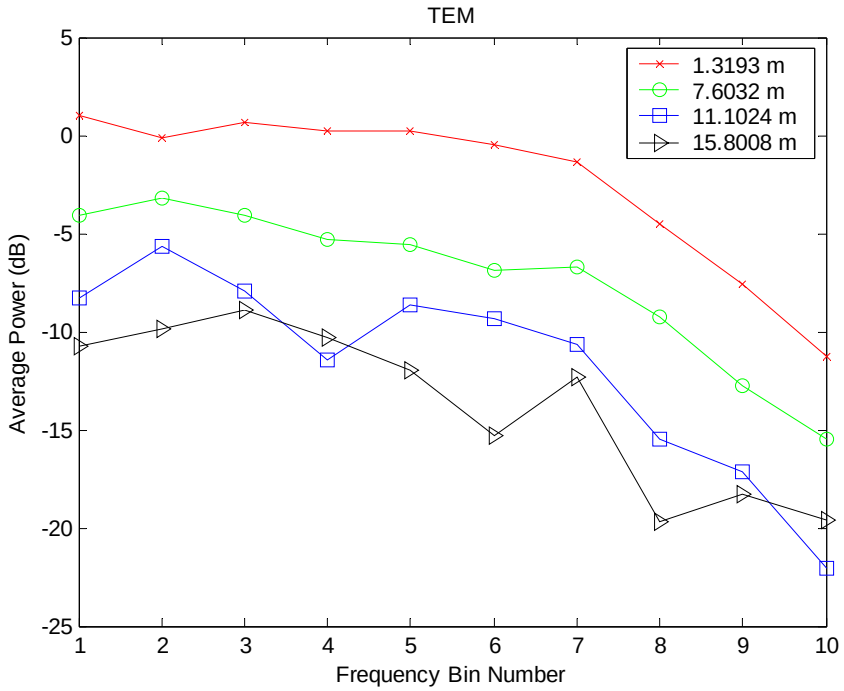

Figure 2.9 Example Received Powers for Frequency Domain Measurements of Different Distances Using TEM Horn Antennas (in 1 GHz increments)

It is also of interest to examine an NLOS scenario. The NLOS environment provides the opportunity for substantial pulse interaction, frequency selective fading and the introduction of frequency dependence into the path loss. Examining and comparing the slopes of LOS and NLOS measurements should provide some insight into NLOS frequency dependence.

Figure 2.10 and Figure 2.11 show the averaged received power versus frequency for the wideband biconical antennas (this average is taken over all the time domain measurements). Note that the slope of the received power versus frequency is different than that given in Figure 2.6. This is because the current plot includes both the effect of the antenna as well as the pulse used for the time domain measurements. However, examining the slopes of these two plots (LOS and NLOS) reveals that they are very similar. This suggests that the NLOS measurements experience the same frequency dependence as the LOS measurements. Based on the conclusion that LOS frequency dependence is antenna induced and not channel induced, we can further conclude that the NLOS channel also does not exhibit frequency dependence[2]. We should emphasize that the NLOS measurements were taken at relatively short distances (< 10m). It is very possible that larger distances may reveal frequency dependencies for NLOS channels due to the frequency dependence of many materials.

[2] It should be emphasized that we are talking about the received power versus distance averaged over many measurements. It is certainly true that frequency selective fading will occur on any individual measurement.

A similar analysis was performed for the TEM horn antennas. Figure 2.12 and Figure 2.13 show the slope of the averaged received power versus frequency. There is a slight variation in the shape of the frequency spectrum and slope but in general they are very similar. This again suggests that NLOS path loss does not suffer substantially from frequency dependence. We will revist this conclusion shortly. At this point we simply emphasize that the dominant source of frequency dependence in the averaged received signal power is due to the antennas rather than the path.

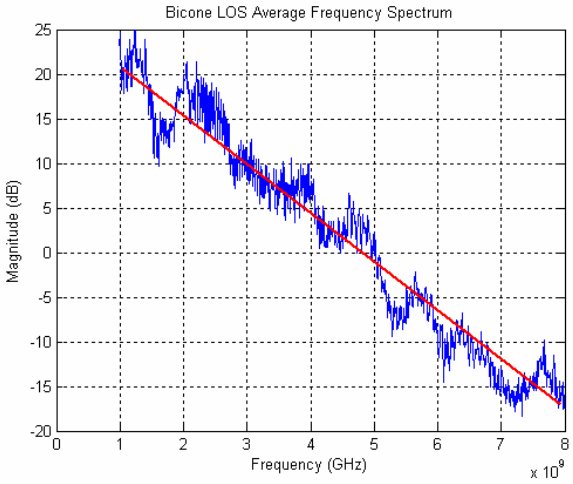

Figure 2.10 Bicone LOS Average Received Power vs. Frequency

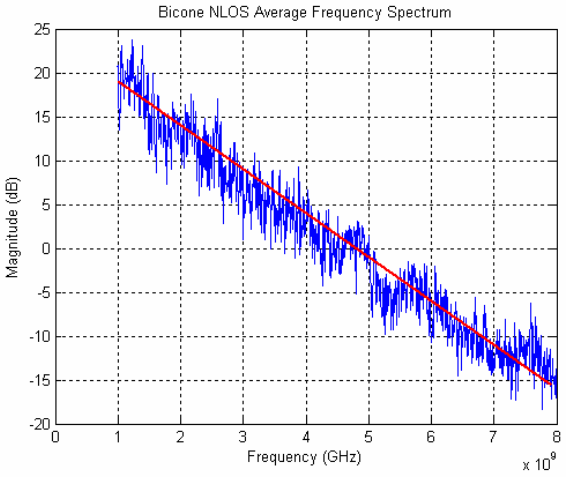

Figure 2.11 Bicone NLOS Average Received Power vs. Frequency

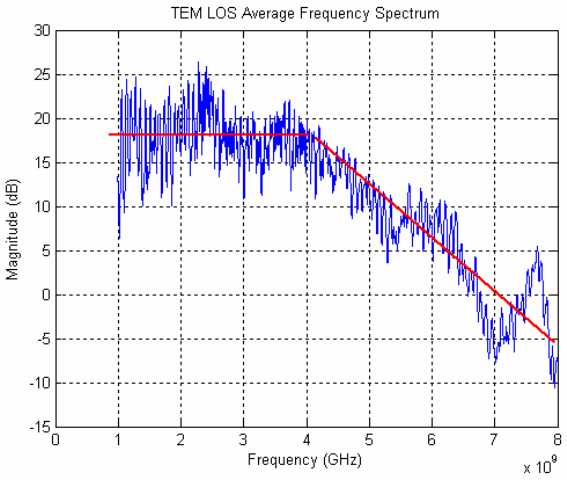

Figure 2.12 TEM LOS Averaged Received Power vs. Frequency

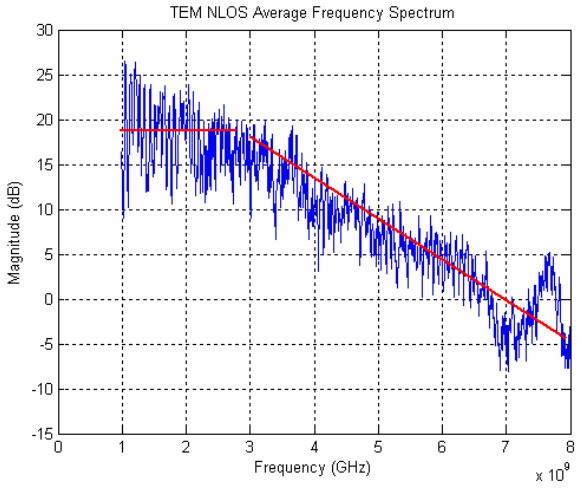

Figure 2.13 TEM NLOS Averaged Received Power vs. Frequency

2.3.1 Empirical Modeling

Section 2.3 provides justification for applying the traditional path loss model to the analysis of UWB signals. In other words, since path loss is not inherently frequency

dependent, the traditional narrowband models apply. Specifically traditional empirical models examine the path loss relative to a reference point. Since the frequency dependent effects will be captured in the reference measurement the standard model is applicable. The following provides analysis and results for measurements taken in the time domain and frequency domain for LOS and NLOS scenarios.

It is has been shown in many experiments and with theoretical models that the average path loss (both indoors and outdoors) increases exponentially with distance [Rapp02]:

$$\overline{PL}(d) \propto \left(\frac{d}{d_o}\right)^n \tag{2.9}$$

where d_o is a reference distance (typically 1m for indoor measurements). Specifically, the average received power can be modeled as

$$\overline{P_r}(d) = \overline{P_r}(d_o)\left(\frac{d}{d_o}\right)^n \tag{2.10}$$

where $P_r(d_o)$ is the received power at a reference distance which includes the effects of the antennas and is assumed to be a free space reference. This can be calculated using the Friis transmission formula (if the antenna gains or apertures are known) or measured. In this work a reference measurement was taken since the antenna gain calculations are somewhat problematic for UWB. Note that in typical narrowband measurements, the reference measurement must be averaged over several local measurements to eliminate multipath fading. The reference measurement was taken at d_0 = 1 m and the LOS path was extracted using time gating to eliminate multipath. *This makes the path loss calculations relative to free space at 1m*. The additional average path loss can be calculated for any subsequent measurement taken at a distance d, with received power $P_r(d)$ using

$$\overline{PL}(d) = \frac{\overline{P}_r(d_0)}{\overline{P}_r(d)}, \qquad \overline{PL}(d)_{dB} = \overline{P}_r(d_0)_{dB} - \overline{P}_r(d)_{dB} \tag{2.11}$$

Combining (2.10) and (2.11) results in

$$\overline{PL}(d)_{dB} = 10\log_{10}\left(\frac{\overline{P}_r(d_0)}{\overline{P}_r(d)}\right) = -10n\log_{10}\left(\frac{d_0}{d}\right) \tag{2.12}$$

which allows n to be determined using the path loss values, PL_{dB}, and the distances, d_0 and d. Therefore (2.12) is used to determine the path loss exponents for each of the measurement environments examined here where n is chosen to minimize the square error between the linear fit and the pathloss values [Rapp02].

Note that equation (2.12) represents the *average* path loss experienced at a distance d. The path loss observed at any given point will deviate from this average value due to variations in the environment [Rapp02]. This variation has been found to follow a log-normal distribution in many measurements. We will examine this observation for UWB channels shortly. Thus, the received signal power can be represented as

$$\overline{P_r}(d)_{dB} = \overline{P_r}(d_0)_{dB} - 10n\log_{10}\left(\frac{d}{d_o}\right) + X_\sigma \quad (2.13)$$

where X_σ is a log-normal random variable with standard deviation, σ. It should be noted that typically this variation is attributed to large objects shadowing the receiver, in our case it is more commonly due to the amount of multipath available.

2.3.2 Total vs. "Single Path" Path Loss Calculations

What we have just described is often termed the "total" path loss. Since the total received signal power is used. However, UWB signals typically result in many resovable multipath components (we will discuss this shortly). Depending on the receiver structure, the entire received signal energy may not be available to the detector. In fact, many receivers may only be able to capture the dominant multipath component. Thus we are also interested in the average power loss experienced by the dominant multipath component. We refer to this as "single path" path loss.

Thus all the received signal was used to perform the "total" path loss analysis. The received signal energy computations, for both the time and frequency domain measurements, were calculated in the frequency domain. For the frequency domain measurements, which where taken using a network analyzer over the frequency band 0.1 – 12 GHz (see [Bueh04] for a complete description of the measurements), the total received power was simply taken as the sum of the powers in the frequency band. For the time domain measurements each received signal was transformed into the frequency domain using a 2^{16}-point FFT. A portion of the frequency spectrum, which was known to have minimal signal power, was then used to calculate an average noise floor[3] (*NF*) and a standard deviation (σ_n) about that noise floor. A threshold (*Threshold*) was then set using

$$Threshold = NF + 3\sigma_n \quad (2.14)$$

such that any magnitude in the frequency spectrum greater than *Threshold* was considered to contribute to the total received power.

Note that every measurement location consists of a group of 49 measurements taken over a 1 m x 1m grid (see [Bueh04] for a complete description). These measurements comprise a local area. Path loss calculations for a measurement location is calculated as the average of the received energy for the local area. An average path loss exponent is then determined by averaging the received energy over all the locations and performing a least-squares fit on all the values of *n*.

2.3.3 Path Loss Results

This section presents path loss results that represent approximately 800 time domain and 400 frequency domain indoor measurements. The results are presented according to antenna type and environment.

[3] Note that several different methods were used to ascertain the noise floor including time gating and using noise-only measurements. It was found that there were no significant differences in the results using the different noise floor calculation methods.

The average path loss parameters for the measurements data, n and σ, are given Table 2.1. *Again, note that the path loss is relative to free space at a distance of 1m*. Compared with other UWB measurement campaigns these measurements fall within the range of typically reported values but are on the lower end. Table 2.2 summarizes results from other campaigns along with our results. Examining the "total" path loss results given in Table 2.1 a couple general observations can be made. First, the TEM and Bicone antennas have nearly the same average path loss exponent for both the LOS and NLOS environments. However the TEM horn antennas seem to exhibit a higher variation in received power. This is only slightly the case for the LOS environment but is very pronounced for the NLOS environment. The NLOS's larger variance can be attributed to the directional nature of the antenna as this will impact the number of received paths and strength of those paths as the receiver is moved throughout the environment.

It is helpful also to look at the "single path" path loss as discussed in Section 2.3.2. This provides a more complete understanding of the paths' behavior and its affect on the path loss. These results are given in Table 2.1. The LOS measurements were used to calibrate the path loss calculations since it is expected that this will always be 2. The NLOS "single path" path loss helps demonstrate that there is significant path loss for an individual path loss but the collective energy of the large number of paths results in a much lower path loss. This will be discussed in more detail shortly.

As mentioned, the results given in Table 2.1 are on the low end of previously reported results. The fact that $n < 2$ for the LOS environments while commonly reported may be somewhat counterintuitive. The following analysis gives a specific example which demonstrates the reason path loss can exhibit "better than free space" propagation in LOS scenarios. This example is for a distance of 9 meters and is given in Figure 2.13.

Figure 2.14 illustrates that in this particular case the LOS pulse of the received signal accounts for only about 25% of the total received energy of the signal. This by itself would suggest that the path loss would be better than free space but it is helpful to work out the exact path loss. The expected received power in dBm for free space propagation, P_r^{FS}, at a distance, d, is given as

$$P_r^{FS} = P_0 - 20 \log_{10}\left(\frac{d}{d_0}\right) \tag{2.15}$$

where P_0 is a reference power measurement taken at distance, d_0. Similarly the measured received power, P_r^m, at a distance, d, which in a general environment may have a path loss exponent different than free space ($n = 2$), is given as

$$P_r^m = P_0 - 10(2-\alpha)\log_{10}\left(\frac{d}{d_0}\right) \tag{2.16}$$

where α accounts for the deviation from free space. The value of α and therefore the path loss exponent, n, can be determined by calculating the difference between the received powers given by equations (2.15) and (1-17), ΔP_r, which is given as

$$\Delta P_r = P_r^m - P_r^{FS} \tag{2.17}$$

Substituting the values for ΔP_r from our example and combining equations (2.15) - (2.17) gives

$$4.8 = 10\alpha \log_{10}\left(\frac{d}{d_0}\right), \qquad \alpha = 0.5 \rightarrow n = 1.5 \tag{2.18}$$

Thus the path loss exponent for this specific example, n = 1.5, is much better than free space.

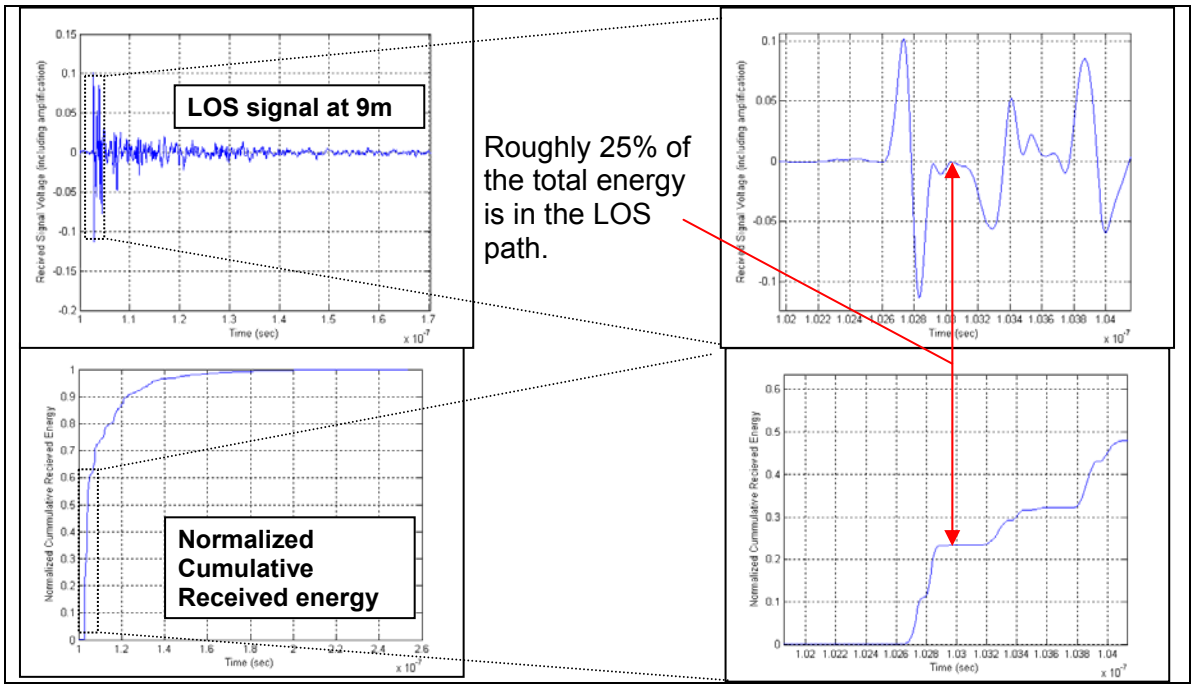

Figure 2.14 TEM LOS Received Signal and Cumulative Energy

2.3.4 Frequency Dependence of Path Loss Revisited

With the path loss model justified, we now wish to re-examine our earlier conclusion that path loss is not frequency dependent. Using frequency domain measurements, two different approaches to the analysis will be presented. First, path loss was calculated on individual frequency bins by dividing the range of frequencies into ten 1 GHz bins. The received power was calculated for each bin, and using the corresponding bin in the reference measurement, a path loss exponent and standard deviation were calculated. Comparing the results across the frequency band will provide further insight into frequency dependent path loss. It is expected that that all the bins will have similar path loss exponents, although possibly different σ values.

Secondly path loss was investigated for different bandwidths. Calculations were performed such that all bandwidths investigated had a common center frequency, f_c. Therefore f_c was chosen as 6 GHz and the bandwidth was incrementally increased around f_c in 500 MHz steps. Path loss calculations were performed for each bandwidth and it is

expected that all bandwidths will have similar path loss exponents but possibly different values of σ.

Figure 2.15 plots path loss results versus frequency for 10 different bins from 1 GHz to 10 GHz. The path loss exponents and standard deviations represent both the NLOS and LOS environments and both the Bicone and TEM horn antennas. The path loss exponents are in general fairly flat. This statement is confirmed by examining the mean path loss exponent, $\overline{n}$, and the standard deviation about this mean, $\sigma_{\overline{n}}$. For the Bicone LOS and NLOS measurements these values are $\left(\overline{n}=1.4,\sigma_{\overline{n}}=0.10\right)$ and $\left(\overline{n}=2.47,\sigma_{\overline{n}}=0.15\right)$ respectively, and for the TEM LOS and NLOS scenarios they are $\left(\overline{n}=1.36,\sigma_{\overline{n}}=0.11\right)$ and $\left(\overline{n}=2.46,\sigma_{\overline{n}}=0.14\right)$ respectively. This demonstrates that the path loss exponent variation is small. The NLOS Bicone scenario shows a slight increase in the path loss exponent with increasing frequency and it is possible that NLOS measurements may see some frequency dependence with distance.

The standard deviation of the Gaussian shadowing term, σ, shows some frequency dependence, especially for the TEM NLOS case. Since the antenna is directional and because of the possibility of having frequency selective materials the TEM NLOS case could see larger variability in the shadowing term. This should be verified with additional measurements.

Figure 2.16 plots the comparison of bandwidth and path loss. For all cases, Bicone or TEM and LOS or NLOS, the path loss exponent was found to be essentially flat. To lend support to this statement the mean path loss exponent, $\overline{n}$, and the standard deviation about this mean, $\sigma_{\overline{n}}$, were again examined. For the Bicone LOS and NLOS cases these values are $\left(\overline{n}=1.44,\sigma_{\overline{n}}=0.05\right)$ and $\left(\overline{n}=2.45,\sigma_{\overline{n}}=0.05\right)$ respectively and for the TEM LOS and NLOS scenarios they are $\left(\overline{n}=1.38,\sigma_{\overline{n}}=0.05\right)$ and $\left(\overline{n}=2.49,\sigma_{\overline{n}}=0.06\right)$ respectively. This demonstrates that the variation of the path loss exponent is rather small. The plot also shows that the standard deviation shows a decreasing trend with increasing bandwidth. This is expected since larger bandwidth signals exhibit less variation in received signal power than smaller bandwidth signals.

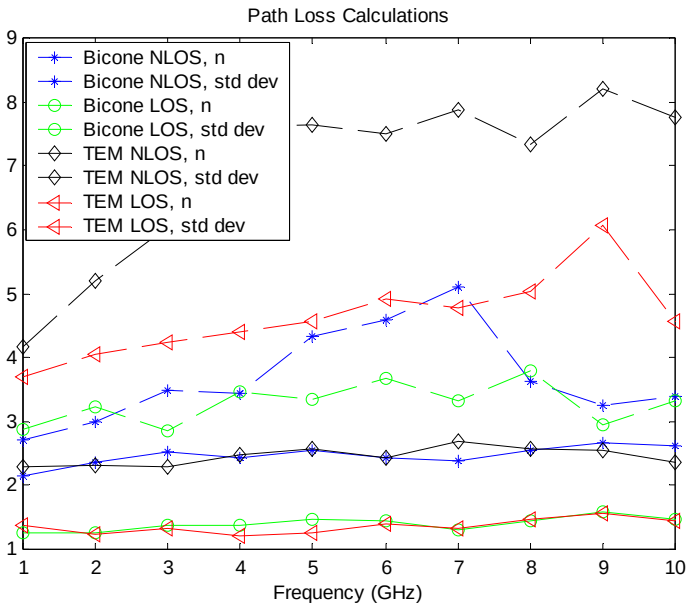

Figure 2.15 Path Loss Exponent and Standard Deviation for Different Frequencies Across the Measurement Range

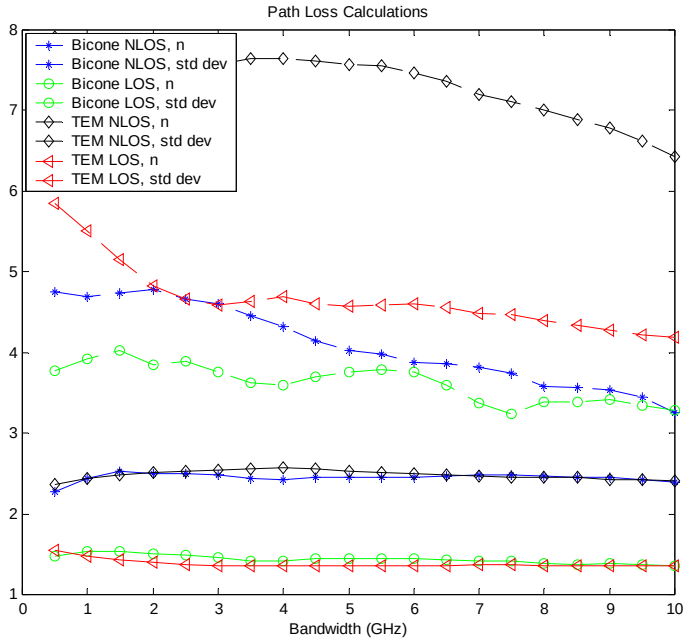

Figure 2.16 Path Loss Exponent and Standard Deviation Calculations for Different Bandwidths (in 500 MHz increments) Across the Measurement Range

2.3.5 Shadowing

Referring to equation (1-13) shadowing is represented by the term X_σ. This is modeled as a log-normal random variable with standard deviation σ and is used to characterize the deviation of received power about the average power. Note that traditionally this term is referred to as shadowing since it may be caused by objects which "shadow" the receiver. However this can also simply be caused by the number of reflectors and scatterers in the environment. Additional scattering causes more multipath and thus can result in high received signal energy. Figure 2.17 plots the CDF of the deviation of the measured received power from the calculated average. The curves in general fit a log-normal distribution fairly well, however the NLOS scenarios seem to have a little more of a deviation from this distribution, especially the TEM case. It should be noted that the TEM NLOS case had the fewest number of measurements and more measurements may be warranted to validate the log-normal fit. Note that the values for the standard deviation of each curve is given in Table 2.1.

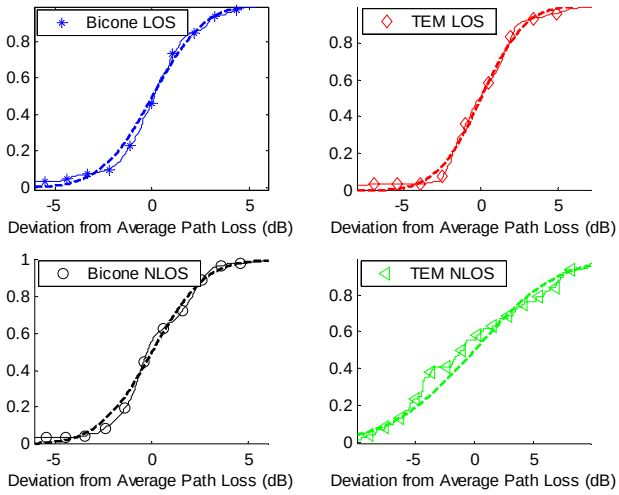

Figure 2.17 CDF of the Difference Between the Average and Measured Received Power Fit to a Log-Normal Distribution (represents shadowing)

2.4 Small Scale Channel Modeling

Like path loss, small scale statistics are important metrics required to effectively model a particular channel and facilitate receiver design. Combining all the indoor time domain data (which consists of 800 time domain profiles), time dispersion statistics were calculated for the indoor UWB channel. Specifically mean excess delay, maximum excess delay, RMS delay spread, and the number of paths were calculated. Also of interest were the number of inverted paths and the amount of inverted energy. These two statistics are of interest to the pulse-based UWB systems since pulse polarity is very important in certain modulation schemes (for instance, bi-phase modulation). The statistics were classified by the measurement environment (LOS or NLOS) and by the

particular antenna used (TEM or Bicone). To calculate these statistics an impulse response was first extracted from the channel. As described in [McKi03a], this impulse response is used to model the small scale effects of the channel and is described in the traditional narrowband sense using a tapped delay line but with a slight modification. The model is a time-invariant linear filter with the channel impulse response, *h(t)*, given by

$$h(t) = \sum_{k=0}^{N-1} a_k \delta(t - t_k) \tag{2.21}$$

where the polarity of a_k is determined by a binary random variable (the phase term in the traditional narrowband model is replaced by polarity in the UWB model). In order to extract the channel impulse response the CLEAN algorithm is used. A brief explanation of this algorithm is provided in Section 2.4.1 [McKi03a][Yano02]. Section 2.4.2 gives an explanation of the processing used to calculate the statistics and finally in Section 2.4.3 – 2.4.5 the results are presented.

2.4.1 CLEAN Algorithm

The CLEAN algorithm is a time domain deconvolution technique. CLEAN is an iterative process by which a template LOS pulse is used to extract the channel impulse response (CIR) from a received signal [McKi03a]. In computing the CIR the CLEAN algorithm cycles through the following steps. First the autocorrelation of the template LOS pulse, $r_{ss}(t)$, and the cross-correlation between the received signal and the template LOS pulse, $r_{sy}(t)$, are computed. The iterative process then begins by finding the maximum correlation peak of $r_{sy}(t)$ and the time delay, τ_k, associated with the peak, and then normalizing the peak by the correlation peak of $r_{ss}(t)$ to give the amplitude a_k. The autocorrelation, $r_{ss}(t)$, is then scaled by a_k and subtracted from $r_{sy}(t)$ at the time delay, τ_k. A second iteration is performed to find and remove the next strongest correlation peak. The iterative process continues until the maximum correlation peak has dropped below a minimum threshold. The data considered for this analysis used CIRs which were extracted using thresholds of 15 dB and 20 dB below the maximum correlation peak. A more detailed discussion of the impact of the CLEAN algorithm on the results is presented in [McKi03a].

2.4.2 Statistic Calculation Methodology

As mentioned in Section 2.3.2 each measurement location consists of a group of local area measurements taken on a grid (please see [Muqa03a] for further details). The 7x7 grid consists of points separated by 15 cm in both the horizontal and vertical directions. Because of this spacing and the short time duration of the pulses (< 200 ps) individual paths in the profile will move as the receiver is moved amongst the local area points. Therefore power delay profiles for a local area could not be averaged together to give one power delay profile upon which the statistics could be computed for a local area. Instead statistics were calculated on the individual profiles constituting a local area. The local

area average statistics were then the result of averaging the individual statistics. Averaging the local area averages gives the final average statistics.

The statistics were computed using the traditional definitions as found in [Rapp02]. Mean excess delay, $\bar{\tau}$, is given by

$$\bar{\tau} = \frac{\sum a_k^2 \tau_k}{\sum a_k^2} \tag{2.22}$$

where a_k^2 represents the power in the path at time delay τ_k. Using the same notation, RMS delay spread, σ_τ, is given by

$$\sigma_\tau = \sqrt{\overline{\tau^2} - \left(\bar{\tau}\right)^2}, \text{where} \quad \overline{\tau^2} = \frac{\sum a_k^2 \tau_k^2}{\sum a_k^2} \tag{2.23}$$

The maximum excess delay, $\tau_{\max}$, is simply equal to the max(τ_k). The number of paths is equal to the number of paths contained in a channel impulse response. The number of inverted paths is simply the number of paths which have negative polarity and the amount of inverted energy is the percentage of the power contained in the inverted paths.

2.4.3 Small Scale Average Results

Table 2.1 presents average small scale statistics that were calculated using channel impulse responses computed with 15 dB and 20 dB thresholds. In every case the 20 dB threshold always gives greater values than the 15 dB threshold case (excluding the inverted energy statistics, these remain fairly constant). This is expected since the CLEAN algorithm will find more paths in the 20 dB case. Note the threshold used for the CLEAN should be chosen in relation to the SNR of the measurements. A more detailed discussion of the impact of CLEAN threshold is given in [McKi03a].

Comparing the results for the different environments and the different antennas reveals some relative trends for the mean excess delay, the max excess delay, the RMS delay spread, and the number of paths. In general the TEM horn antennas, which are directional, always give lower values than the Bicone antennas, which are omni directional. This is expected since an omni directional antenna illuminates more scatterers and is able to collect more multipath than a directional antenna. Also the LOS cases always produce lower values than the NLOS which is due to the presence of the dominant LOS path.

In terms of inverted paths all cases seem to invert about 50% of the paths except the LOS TEM case. This is intuitive since, due to their directivity, the TEM Horn antennas will tend to receive mainly signals from the LOS direction which will be inverted with smaller probability.

Table 2.3 gives a comparison of previously reported results for the number of paths, mean excess delay, and RMS delay spread. The results in Table 2.1 are within the range of these results and match nicely with some results and not as well with others. However it should be noted that Table 2.3 represents a wide range of environments.

2.4.4 Small Scale Statistic Distributions

Table 2.1 represents averaged results and it is therefore instructive to examine the CDFs of these statistics in order to better understand the overall characteristics of the channel. CDF calculations were performed for the RMS delay spread, mean excess delay and the number of paths. These are given in Figure 2.18, Figure 2.19 and Figure 2.20 respectively. The results represent all 800 time domain measurements. In general we see more variation occurs in the Bicone measurements than the TEM and also more variation is apparent in the NLOS than in the LOS. The TEM horn antenna seems to show vary little variance for either the LOS or NLOS case which can be attributed to the directional nature of the antenna. Note that as expected, NLOS channels provide a larger mean in the delay statistics as well as a larger variance than LOS channels. Additionally, Bicone antennas also result in both larger means and variations. An attempt was made to fit each curve to a normal CDF, which is the superimposed dotted line. The Gaussian distribution provides a reasonable.

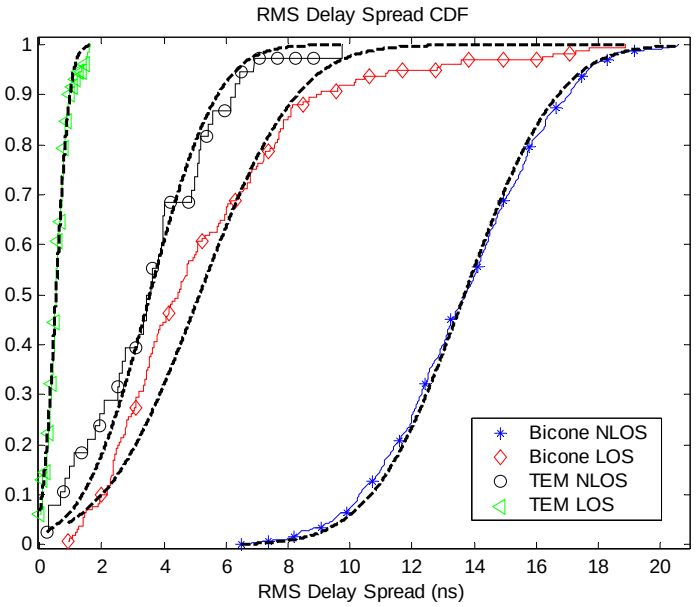

Figure 2.18 CDF of RMS Delay Spread for Various Scenarios (Along with Best Gaussian Fit)

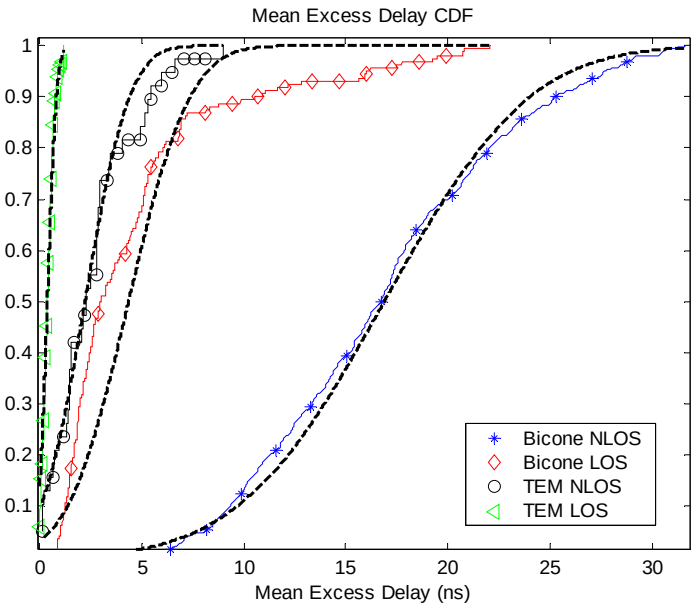

Figure 2.19 CDF of Mean Excess Delay for Various Scenarios (Along with Best Gaussian Fit)

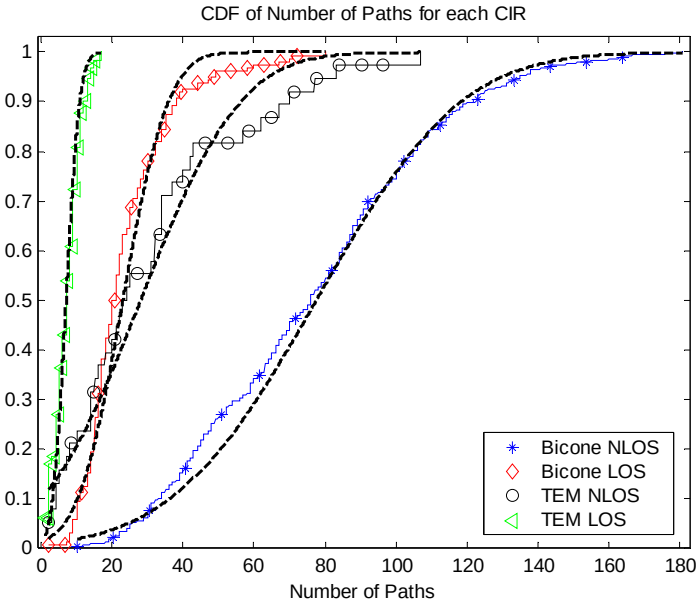

Figure 2.20 CDF of the Number of Paths for Various Scenarios (Along with Best Gaussian Fit)

2.4.5 Channel Energy Capture[4]

In addition to the previous results, Figure 2.21 represents the total amount of energy that a 50-finger Rake receiver could capture performing non-coherent energy capture using a number of pulse-matched filters. The plot illustrates general trends related to the directivity of the antennas being used, with much of the total energy being captured with few fingers in the TEM cases and requiring many more fingers in the omni-directional, Bicone, cases. (As a note the energy capture never reaches 100% due to the inter-pulse interference. This is the result of the closely spaced paths and this is particularly evident in the TEM LOS case).

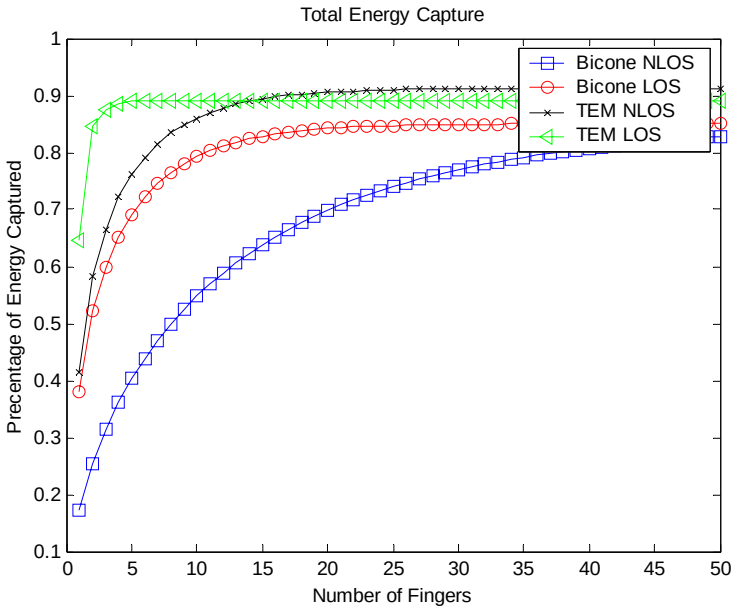

Figure 2.21 Total Energy Capture with Increasing Number of Rake Fingers

2.6 Conclusions

This chapter has presented large and small scale results of the indoor UWB channel, and contributes additional data to the already existing group of reported measurement results. Furthermore, an analysis of frequency domain data has been provided which reinforces the theorectical anlaysis demonstrating that the frequency dependence of the received power is an antenna effect and that path loss is not frequency dependent for the distances investigated. Link budget considerations were also discussed. Further, the CDFs of the reported small scale statistics were examined. This analysis provided some insight to the effects of the different antennas in certain environments on the observed small scale statistics. Finally an analysis of energy capture vs. Rake fingers also provided some

[4] Note that all the energy capture results were obtained by convolving a 500 ps Gaussian pulse with the CIRs extracted from the measurement data and then correlating with that same pulse to find the energy in the fingers.

insight into the effects of the antenna and environment on the distribution and relative strengths of the received paths.

Table 2.1 Large Scale Path Loss Parameters and Small Scale Statistics with 15 and 20 dB Thresholds

	Bicone							
	Total		Peak		Total		Peak	
	n	σ (dB)	n	σ (dB)	n	σ (dB)	n	σ (dB)
LOS	1.3	2.6	2	0.71	1.3	2.8	2	-
NLOS	2.3	2.4	2.7-4.3	2.97-3.98	2.4	5.1	3.35	6.3

	Bicone				TEM			
	15		20		15		20	
	NLOS	LOS	NLOS	LOS	NLOS	LOS	NLOS	LOS
Mean Excess Delay (s)	1.60E-08	5.19E-09	2.01E-08	1.05E-08	2.36E-09	5.52E-10	5.59E-09	1.22E-09
Max Excess Delay (s)	6.57E-08	2.84E-08	7.86E-08	5.68E-08	1.61E-08	2.65E-09	4.31E-08	1.24E-08
RMS Delay Spread (s)	1.37E-08	5.41E-09	1.62E-08	8.50E-09	3.27E-09	7.53E-10	7.09E-09	1.70E-09
Number of Paths	72.8415	24.2753	153.9571	64.5884	28.7333	6.4188	99.1556	15.7607
Inverted Paths	49.00%	47.61%	49.30%	48.68%	50.71%	39.54%	49.81%	43.93%
Inverted Energy	44.23%	45.02%	45.36%	45.63%	34.26%	24.19%	37.67%	25.97%

Table 2.2 Measured Path Loss Exponents (*n*) and Shadowing Standard Deviation (σ) in Published Measurement Studies (mean and standard deviation of both quantities are shown for some studies)

Researchers	*n* : Mean	*n* : Std. Dev.	σ (dB) : Mean	σ (dB) : Std. Dev.	Distance (m)
Virginia Tech (office)	1.3-1.4 (LOS) 2.3-2.4 (NLOS)		2.5-3 (LOS) 2.6-5.6 (NLOS)		5-49 (LOS) 2-9 (NLOS)
AT&T (Res.) [Ghas03]	1.7 /3.5 (LOS/NLOS)	0.3 /0.97	1.6/2.7	0.5/0.98	1-15 (LOS) 1-15 (NLOS)
U.C.A.N. [Alva03]	1.4/3.2(soft)/4.1(hard) LOS/NLOS/NLOS		0.35 LOS/1.21(soft) /1.87(hard) NLOS		4-14 (LOS/NLOS)
France Telecom [Paga03]	1.5 / 2.5 (LOS/NLOS)				2.5-14 (LOS) 4-16 (NLOS)
CEA-LETI [Keig03]	1.6 (lab)1.7(flat) LOS 3.7 (office/lab/NLOS) 5.1 (flat/NLOS)		4 / 4 (LOS/NLOS)		1-6, 1-8 (LOS 2-20,7-17 (NLOS)
Intel (Resident.) [Rusc04]	1.7/4.1 (LOS/NLOS)		1.5/3.6 (LOS/NLOS)		1-11 (LOS) 4-15 (NLOS)
IKT, ETH Zurich [Zaso03]	2.7- 3.3 (on body) 4.1 (around the torso)				0.15 – 1.05
Cassioli/ Molisch/Win [Cass02]	2.04 (d<11m) -56+74log(d) (d>11)		4.3		8-11 (NLOS) 11-13(NLOS)
Oulu Univ. [Hovi02]	1.04,1.4,1.8 LOS 3.2, 3.3, 3.9 NLOS				1-30 (LOS) 4-14 (NLOS)
Whyless [Kuni02]	1.58/1.96 LOS/NLOS				2.5-16 (LOS/NLOS)
Time Domain [Yano02]	2.1 (LOS/NLOS)		3.6		2-21 (LOS/NLOS)

Table 2.3 Comparison of Previously Reported UWB Small Scale Results

Researchers	$\overline{\tau}$ (ns)	σ_τ (ns)	num paths
LOS			
Virginia Tech(Office)	5.19	5.41	24
TDC [Yano02] [Pend02]	4.95 (0-4m)	5.27 (0-4m)	24
CEA-LETI [Keig02a]	4-9	14-18	
CEA-LETI [Keig02b]	6.53 (home)	11.45 (home)	3.4 (home)
	6.42 (office)	10.07 (office)	2 (office)
AT&T [Ghas02b]		1.6	
AT&T [Ghas02a]		1.1-16.6, mean 4.7	
Intel [Pret02] [Foer02b]	4	9	7
802.15 model [Foer02a]	5.1	5.3	24
NLOS			
Virginia Tech(Office)	16	13.7	72
USC [Cram99] [Cram02a] [Cram02b]	~59-126	~45-74	
TDC [Pend02] [Yano02]	10.04 (0-4m)	8.78 (0-4m)	36.1 (0-4m)
	14.24 (4-10m)	14.59 (4-10m)	61.6 (4-10m)
CEA-LETI [Keig02a]	17-23	14-18	
CEA [Keig02b]	16.01 (4-10m)	14.78 (4-10m)	46.8 (4-10m)
	18.85 (10-20m)	17.64 (10-20m)	75.8 (10-20m)
AT&T [Ghas02b]		2.7	
AT&T [Ghas02a]		0.75-21, mean 8.5	
Intel [Pret02] [Foer02b]	17	15	35
802.15 model [Foer02a]	10.4/14.2	8/14.3	36/62
Hashemi (survey paper of various non-UWB indoor results) [Hash93]		20-50, 25 (small/med office) <120,200 (large office) 70-90,<80 (office) <100 (university) 8.3 (LOS), 8.3, 14.1 (NLOS) (office)	

Chapter 3
Narrowband Interference Mitigation

3.1 Introduction

UWB offers many potential advantages for wireless communications and ranging, however a major drawback is that it is highly susceptible to narrowband interference. Consequently the error performance suffers and the systems range is limited. Even though the bandwidth of a UWB signal is extremely large, especially compared to a potential narrowband interferer, the narrowband interferer has a much higher power spectral density. This can be extremely detrimental to a UWB receiver. The following discussion provides some analysis into the nature of the narrowband interferer's impact on a UWB receiver.

Consider a narrowband tone interferer modeled as

$$i(t) = A\sin\left(2\pi f_c t + \phi\right) \tag{3.1}$$

where f_c is the center frequency of the signal and ϕ is a random phase offset. Note that over the duration of a UWB pulse a narrowband interferer, even if it is digitally modulated, will appear as a tone. Therefore, when examining a single pulse, any type of narrowband interference can be characterized by simply using equation (3.1). The interferer's impact can be characterized according to its center frequency, the UWB pulse width (i.e. bandwidth), and the type of UWB pulse, baseband or bandpass. Likewise the phase of the interferer, relative to the phase of the pulse, can also cause varied performance.

First the impact of the interferer's center frequency is discussed. Consider a Gaussian modulated RF pulse (as described in Chapter 1) given by

$$p(t) = g(t)\sin\left(2\pi f_{c,UWB} t\right) \tag{3.2}$$

where $g(t)$ is the Gaussian pulse given in equation (1.1) and $f_{c,UWB}$ is the center frequency of the resulting pulse, $p(t)$. As might be intuitive, an interferer with the same center frequency as that of the pulse is possibly the most detrimental to the system's performance. This interferer's impact is most easily quantified by determining the correlation loss between an uncorrupted pulse and a pulse in the presence of a narrowband interferer. Therefore, correlation loss is expressed as a fraction, taking the correlation of $p(t)$ with $p(t) + i(t)$ divided by the autocorrelation of $p(t)$. The plot

therefore shows the energy reduction associated with narrowband interference. Figure 3.1 plots the relationship between correlation loss and frequency for several different pulse widths (i.e. bandwidths), specifically t_p = 800 ps, 1200 ps, 1600 ps, and 2000 ps with $f_{c,UWB} = 10\ GHz$. (Note that the correlation loss reported is a worse case analysis and is calculated for the relative phase of each interferer which is the most detrimental. The impact of phase will be discussed shortly.). It can be seen that the correlation loss peaks at the center frequency of the pulse and then falls off as the frequency increases or decreases, moving away from f_c. The impact also varies as a function of pulse width. As expected this variation is directly correlated with the spectrum of the pulse.

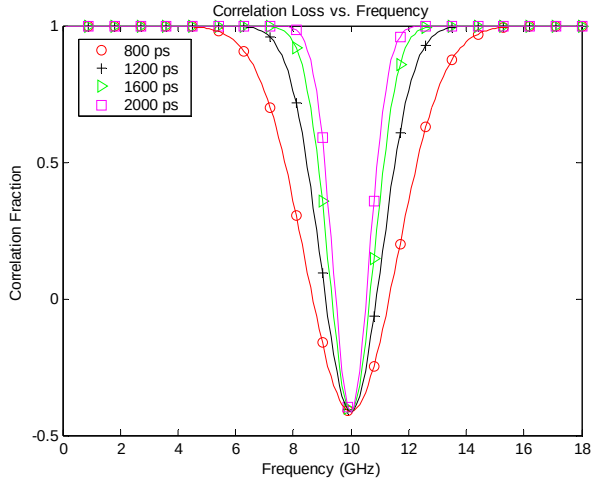

Figure 3.1 Correlation Loss for RF Pulses

As previously mentioned the relative phase alignment of the UWB signal and the narrowband interferer also has an impact on the performance degradation. Since the UWB signal was created using a sine wave with a phase of zero, the results are presented by simply varying the phase of the interferer from 0 to 2π. The impact of the relative phases was investigated for the same frequencies and pulse widths used in the discussion concerning correlation loss. It was determined that for the range of frequencies investigated that as the phase of the interferer was varied from 0 to 2π the impact of the interferer also varied. This impact is measured in terms of its constructive and destructive interference. The interference was found to be cyclic and varies in a sinusoidal fashion as a function 2π. The impact of the relative phase also varies from frequency to frequency but the periodic nature remains the same. In general for a UWB pulse and NBI signal with equal center frequencies the most degradation is caused by an interferer that is 180 degrees out of phase and the degradation is the least when the interferer is completely in phase. However as frequency changes so does the phase causing the most degradation.

Using "spreading" with the UWB receiver also impacts performance in the presence of narrowband interference. "Spreading" is the transmission of multiple pulses per data symbol. This introduces time diversity in the received signal, and averaging over the repeated pulses improves BER performance at the expense of decreasing the data rate. In

the presence of narrowband interference the averaging will help improve the BER performance of the system.

3.2 Narrowband Interference Cancellation: Theory and Previous Work

As mentioned, existing narrowband technologies pose a serious threat to the proper operation of a pulse-based ultra-wideband (UWB) communications system. Compared to UWB, a narrowband signal's power spectral density (PSD) level is much greater. Consequently the system suffers unless the interference can be mitigated. This chapter provides some background information on narrowband interference cancellation. Very little literature exists on narrowband interference cancellation as it relates to UWB. The provided introduction will therefore mainly focus on direct sequence spread spectrum (DS-SS). This area has and continues to receive a great deal of attention and because the interference problem is very similar (in terms of a wideband signal in narrowband interference) and most of the solutions for DS-SS could be applicable to UWB.

The majority of the techniques used for suppressing narrowband interference involve filtering. The goal of any of these filters is to cancel or suppress the interference while not distorting the desired signal, consequently improving the system's performance in terms of SNR and BER performance. These filters constitute two general categories; estimation or prediction filters and transform domain filters. Examples of each of these filters will be discussed in detail in the following sections.

3.2.1 Linear Prediction Filters

A linear prediction filter can be described as a whitening operation that makes the output samples of the filter uncorrelated. The goal is to eliminate the narrowband interference while incurring an acceptable level of distortion in the desired signal. Linear prediction filters operate on the assumption that future values of a wideband signal tend to be uncorrelated with current values while the narrowband interference exhibits correlation between its past and future values. This temporal correlation can be exploited to predict the narrowband interferer and cancel it from the received signal [Last97][Proa96].

A block diagram of the receiver structure incorporating a linear prediction filter is given in Figure 3.2. Using this system the received signal can be modeled as

$$r(t) = s(t) + i(t) + n(t) \tag{3.3}$$

where *r(t)* is the received signal, *s(t)* is the desired signal, *i(t)* is the narrowband interference and *n(t)* is the additive white Gaussian noise (AWGN). From this point forward the system model is examined using discrete values, where *j* denotes discrete time, and the received signal samples will be represented by

$$r_j = s_j + i_j + n_j \tag{3.4}$$

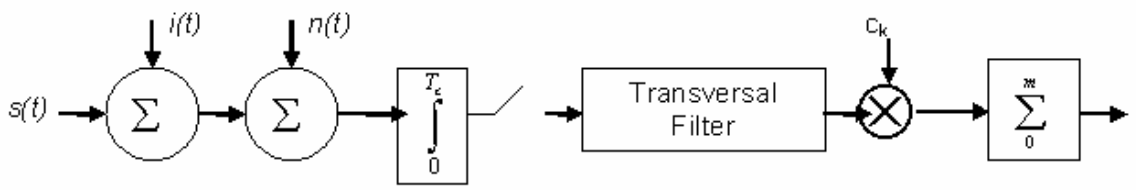

Figure 3.2 System Model for DS-SS with a Prediction Filter

In general the linear prediction filter pictured in Figure 3.2 can be a one-sided prediction error filter, as shown in Figure 3.3, or a two-sided transversal filter, as show in Figure 3.4. The discussion from this point forward mainly focuses on the latter since its symmetry offers a simpler implementation and has also been shown to exhibit nearly equal or better performance than the prediction error filter [Li82]. However the analysis is valid for both filters.

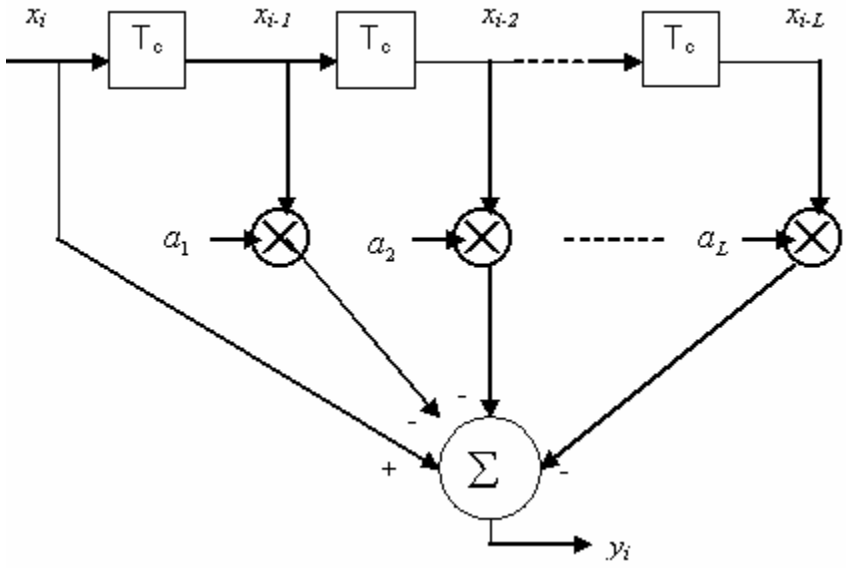

Figure 3.3 Prediction Error Filter

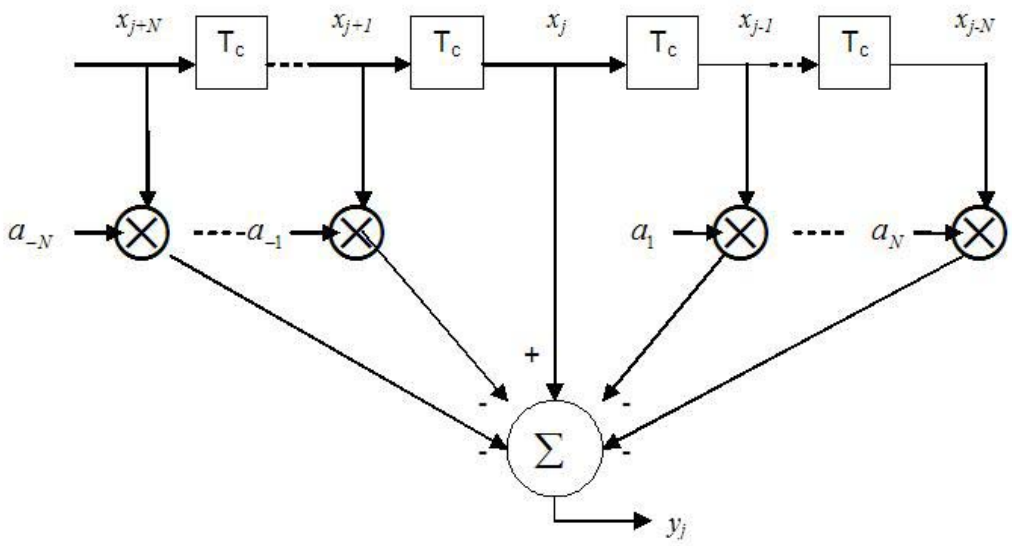

Figure 3.4 Transversal Filter with Two-sided Taps

The filter depicted in Figure 3.4 attempts to produce an estimate of the interference, $\hat{i}_j$, and then subtracts the estimate from the received signal, x_j, cancelling the interference. The sample x_j is the central tap of the filter and $\hat{i}_j$ is given by

$$\hat{i}_j = \sum_{k=-N,k\neq 0}^{N} a_k x_{j-k} \tag{3.5}$$

Thus the output of the filter y_j is given by $y_j = x_j - \hat{i}_j$ and the optimum weights of the filter taps, $a_{-N},\ldots,a_{-1},a_1,\ldots,a_N$, can be determined by minimizing $E\left[y_j^2\right]$, i.e. minimizing the mean square error of the filter. According to the orthogonality principle, in order to minimize mean square error, the error, in this case y_j, must be orthogonal to the data, x_{j-m} where $m \geq 1$. This minimization is given by

$$E\left\{\left(x_j - \sum_{k=-N,k\neq 0}^{N} a_k x_{j-k}\right) x_{j-m}\right\} = 0, \qquad m \geq 1 \tag{3.6}$$

which yields

$$R_{jj}[m] = \sum_{k=-N,k\neq 0}^{N} a_k R_{jj}[m-k] \tag{3.7}$$

where $R_{jj}[m] = E\{r_j r_{j-m}\}$ is the autocorrelation of the received signal [Papo02]. This is the well known Weiner-Hopf equation and can be solved to find the optimum tap weights of the filter. However this requires knowledge of the received signal's autocorrelation

function, which in practice will not be known and is also likely time varying [Proa96]. This motivates the need for adaptive algorithms which can be used to update the tap weights of the filter. Common adaptive algorithms include the LMS and RLS estimation techniques. The LMS algorithm can be represented by three basic relationships [Last97]:

1. The filter output: $y_j = w_j^H x_j$ (3.8a)
2. The adaptation error: $\varepsilon_j = d_j - y_j$ (3.8b)
3. The tap weight adaptation: $w_{k+1} = w_k + \mu x_k \varepsilon_k^*$ (3.8c)

where j denotes discrete time, y_j is the filter output, w_j is the tap-weight vector, x_j is the tap-input vector, H indicates the Hermitian (i.e. conjugate transposition), ε_j is the estimation error, d is the desired response, μ is the step-size parameter and * denotes the conjugation. Several adaptive algorithms and receiver structures which can be employed are now discussed.

In [Ketc82] Ketchum and Proakis examine and compare the performance of several adaptive algorithms (Note their analysis was performed for a one-sided prediction error filter). In general they divide the algorithms into two categories: nonparametric and parametric (linear prediction). The first category, nonparametric, employs the Fast Fourier Transform (FFT) to perform spectral analysis upon which an estimate of the transversal filter can be designed. It was found that this method presented a viable means for narrowband interference suppression. However this implementation requires a relatively large number of samples to obtain a good estimate and requires a larger order filter to obtain the same notch filter when compared with the linear prediction algorithms. Therefore the performance of the second category, parametric algorithms, will be discussed in more detail as it provides a simpler solution and is the more prevalent method.

Ketchum and Proakis divide the parametric category into three algorithms, the Levinson Algorithm, the Burg Algorithm, and the Least Squares Algorithm. The linear prediction methods are based on modeling the narrowband interference as white noise passed through an all-pole filter. The suppression filter is then determined by using the estimated poles as the coefficients for the all-zero transversal filter, rendering the output white. The following introduces the three different algorithms.

Referring to equation (3.7), the Weiner-Hopf equation can be represented in matrix form by

$$R_m a_m = b_m \tag{3.9}$$

where R_m is the $m \times m$ autocorrelation matrix, a_m is the vector of filter coefficients, and b_m is the vector of autocorrelation coefficients $R_{jj}[m]$. When the matrix R_m is a Toeplitz matrix it can be efficiently inverted using the Levinson-Durbin algorithm. This algorithm is order recursive and can be used to determine the coefficients [Ketc82]. In order to make this algorithm adaptive there must be a way to determine the

autocorrelation of the received signal. This is typically done by directly estimating $R_{jj}[m]$ using the received data and is given by

$$\hat{R}_{jj}[m] = \sum_{n=0}^{N-m} r[n]r[n+m] \tag{3.10}$$

The second algorithm, the Burg algorithm, operates using the same principle as the Levinson algorithm and can be considered an order recursive least squares algorithm. The algorithm uses the Levinson recursion in each iteration and forces the filter coefficients to satisfy the Levinson-Durbin recursion (for a detailed analysis please see [Ketc82]). The third and final algorithm is the Least Squares algorithm, which is different from the Burg algorithm in that the coefficients are not constrained to satisfy the Levinson-Durbin recursion. Also the coefficients are obtained in the least squares sense by minimizing over the entire set of filter coefficients. The solution to this is comparable to the set of equations (3.8a) – (3.8c).

Ketchum and Proakis' analysis compared the performance of the different adaptive algorithms and examined multiband interference as well. For the sample size investigated they found that all the algorithms performed equally. However it was noted that for small sample sizes the Burg and least squares algorithm would outperform the Levinson algorithm simply because the estimate of the autocorrelation for the Levinson algorithm will be poor. In their simulations they also considered a type of matched filter receiver variation of the prediction filter. If the signal is represented by $S(f)$ and the noise-whitening filter by $H(f)$, then the matched filter will have the frequency response $H^*(f)S^*(f)$ and will maximize the output SNR. It was found that the matched filter implementation leads to significant improvements in performance when compared with using only the linear suppression filter. It is also of interest to examine the suppression filter's performance in the presence of several narrowband interferers. For the multiband interference it was found that the filter will suppress the interference provided there are enough degrees of freedom to assign at least one complex-conjugate pair of zeros in each band. In other words the number of coefficients should be twice the number of interference bands.

In a complimentary analysis in [Ilti84][Mils88], Iltis and Milstein investigated three different interpretations of the suppression filter for performing linear least squares estimation and compared their performance in the presence of a single tone jammer and a narrowband Gaussian jammer. The first implementation uses a suppression filter to subtract the narrowband interference from the received signal (Criterion 1). The second implementation uses the structure suggested in [Ketc82], which implements a suppression filter followed by a matched filter and the whitening filter (Criterion 2). Lastly the third structure employed an all-zero filter which generates an infinitely deep notch in the frequency response at the location of the interferer (Criterion 3).

Iltis [Ilti84] reported that when employing Criterion 1 the performance improves as the strength of the jammer increases and also that using the suppression filter alone is less

effective against Gaussian jammers than tone jammers. For Criterion 2 they found that the performance degraded with an increase in the Gaussian interferer's power but that some improvement can be seen if the number of filter taps is increased. They attribute the worsening performance to the finite number of filter taps, meaning only a finite number of zeros can be placed in the interference band. Increasing the number of taps therefore improves performance however some jammer energy will always pass through the suppression filter. It is also shown that the matched filter performance was superior to that of just the prediction filter. However the two-sided transversal filter was found to perform equally as well as the matched filter prediction filter in the presence of either a tone or Gaussian noise jamming. It is interesting to note that the two sided matched filter actually showed a degradation in performance.

The LMS algorithm discussed previously is known to have a slow convergence rate and therefore structures other than the transversal filter have been investigated. One such structure is the lattice filter [Mils88] and is given in Figure 3.5. It has been shown that each section of the filter converges individually and independently from the other sections and therefore an adaptive version of this filter can result in a much faster convergence than the LMS algorithm [Mils88].

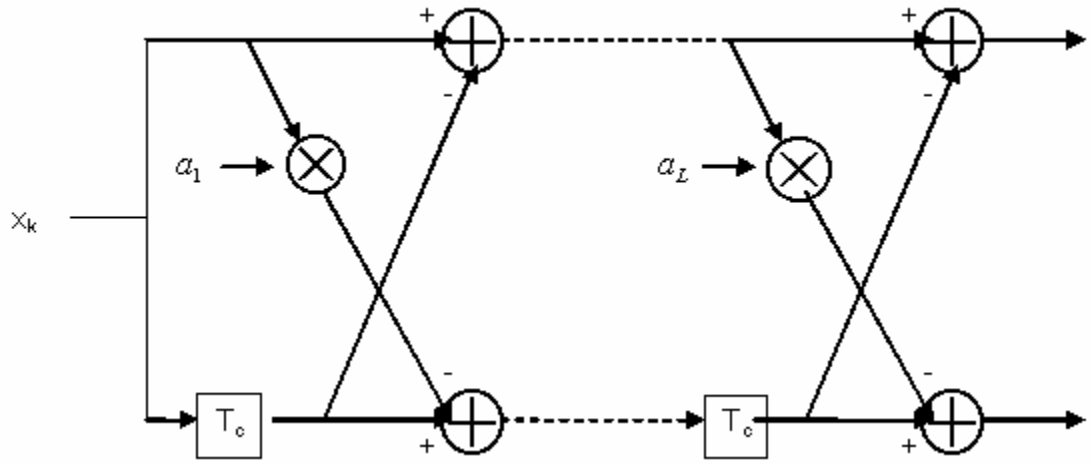

Figure 3.5 Lattice Filter

3.2.2 Nonlinear Prediction Filters

The linear prediction filters discussed in the previous section are designed on the assumption that the signal, s_j, and the noise, n_j, are Gaussian random processes. However a DS-SS signal appears to be non-Gaussian noise to the filter and therefore linear prediction methods are suboptimal. The optimum estimator is consequently based on nonlinear filtering techniques [Last97][Proa96].

The narrowband signal is still modeled as an autoregressive (AR) process in which the output is the result of passing AWGN through an all-pole filter. In [Vija90] it is shown that the optimum estimates for the nonlinear filter can be found using a series of Kalman-

Bucy filters. However this implementation is extremely complex and not suitable for implementation. Therefore Vijayan and Poor use an approximate conditional mean (ACM) filter to estimate the filter coefficients. [Vija90] also concluded that the ACM filter outperformed the Kalman filter as the order of the autoregression was increased. As shown in the linear filters the determination of the coefficients once again requires prior knowledge of the interference which is not known and therefore requires an adaptive algorithm to be implemented.

Note that the received signal is the sum of an autoregressive process and a white process. This yields an autoregressive moving average (ARMA) process with the same autoregressive parameters as the interference. Therefore the estimation is concerned with estimating the autoregressive parameters of an ARMA process. It was found that directly adapting the ACM filter using estimates of the AR parameters was not plausible because the ACM filter is sensitive to variations in the parameters (a derivation of the ACM filter is given in [Vija90]). Vijayan and Poor examine two adaptive algorithms to determine the coefficients, an LMS algorithm and a nonlinear gradient algorithm.

The Widrow LMS algorithm, which is widely used to adapt the coefficients of linear transversal filters (and is given by equations (3.8a) – (3.8b)), was used along with a nonlinear transformation to determine the nonlinear filter coefficients. The predicted value of the current state is given as a linear function of the previous estimate modified by a nonlinear function of the prediction error. A diagram of the adaptive nonlinear prediction filter is given in Figure 3.6. For illustrative purposes the equation for the linear prediction filter is given by [Vija90]

$$\hat{z}_k = \sum_{i=1}^{L} a_i(k-1)\left[\hat{z}_{k-i} + \varepsilon_{k-i}\right] \tag{3.11}$$

For the nonlinear filter an assumption is made that the error, ε_k, is the sum of a Gaussian random variable and a binary random variable (this same assumption was used in the derivation of the ACM filter). Assuming the variance of the Gaussian random variable is σ_k^2 then the nonlinear transform shown in Figure 3.6 is given by

$$\rho_k(\varepsilon_k) = \varepsilon_k - \tanh\left(\frac{\varepsilon_k}{\sigma_k^2}\right) \tag{3.12}$$

The representation of the prediction of z_k for the nonlinear transversal filter is then given by

$$\hat{z}_k = \sum_{i=1}^{L} a_i(k-1)\left[\hat{z}_{k-i} + \rho_{k-i}(\varepsilon_{k-i})\right] \tag{3.13}$$

It is then possible to update the weights using the Widrow LMS algorithm as given in equations (3.8a)-(3.8c). However first an estimate of σ_k^2 is need. This variance is approximated by $\hat{\sigma}_k^2 = \Delta_k - 1$ where Δ_k is a sample estimate of the prediction error variance. In contrast to the linear prediction filter, the updating of the nonlinear filter depends explicitly on the previous predicted values as well as the previous filter inputs.

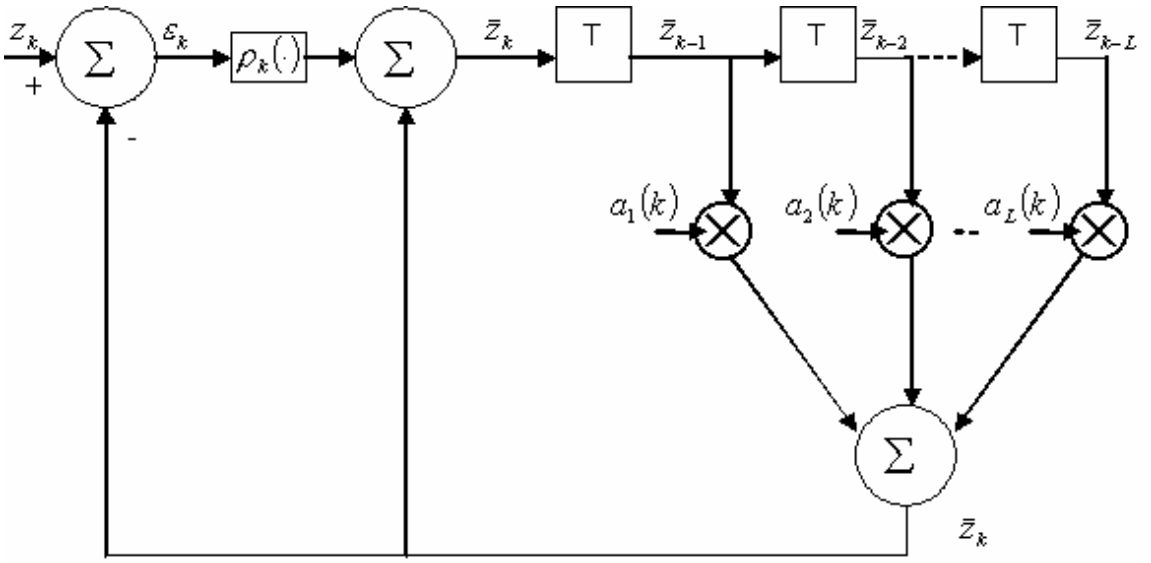

Figure 3.6 Adaptive Nonlinear Prediction Filter

The above mentioned LMS algorithm is a gradient algorithm based on linear prediction and therefore Vijayan and Poor investigated a nonlinear gradient algorithm. However their results determined that the nonlinear gradient algorithm offered no appreciable advantages over the LMS algorithm while at the same time requiring many more computations. Also the results were compared with a linear two-sided interpolation filter. The nonlinear LMS filter was found to perform significantly better than the linear filter in both sinusoidal and autoregressive interference. However Vijayan and Poor noticed that occasionally the non-linear filter would not offer much improvement over the linear filter. Vijayan and Poor conjecture that the error surface of the non-linear filter has a high possibility of having local minima and therefore the algorithm is not always guaranteed to converge to the global minimum. On the other hand the linear filter uses a gradient algorithm and is guaranteed to converge to a local minimum.

Another possible non-linear filter configuration is the decision feedback filter [Last97] [Mils88]. A block diagram of this filter is given in Figure 3.7. The basic concept of a decision feedback filter is that performance may be improved if the interference can be whitened without the desired signal being present. Ideally the desired signal would be subtracted from the received signal leaving only interference and noise. The interference could then be whitened without distorting the desired signal. Obviously the desired signal is not known and must be estimated. The estimate is taken from the receiver's estimate of the data symbol. Since the replicated signal is generated from the estimated data symbol it is possible that this estimate may be incorrect. This can lead to error propagation and poor performance. [Mils88] gives results which show that the ideal decision feedback filter outperforms a linear suppression filter of the same size. It was also reported that error propagation had a minimal impact on the performance of the decision feedback filter. However it seems that in low SIR situations the decisions would be very poor and cancellation would not be very effective.

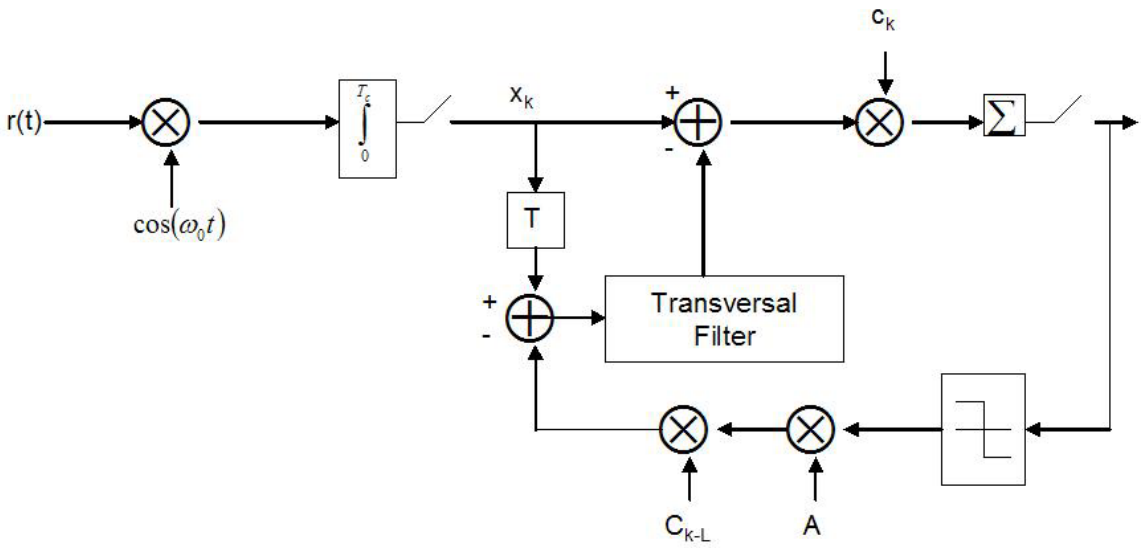

Figure 3.7 Decision Feedback Receiver

3.2.3 Transform Domain Processing

Transform domain processing is another filtering technique for suppressing narrowband interference. A receiver employing this technique would utilize a device that allows the computation of a real-time Fourier transform. Figure 3.8 below gives a general block diagram of a transform domain receiver. The switch or gain function in the block diagram allows the interference to be suppressed either through soft limiting or by notching. In UWB it would not be currently practical to digitally sample the signal and copmute an FFT. This is due to the extremely large bandwidths of the signal. The following discussion is therefore directed toward the use of a SAW filter to perform this operation.

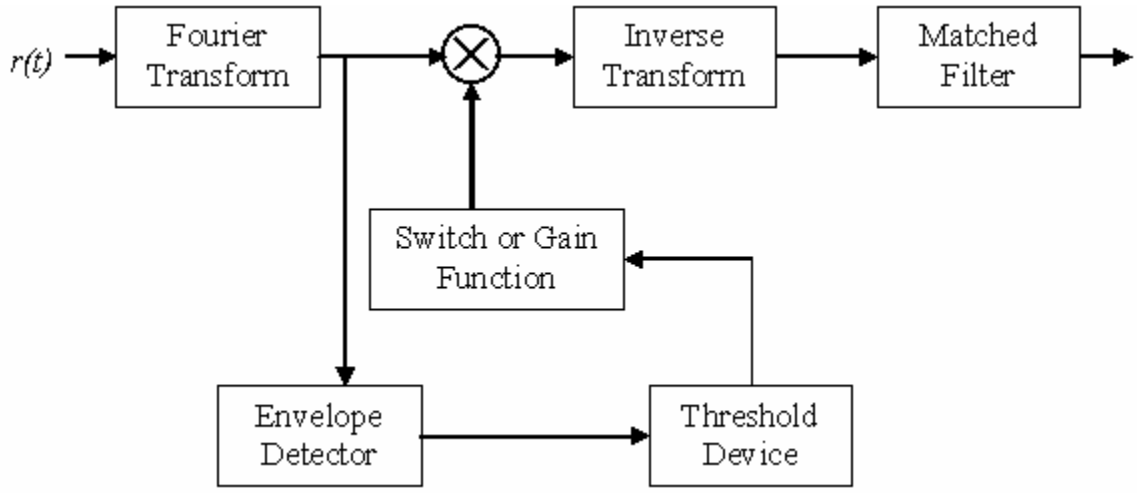

Figure 3.8 Transform Domain Processing Receiver Block Diagram

The Fourier transform and inverse Fourier transform blocks can be realized using SAW filters. This is accomplished by using the SAW filter to perform the convolution of two FM chirp waveforms. It is described in [Mils77] that the convolution of two signals can be performed using the nonlinear interaction of two properly modulated oppositely traveling waves. By applying the two RF signals $f(t)e^{j\omega t}$ and $g(t)e^{j\omega t}$ as inputs to opposite ends of a SAW device the convolution of $f(t)$ and $g(t)$ can be obtained. The following analysis explains the convolution operation [Mils77].

While in the SAW device's medium these two signals $f(t)e^{j\omega t}$ and $g(t)e^{j\omega t}$ can be represented at any point *x* and for any time *t* by

$$f\left(t-\frac{x}{v}\right)e^{j(\omega t-kx)} \text{ and } g\left(t+\frac{x}{v}\right)e^{j(\omega t+kx)} \tag{3.14}$$

where *v* is the velocity of the wave and *k* is a propagation constant. The following three signals are produced when the two waves overlap within the device (assuming a second order nonlinearity):

$$\frac{K}{2}\left[f\left(t-\frac{x}{v}\right)\right]^2 e^{2j(\omega t-kx)} \tag{3.15}$$

$$\frac{K}{2}\left[g\left(t+\frac{x}{v}\right)\right]^2 e^{2j(\omega t+kx)} \tag{3.16}$$

$$Kf\left(t-\frac{x}{v}\right)g\left(t+\frac{x}{v}\right)e^{2j\omega t} \tag{3.17}$$

where *K* is a constant representing the strength of the nonlinearity of the SAW device. The first two terms represent second order harmonics, but the last term is the term of interest and represents the product of two envelope functions. In order to complete the convolution these terms need to be integrated. The SAW device automatically performs this integration with the integration length being *L*. *L* is the length of the SAW device. For large values of *L* ($L > 10\lambda$) the term in (3.17) is the only important term and the output of the SAW device is given by

$$y(t)=K\int_{-L/2}^{L/2} f\left(t-\frac{x}{v}\right)g\left(t+\frac{x}{v}\right)dx = Kv\int_{t-L/2v}^{t+L/2v} f(\tau)\,g(2t-\tau)\,d\tau \tag{3.18}$$

Thus, this gives the convolution of $f(t)$ and $g(t)$ with a time compression factor of two. Using this convolution technique it is possible to produce a real-time Fourier transform by using FM chirp waveforms as inputs to the SAW device. The inputs are then given by

$$f(t)e^{j(\omega t+\Delta t^2)} \text{ and } e^{j(\omega t+\Delta t^2)} \tag{3.19}$$

where $f(t)$ is the signal to Fourier transformed and 2Δ is the linear rate of change of the FM chirp's angular frequency. The output of the SAW device then yields

$$Kv\int_{t-\frac{L}{2v}}^{t+\frac{L}{2v}} f(\tau)e^{-j4t\Delta\tau}d\tau \tag{3.20}$$

which is the Fourier Transform for appropriate values of L and v (note that the scaled frequency is $4t\Delta$). The frequencies for which the Fourier transform is valid is related to the rate of change of the FM chirp and the length of the SAW device. Representing the right range of frequencies allows cancellation to be performed in the frequency domain.

Results presented in [Mils88][Mils80] demonstrate that transform domain processing can significantly improve system performance. As an example they found that a system with a processing gain of 31 and transform domain processing performs almost as well as a system with a processing gain of 255 which is almost a 10 dB improvement.

The results presented in [Mils88] used notching to remove the NBI. However it is also possible to suppress the interference by simply limiting the NBI power to a determined threshold. The trade off is leaving some NBI power in the signal versus removing UWB signal power. This is important depending on the output of the Fourier transformation. If the transformation produces significant side lobes in the narrowband interferer's spectrum then limiting is likely best so that removing too much UWB signal power is avoided.

3.2.4 Synchronization Assumptions

Depending on the type of interference cancellation technique used synchronization may or may not be needed. For example a decision feedback canceller assumes that synchronization of the desired signal can be performed since the symbol estimate is used in the cancellation. However the prediction filters do not suffer from this requirement. Synchronization can be performed after the cancellation of the interference. This is also true for the transform domain processing technique. The interference cancellation can be implemented on the front end and acquisition and synchronization can be performed after cancellation. However in any of the cases if the front end is overwhelmed than the desired signal may be pushed to far into the noise floor and the cancellation will not be able to negate this.

3.2.5 UWB Interference Cancellation

The previous narrowband interference cancellation techniques were discussed in the context of spread spectrum. Work focusing specifically on UWB is much less prevalent. However the topic has begun to garner much research attention since it will likely be vital to the operation of a UWB receiver. This section discusses several techniques that have been investigated for UWB communications and radar systems.

For the following discussion the received signal is assumed to be $x(k) = s(k) + i(k) + n(k)$ where *s(k)* represents the desired signal, *i(k)* represents the interference, and *n(k)* represents the noise.

First, techniques related to UWB synthetic aperture radar (UWB-SAR) will be discussed. Huang and Liang suggest a Gradual RELAX (GRELAX) approach in [Huan99]. The RELAX algorithm is used for sinusoidal estimation and is described in [Li96]. The RELAX algorithm is described by the following.

The interference is described by $i(k) = \sum_{n=1}^{N} \alpha_n e^{j2\pi f_n k}$.

Let, $\boldsymbol{\alpha} = [\alpha_1 \quad \alpha_2 \quad \cdots \quad \alpha_K]$ and $\Omega = [\omega(f_1) \quad \omega(f_2) \quad \cdots \quad \omega(f_K)]$. The parameter estimates are then given by

$$\left\{\hat{f}_k, \hat{\alpha}_k\right\} = \arg\min \left\{f_k, \alpha_k\right\} \quad \left\|x - \Omega\boldsymbol{\alpha}\right\|^2 . \tag{3.21}$$

Minimizing the right side of this equation with respect to α gives

$$\hat{\alpha} = \left(\Omega^H \Omega\right)^{-1} \Omega^H x . \tag{3.22}$$

The estimates of the frequencies $f = \left[f_1, f_2, \cdots, f_K\right]^T$ are found by minimizing

$$C_1\left(f_1, f_2, \cdots, f_K\right) = \left\|P_\Omega^\perp x\right\|^2 \tag{3.23}$$

where $P_\Omega^\perp$ stands for the orthogonal projector onto the null space of Ω^H . This gives

$$P_\Omega^\perp = \mathrm{I} - \Omega\left(\Omega^H \Omega\right)^{-1} \Omega^H . \tag{3.24}$$

The GRELAX algorithm suppresses the interference by applying the RELAX algorithm to a small number of sinusoids in stages. The GRELAX is described by the following steps as detailed in [Huan99].

1. Decide the number of stages *L* and the number of sinusoids in each stage *M*;
2. Take $x = \left[x(0), x(1), \cdots, x(N-1)\right]^T$ as the initial input of the RELAX algorithm at the first stage;
3. Estimate the parameters of the M sinusoids at the present stage using the RELAX algorithm;

4. Synthesize the estimated RFI with the estimate parameters 3 and subtract it from the input of the present stage. Take the residual value as the input of the RELAX algorithm at the next stage;
5. Repeat 3 and 4 until L stages have been processed.

They conclude that the GRELAX exhibits slightly reduced performance over the RELAX algorithm but that it has good computational efficiency and robustness.

Another suppression technique for UWB SAR is presented by Juhen, Vezzosi, and Le Goff in [Juhe99]. They suggest an LMS technique for suppression in UWB SAR measurements. For this algorithm the interference is described by

$$i(k) = \sum_{i=1}^{M} a_i \sin(w_i k) + \sum_{i=1}^{M} b_i \cos(w_i k). \tag{3.25}$$

Therefore $i(k)$ is estimated to minimize the quadratic error criterion $\sum_{k=0}^{N} \left| x(k) - i(k) \right|^2$.

This gives $\hat{i} = Az$ where the LMS problem is $Az = x$ with:

$$A = \begin{bmatrix} \sin(w_1 k_1) & \cos(w_1 k_1) & \cdots & \sin(w_M k_1) & \cos(w_M k_1) \\ \cdot & \cdot & \cdots & \cdot & \cdot \\ \cdot & \cdot & \cdots & \cdot & \cdot \\ \cdot & \cdot & \cdots & \cdot & \cdot \\ \sin(w_1 k_N) & \cos(w_1 k_N) & \cdots & \sin(w_M k_N) & \cos(w_M k_N) \end{bmatrix} \tag{3.26}$$

$$z = \begin{bmatrix} a_1 \\ b_1 \\ \cdot \\ \cdot \\ a_M \\ b_M \end{bmatrix}, \quad x = \begin{bmatrix} x(k_1) \\ x(k_2) \\ \cdot \\ \cdot \\ \cdot \\ x(k_N) \end{bmatrix}$$

The solution is found by finding $\hat{z}$ to minimize

$$J(z) = \left\| x - Az \right\|^2 = (x - Az)^t (x - Az) = x^t x - 2x^t Az + z^t A^t Az$$

Then $\hat{z} = \left(A^T A \right)^{-1} A^T x$ is found using the derivative expression $\frac{\partial J(z)}{\partial t} = -2x^t + 2z^t \left(A^t A \right) = 0$ and the LMS solution gives $\hat{i} = A\left(A^T A \right)^{-1} A^T x$ which then can be subtracted from the received signal. The authors simulated the performance and found that target recognition is greatly improved when implementing the suppression

algorithm. The simulation was conducted for an SIR = -18 dB and with 15 RF interferers.

The following discuss a couple techniques for UWB communications. Boubaker and Letaief analyze a MMSE Rake receiver for interference cancellation in [Boub03]. An advantage of this receiver is that it doesn't require knowledge of the interferer's parameters. A block diagram of the receiver is given in Figure 3.9.

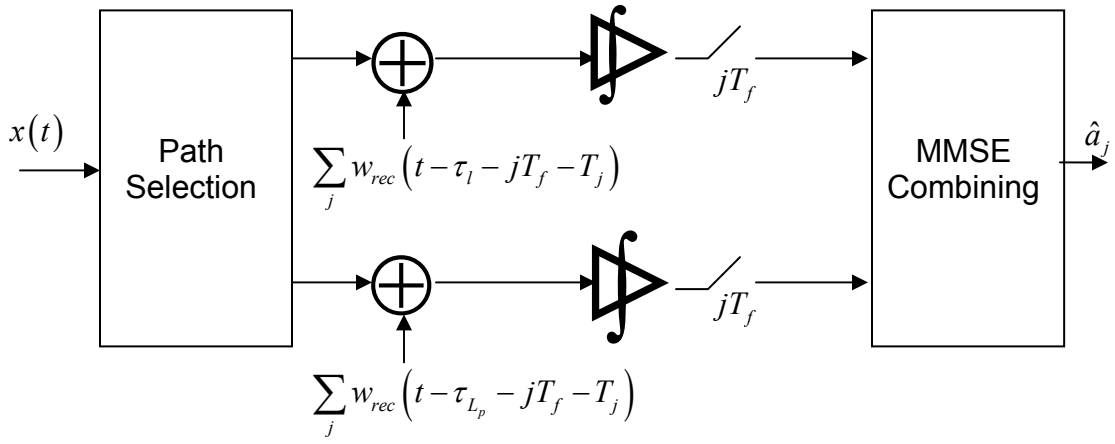

Figure 3.9 Rake Receiver MMSE Combiner

The receiver output is given by

$$\begin{aligned} y_{\lfloor j/N_s \rfloor} &= \sum_{l=0}^{L_p-1} \omega_l \left(a_{\lfloor j/N_s \rfloor} N_s \rho \sqrt{G_l} + \beta_l I_l + n_l \right) \\ &= \mathbf{w}^T \mathbf{r}_{\lfloor j/N_s \rfloor} \end{aligned} \tag{3.27}$$

where $\mathbf{r}_{\lfloor j/N_s \rfloor} = a_{\lfloor j/N_s \rfloor}\mathbf{S} + \beta\mathbf{I} + \mathbf{n}$. The MMSE linear combiner uses the weight vector $\mathbf{rw} = \left[\omega_0, \cdots, \omega_{L_p-1}\right]^T$ and the UWB and narrowband channel gain vectors are respectively defined as $\mathbf{S} = \rho N_s \left[\sqrt{G_0}, \cdots, \sqrt{G_{L_p-1}}\right]^T$ and $\beta = \left[\beta_0, \cdots, \beta_{L_p-1}\right]^T$. $\mathbf{I} = \left[I_0, \cdots, I_{L_p-1}\right]^T$ is the sampled narrowband interferer and $\mathbf{n} = \left[n_0, \cdots, n_{L_p-1}\right]^T$ is the sampled noise. The linear MMSE detector has the form of $\hat{\alpha}_{\lfloor j/N_s \rfloor} = \text{sgn}\left(y_{\lfloor j/N_s \rfloor}\right)$ where $\mathbf{w}$ is chosen to minimize the mean square error, given by $MSE = E\left[\left(\mathbf{w}^T \mathbf{r}_{\lfloor j/N_s \rfloor} - a_{\lfloor j/N_s \rfloor}\right)^2\right]$, and the MMSE weight vector $\mathbf{w}$ is given by $\mathbf{w}^* = \left(\mathbf{R}_S + \mathbf{R}_I + \mathbf{R}_N\right)^{-1}\mathbf{S}$. The authors simulated a realistic UWB channel and found that the Rake combining achieves acceptable performance even with SIR = -20 dB [Boub03].

Milstein and da Silva presented a spectral encoding technique in [Silv03]. The basic premise is to apply a spreading sequence, like CDMA, but in the frequency domain. Interference suppression can be accomplished by placing a spectral null in the waveform at the interferer's frequency. Figure 3.10 taken from [Silv03] illustrates this encoding.

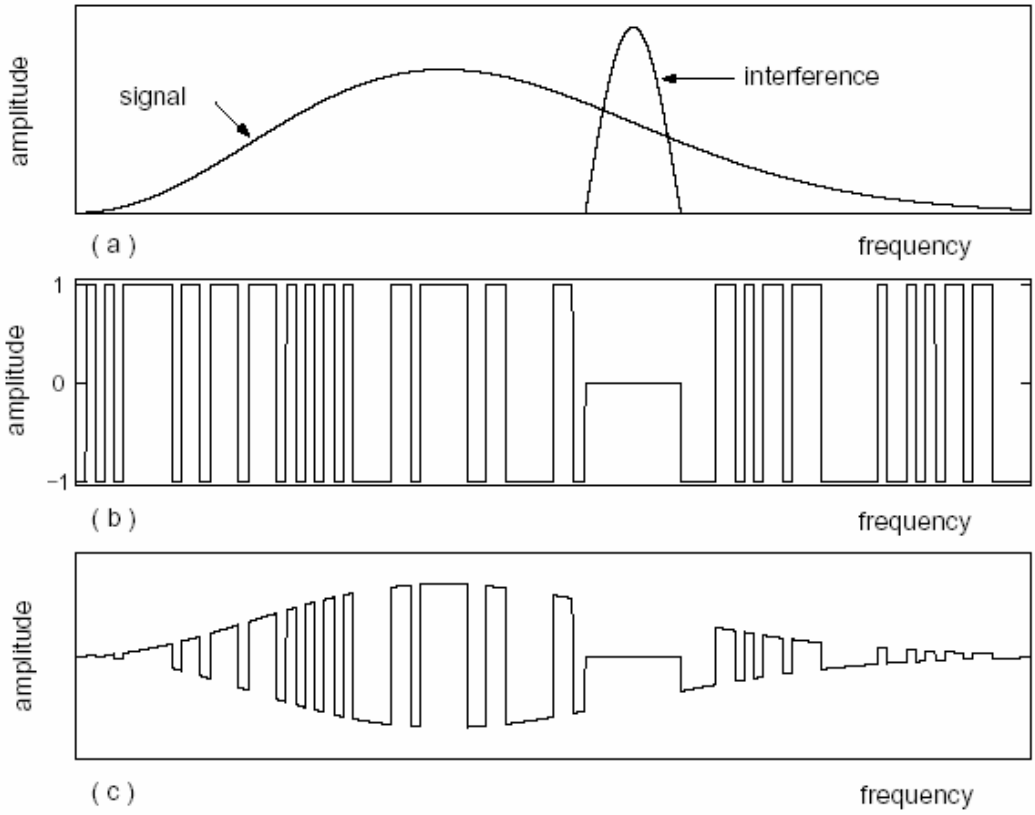

Figure 3.10 (a) Spectrum of signal and interference (b) Encoding sequence, and (c) Transmitted waveform.

Figure 3.11, taken from [Silv03], gives a block diagram of the basic transmitter and receiver operation. $PN(\omega)$ is the spreading sequence, and $F(\omega)$ is the Fourier transform of $f(t)$.

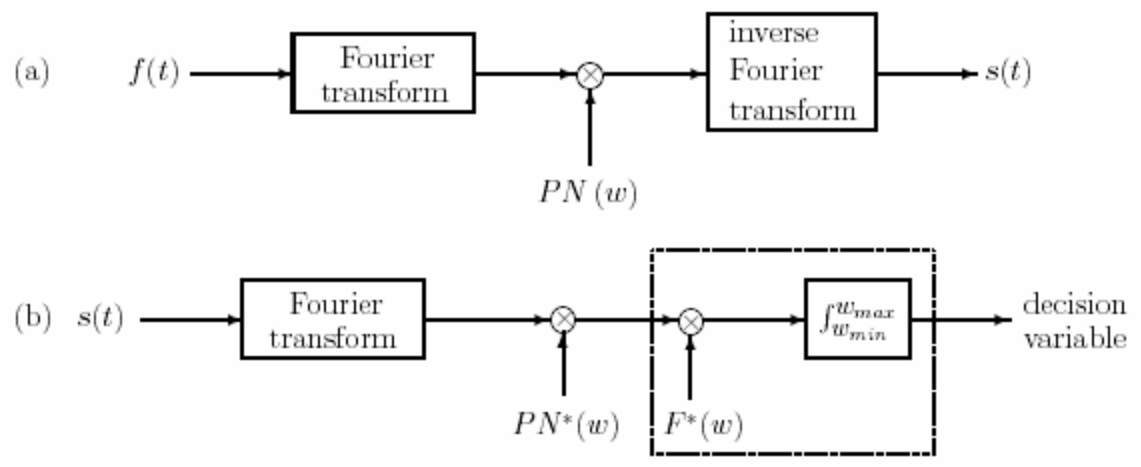

Figure 3.11 Bock diagrams of the (a) transmitter and (b) receiver

They propose to use SAW devices for the Fourier transform portion of the receivers as discussed in Section 3.2.3. They found that the system performance can be greatly improved using this technique and at an SIR value of -15 dB the signal approaches the normal BER curve without the narrowband interference. Note that this approach assumes that the frequency of the interferer is known.

3.3 Conclusion

This chapter provided an introduction to the impact of narrowband interference on UWB receivers. Narrowband interference can prevent acquisition and cause poor error performance. This motivates the need for front end narrowband interference suppression. Suppression techniques have been widely researched for DS-SS and those techniques have been introduced in this chapter. Several previous UWB techniques were also discussed. The subsequent chapters will provide an analysis of two interference suppression techniques for UWB. Chapter 4 will look at a combination analog-digital LMS algorithm that is similar in application to a LMS linear prediction filter. Chapter 5 will analyze the use of transform domain processing with SAW filters.

Chapter 4
Time Domain Front End NBIC

4.1 Introduction

Many digital signal processing techniques have been investigated to suppress or mitigate narrowband interference in the presence of a wideband signal. These techniques exist mainly for spread spectrum systems and since in principle the problem is the same for UWB, these techniques may also be applicable to UWB. Typically suppression is achieved using either linear or non-linear prediction filters and are purely digital. However current digital technology does not allow for a cost effective realization of a completely digital UWB system. It is therefore necessary to investigate techniques which are either purely analog or a combination of analog and digital. In this chapter we specifically investigate time-domain techniques which perform narrowband interference rejection in the RF front end. Note that this does not necessarily mean that the circuit is entirely analog. In fact, digital techniques can be used, but use sampling rates commensurate with the narrowband interferer bandwidth rather than the UWB signal bandwidth.

4.1.1 Approach 1: Single Tap LMS Cancellation

Figure 4.1 presents a block diagram for a combination analog and digital interference canceller that performs time domain cancellation in the RF front end. The circuit was previously presented in [McKi03a][McKi03b] and is similar to a circuit introduced in [Odli02]. The circuit attempts to track a narrowband interfering signal in the digital domain and then cancel it in the analog domain. The advantage of this approach is derived from the fact that the sampling and digital processing occur at a rate commensurate with the narrowband signal bandwidth, which is relatively low.

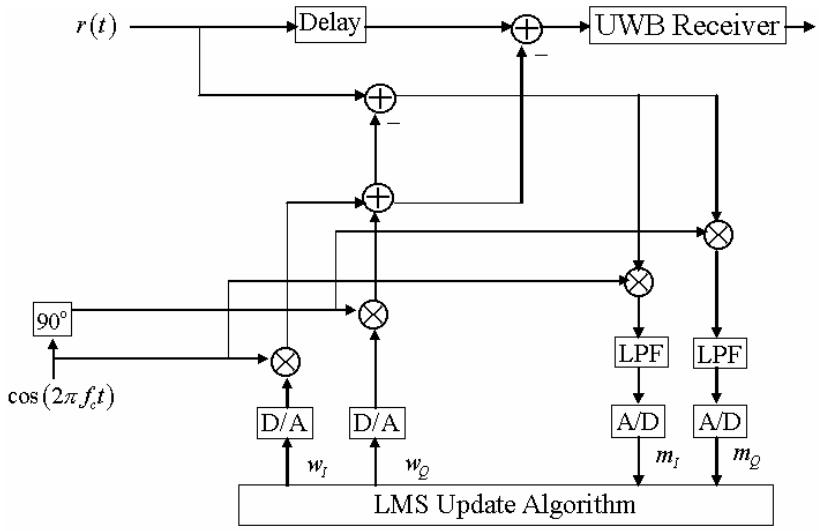

Figure 4.1 Time Domain Front End NBIC Circuit

The performance of the circuit is contingent on several factors. First, there are two stages which require the use of a mixer. The purpose of this mixer is to down-convert the incoming signal into an inphase (I) and quadrature (Q) representation allowing digital signal processing to be performed. Subsequently, the result of the digital algorithm must be up-converted in order to allow the interference cancellation to occur in the analog domain. An inherent assumption then is that the center frequency, f_c, of the narrowband interferer is known. It is desired to have an adaptive canceller which can operate on an interferer with unknown parameters. This therefore requires frequency estimation to be performed. An analysis of the ability to perform this frequency estimation is given in Section 4.2, in which a method of moments and a maximum likelihood estimation technique are investigated.

Now let's consider the performance of the digital portion of the circuit. Following the down-conversion, the resulting signal is lowpass filtered, sampled, and passed to a digital least mean squares (LMS) update algorithm. In this stage, the performance of the circuit (algorithm) is related directly to the strength of the narrowband interferer compared to the noise it observes, or the interference to noise ratio (INR). The INR of the cancellation circuit is determined by the thermal noise in the system and the noise contributed by the UWB signal. It was shown in [McKi03a][McKi03b] that after performing the lowpass filtering the noise contribution of the UWB signal can be properly modeled as AWGN. As a result, the combination of the UWB signal and thermal noise can simply be modeled as Gaussian noise.

Once the signal is down-converted and sampled, the narrowband interference is estimated using digital filter techniques. In the first approach the LMS algorithm is used along with a one-tap canceller to perform the interference estimation by successively updating the weights of the I and Q channels. This update is defined by

$$w_{X,j+1} = w_{X,j} + \lambda m_{X,j}, \quad X = I, Q \tag{4.1}$$

where λ is the weight update parameter ($0 < \lambda \leq 1$), m is the down-converted and filtered I or Q values, and w represents the I or Q weights used to estimate the narrowband signal. The inputs to the algorithm are then the previous weight approximations and the current I and Q message values, m_I and m_Q. Note that these message values are the I and Q values of an error signal. This error signal represents the difference between the actual and estimated interference. Therefore, at each iteration the algorithm attempts to minimize the error signal, eventually converging to a steady state, which provides the maximum amount of cancellation. The rate of convergence of the LMS algorithm is directly related to the weight update parameter, λ. The choice of λ is discussed in Section 4.3.

4.1.2 Approach 2: Multi-tap Transversal Filter Cancellation

The LMS algorithm is known to have slow convergence and therefore abrupt phase changes seriously degrade the interferer canceller's performance, making it particularly ineffective against modulated interference, especially BPSK and QPSK. This approach would likely be more amenable to continuous phase modulation. Therefore a second approach using a two-sided transversal filter (which performs much better with a modulated interferer), was also investigated. Figure 4.2 provides a diagram of the cancellation circuit used for the transversal filter.

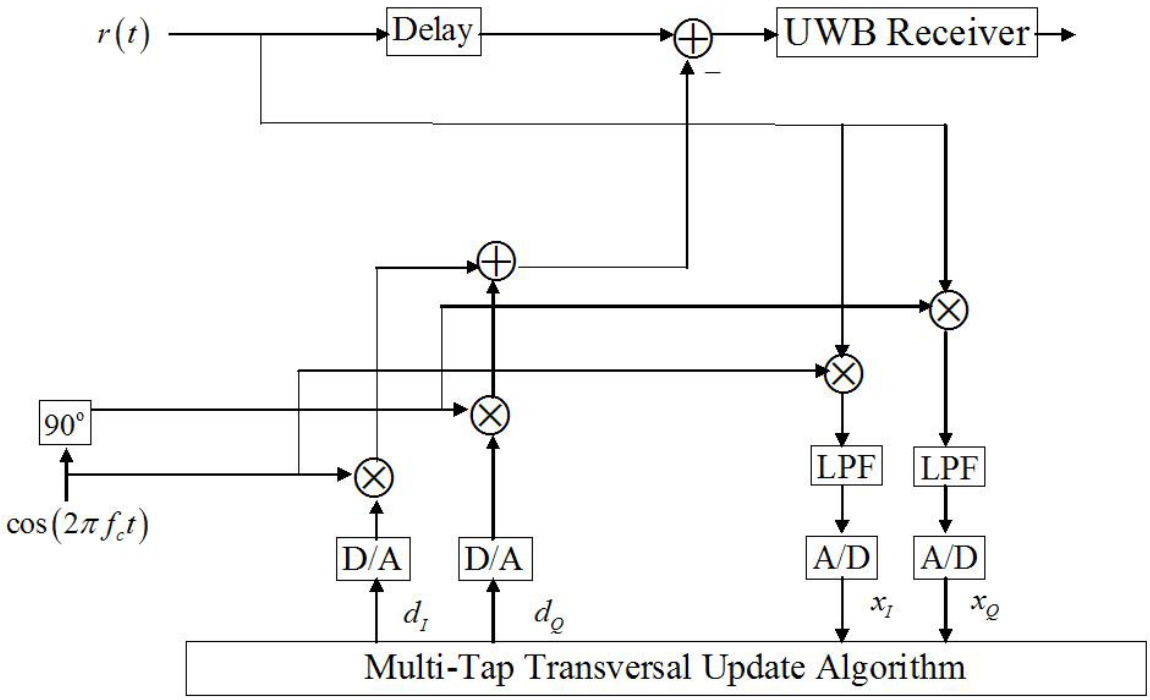

Figure 4.2 Multi-Tap Transversal Filter Cancellation Circuit

Figure 4.3 details the implementation of the transversal filter.

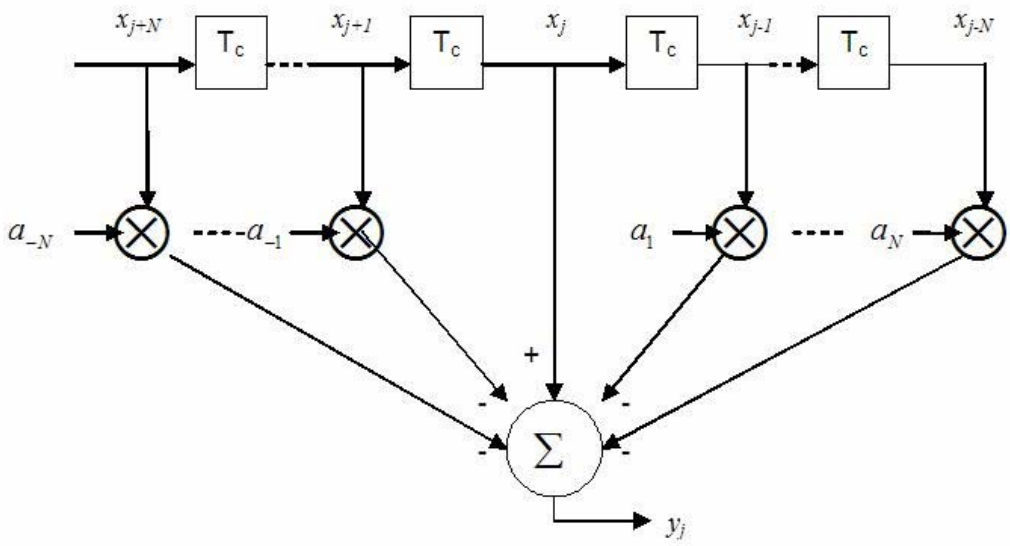

Figure 4.3 Transversal Filter

The filter performs the cancellation based on a block of past and future samples of the signal. The samples are populated by the A/D conversion in Figure 4.2. The delay given in the circuit therefore accounts for the processing delay of acquiring the N future samples and performing the calculations. Since the successive samples of the signal are highly correlated, the filter can predict the current sample of the narrowband interferer based on past and future values. The algorithm is implemented using the following steps.

1. Compute the estimate of the interferer, $d_j = a_j^T x$
2. Compute the error signal, $y_j = x_j - d_j$
3. Calculate the new filter weights, $a_j = a_{j-1} + \mu y x$

In the above steps x_j is the current received signal value, a_j is the vector of filter coefficients $\left[a_{-N} \cdots a_{-1}, a_1 \cdots a_N\right]$ and x is the vector of past and future received signal values $\left[x_{j-N} \cdots x_{j-1}, x_{j+1} \cdots x_{j+N}\right]$ for $N \neq 0$, as shown in Figure 4.3. The value T_c is the sample time. The output y_j represents the residual narrowband interference and noise. The value of d_j represents the estimate of the interferer. Based on this the weights are updated with every sample of the received signal and the output of the multi-tap transversal update algorithm is the estimate of the interferer, d_j. This value is then upconverted and subtracted from the received signal.

4.2 Frequency Estimation

A fundamental component of the digital LMS narrowband interference cancellation circuit is the ability to estimate the frequency of the interferer. The following discussion examines two frequency estimation techniques taken from [Kay93]. The first technique uses a method of moments and the second technique is the maximum likelihood estimator.

4.2.1 Method of Moments

In the method of moments technique, the received discrete time signal is assumed to be [Kay93]

$$x[n] = A\cos(2\pi f_0 n + \phi) + w[n] \qquad n = 0,1,...,N-1 \tag{4.2}$$

where $w[n]$ is zero mean white noise with variance σ^2 and f_0 is the frequency to be estimated. For this method of estimation the phase, ϕ, is considered to be uniformly distributed between zero and 2π, ($\phi \sim U[0,2\pi]$), and is independent of $w[n]$. Making this assumption allows $s[n] = A\cos(2\pi f_0 n + \phi)$ to be treated as a realization of a wide sense stationary (WSS) random process. To verify this assumption the mean and autocorrelation of $s[n]$ are examined. The expected value of the signal is given by

$$\begin{aligned} E\{s[n]\} &= E\{A\cos(2\pi f_0 n + \phi)\} \\ &= \int_0^{2\pi} A\cos(2\pi f_0 n + \phi)\frac{1}{2\pi}d\phi = 0 \end{aligned} \tag{4.3}$$

and the autocorrelation is given by

$$\begin{aligned} r_{ss}[k] &= E\{s[n]s[n+k]\} \\ &= E\{A^2\cos(2\pi f_0 n + \phi)\cos(2\pi f_0 (n+k) + \phi)\} \\ &= A^2 E\left\{\frac{1}{2}\cos(4\pi f_0 n + 2\pi f_0 k + 2\phi) + \frac{1}{2}\cos(2\pi f_0 k)\right\} \\ &= \frac{A^2}{2}\cos(2\pi f_0 k) \end{aligned} \tag{4.4}$$

The autocorrelation of the white noise, $w[n]$, is given by $r_{ww}[k] = \sigma^2\delta[k]$ and therefore using the result of equation (4.4) the autocorrelation of the received signal, $r_{xx}[k]$, becomes

$$r_{xx}[k] = \frac{A^2}{2}\cos(2\pi f_0 k) + \sigma^2 \delta[k] \tag{4.5}$$

In order to estimate the frequency using the method of moments $r_{xx}[1]$ is used . This is given by

$$r_{xx}[1] = \frac{A^2}{2}\cos(2\pi f_0) \tag{4.6}$$

This allows the estimation to be performed without knowledge of the noise variance. An estimate of the frequency is then given by

$$\hat{f}_0 = \frac{1}{2\pi}\arccos\left[\frac{\hat{r}_{xx}[1]}{A^2/2}\right] \tag{4.7}$$

where the autocorrelation $r_{xx}[1]$ is estimated by

$$\hat{r}_{xx}[1] = \frac{1}{N-1}\sum_{n=0}^{N-2} x[n]x[n+1] \tag{4.8}$$

In equation (4.7) the term representing the average power of the sinusoid, $A^2/2$, must also be estimated. This estimation is given by

$$\frac{A^2}{2} = \frac{1}{N}\sum_{n=0}^{N-1} x^2[n] \tag{4.9}$$

and the frequency, f_0, is finally estimated using

$$\hat{f}_0 = \frac{1}{2\pi}\arccos\left[\frac{\frac{1}{N-1}\sum_{n=0}^{N-2} x[n]x[n+1]}{\frac{1}{N}\sum_{n=0}^{N-1} x^2[n]}\right] \tag{4.10}$$

Note that the estimate of f_0 is the normalized frequency of the signal (f_0/F_s where F_s is the sampling frequency) such that the estimate found for f_0 is between 0 and ½. In [Kay93] it is shown that for a high SNR this method has an expected value which is equal to f_0. Kay also provides an expression for the variance of the estimation that highlights limitations of this method. It is noted that the variance of the estimate decreases most rapidly for increasing block size for f_0 = ¼ while for f_0 near 0 and ½ the variance decreases much less rapidly. This results from the use of the arccos() function in the estimation. This can be seen in Figure 4.4. Observe that slight variations in the value of x[n] near the points -1 and 1 cause large variations in the output due to the steepness of the curve near those values.

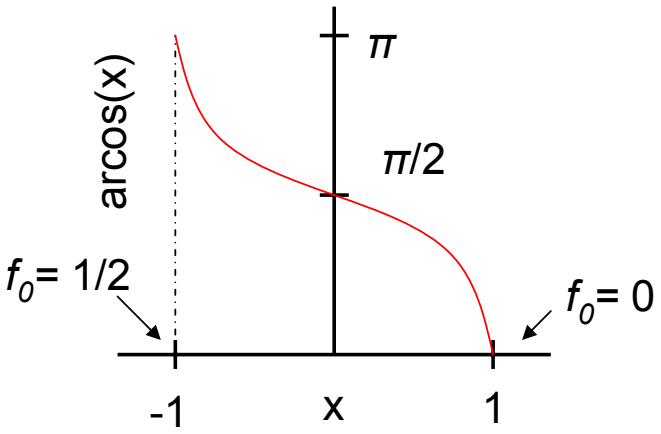

Figure 4.4 Evaluation of Arccos

4.2.2 Maximum Likelihood Estimation

The second frequency estimation technique considered uses a maximum likelihood estimator derived from the PDF of the received signal. Again the received signal is taken as

$$x[n] = A\cos(2\pi f_0 n + \phi) + w[n] \qquad n = 0,1,...,N-1$$

which results in the PDF of w

$$\begin{aligned} p(w) &= \frac{1}{(2\pi\sigma^2)^{\frac{N}{2}}} \exp\left[-\frac{1}{2\sigma^2}\sum_{n=0}^{N-1}(w[n])^2\right] \\ &= \frac{1}{(2\pi\sigma^2)^{\frac{N}{2}}} \exp\left[-\frac{1}{2\sigma^2}\sum_{n=0}^{N-1}(x[n]-A\cos(2\pi f_0 n+\phi))^2\right] \end{aligned} \tag{4.11}$$

where $A > 0$, and $0 < f_0 < 1/2$. The maximum likelihood estimate of f_0 is then found by maximizing *p(w)* or minimizing the argument of the exponential in the PDF with respect to f_0. Therefore the following expression needs to be minimized [Kay93]

$$\begin{aligned} J(A, f_0, \phi) &= \sum_{n=0}^{N-1}(x[n]-A\cos(2\pi f_0 n+\phi))^2 \\ &= \sum_{n=0}^{N-1}(x[n]-A\cos\phi\cos(2\pi f_0 n)+A\sin\phi\sin(2\pi f_0 n))^2 \end{aligned} \tag{4.12}$$

By letting

$$c = \begin{bmatrix} 1 & \cos 2\pi f_0 \ldots \cos 2\pi f_0 (N-1) \end{bmatrix}^T$$
$$s = \begin{bmatrix} 0 & \sin 2\pi f_0 \ldots \sin 2\pi f_0 (N-1) \end{bmatrix}^T$$

and transforming J into a quadratic using the following transformation

$$\alpha_1 = A\cos\phi$$
$$\alpha_2 = A\sin\phi$$

the following relationship is given

$$\begin{aligned} J'(\alpha_1, \alpha_2, f_0) &= (\mathrm{x} - \alpha_1 \mathrm{c} - \alpha_2 s)^T (\mathrm{x} - \alpha_1 \mathrm{c} - \alpha_2 \mathrm{s}) \\ &= (\mathrm{x} - \mathrm{H}\alpha)^T (\mathrm{x} - \mathrm{H}\alpha) \end{aligned} \tag{4.13}$$

where $\alpha = \begin{bmatrix} \alpha_1 \alpha_2 \end{bmatrix}^T$ and $\mathrm{H} = \begin{bmatrix} \mathrm{cs} \end{bmatrix}^T$. It is shown in [Kay93] that the minimizing solution for equation (4.13) is given by

$$\hat{\alpha} = \left(\mathrm{H}^{\mathrm{T}}\mathrm{H}\right)^{-1} \mathrm{H}^{\mathrm{T}}\mathrm{x} \tag{4.14}$$

which results in

$$\begin{aligned} J'(\hat{\alpha}_1, \hat{\alpha}_2, f_0) &= (\mathrm{x} - \mathrm{H}\hat{\alpha})^T (\mathrm{x} - \mathrm{H}\hat{\alpha}) \\ &= \left(\mathrm{x} - \mathrm{H}\left(\mathrm{H}^T\mathrm{H}\right)^{-1} \mathrm{H}^T\mathrm{x}\right)^T \left(\mathrm{x} - \mathrm{H}\left(\mathrm{H}^T\mathrm{H}\right)^{-1} \mathrm{H}^T\mathrm{x}\right) \\ &= \mathrm{x}^T \left(\mathrm{I} - \mathrm{H}\left(\mathrm{H}^T\mathrm{H}\right)^{-1} \mathrm{H}^T\right)\mathrm{x} \end{aligned} \tag{4.15}$$

since $\mathrm{I} - \mathrm{H}\left(\mathrm{H}^T\mathrm{H}\right)^{-1} \mathrm{H}^T$ is an idempotent matrix. In order to estimate the frequency f_0, equation (4.15) needs to be minimized or accordingly the following needs to be maximized [Kay93]:

$$\mathrm{x}^T\mathrm{H}\left(\mathrm{H}^T\mathrm{H}\right)^{-1} \mathrm{H}^T\mathrm{x} \tag{4.16}$$

Upon substitution of the definition of H this yields

$$\begin{bmatrix} \mathrm{c}^T\mathrm{x} \\ \mathrm{s}^T\mathrm{x} \end{bmatrix}^T \begin{bmatrix} \mathrm{c}^T\mathrm{c} & \mathrm{c}^T\mathrm{s} \\ \mathrm{s}^T\mathrm{c} & \mathrm{s}^T\mathrm{s} \end{bmatrix}^{-1} \begin{bmatrix} \mathrm{c}^T\mathrm{x} \\ \mathrm{s}^T\mathrm{x} \end{bmatrix} \tag{4.17}$$

Finding the maximum value of equation (4.16) according to f_0 determines the MLE estimate for f_0.

4.2.3 Simulation Comparison

The following serves to compare the performance of the method of moments and MLE estimation techniques. The performance is measured in terms of the mean and variance of the estimates for different values of SNR (SNR values are determined relative to the tone's average power). It is common that these techniques will show improved performance for increasing block size. The comparison therefore examines block sizes of 20, 40, 80, and 160 samples.

Method of Moments

Recall the discussion concerning the method of moments estimate from Section 4.2.1. It was mentioned that as f_0 approaches 0 the variance is expected to become increasingly worse. Figure 4.5 compares the effect of increasing the sampling rate (therefore decreasing f_0) on the estimate variance for a tone with f_c = 2.5 GHz. Notice that as f_0 approaches 0 the variance becomes increasingly worse. For demonstration purposes this comparison was computed assuming the amplitude of the tone was known, as in equation (4.7). The variance also exhibits the same behavior when the amplitude must be estimated (as given by equation (4.8)) but the mean estimate of the frequency becomes much worse as well. Figure 4.6 displays the method of moments mean estimates for increasing sampling rates, again for f_c = 2.5 GHz. As SNR increases the mean converges towards the correct value but at SNR = 10 dB the higher sampling rate estimates are still considerably poor. Notice that for $F_s = 4F_c$ the variance and mean are considerably better than the other cases. As mentioned this is expected since f_0 = ¼ when $F_s = 4F_c$. The following analysis therefore only examines f_0 = ¼ for the methods of moments.

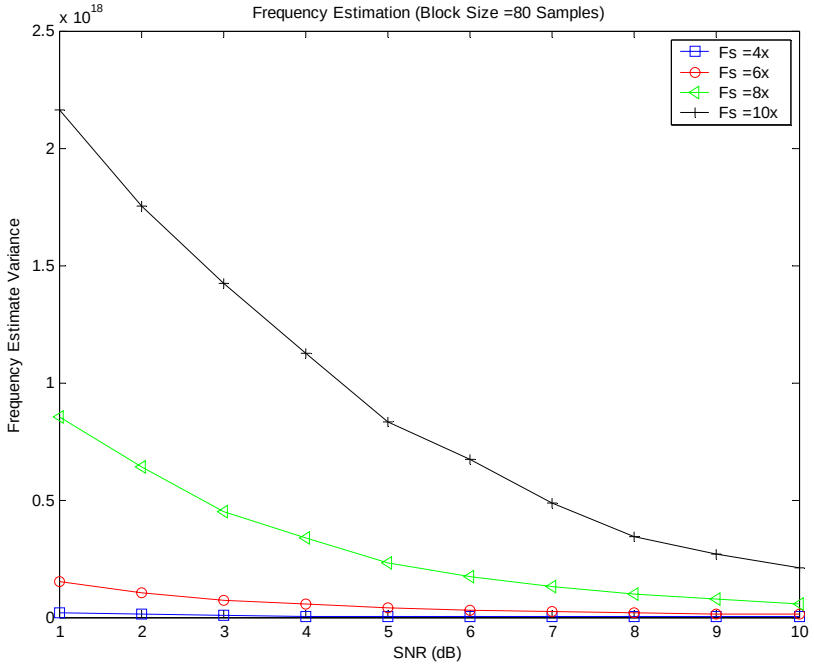

Figure 4.5 Method of Moments Estimate Variance vs. SNR

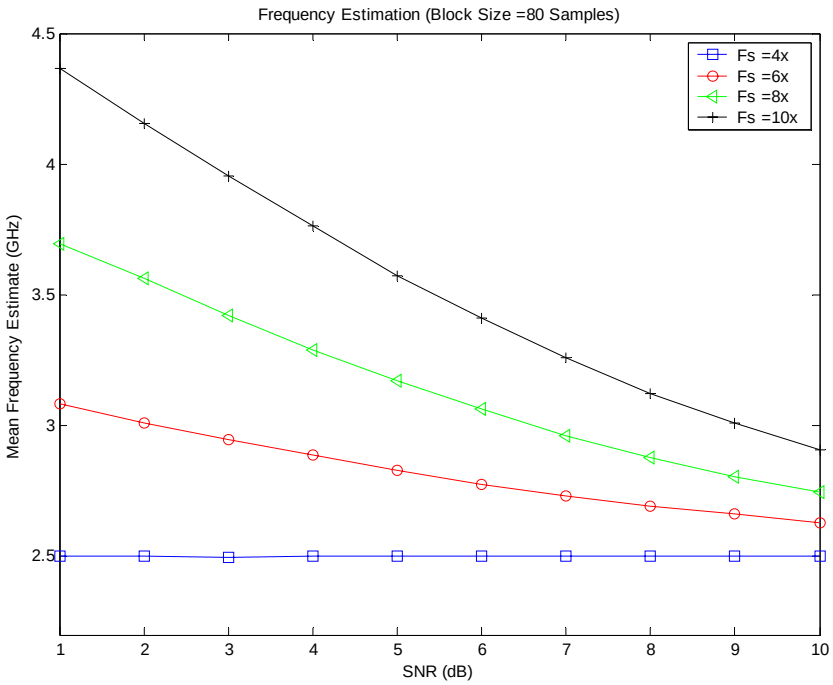

Figure 4.6 Method of Moments Estimate Mean vs. SNR

Figures 4.7 and 4.8 present the mean and variance respectively as a function of block size and SNR for the method of moments.

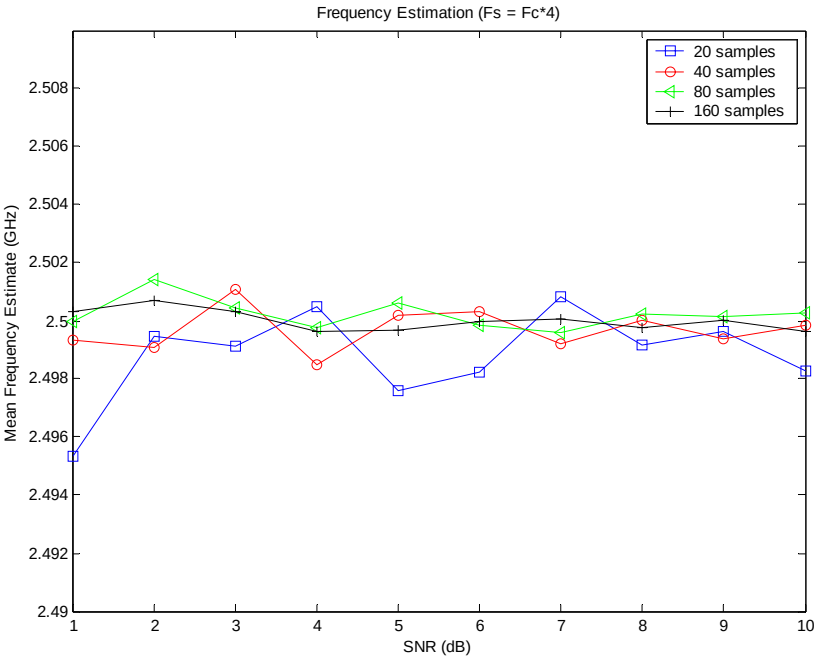

Figure 4.7 Method of Moments Estimate Mean vs. Block Size for $F_s = 4F_c$

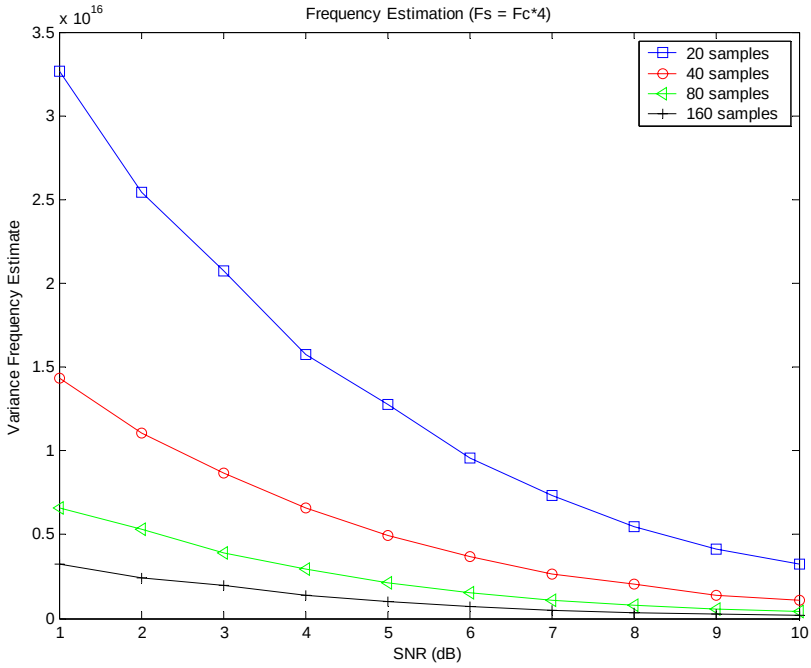

Figure 4.8 Method of Moments Estimate Variance vs. Block Size for $F_s = 4F_c$

As expected the variance decreases with an increase in block size and also as SNR increases. The mean slightly deviates from 2.5 GHz and is more evident for the smaller block sizes. Note however that the simulation results represent an average taken over 5000 iterations per SNR value. Running the simulation over a much larger number of iterations would likely bring the mean values even closer to the actual estimate. In an attempt to quantify and compare techniques, Table 4.1 below gives the standard deviation, σ, of the estimate along with its percentage of the sampling frequency (σ/F_c) for F_c = 0.5, 0.9, and 2.5 GHz ($F_s = 4F_c$)with SNR values of 5 and 10 and a block size of 160 samples. Table 4.2 provides the same for a block size of 20 samples. It is observed that with the SNR = 5 dB that a block size of 160 samples outperforms the case for the SNR = 10 dB and a block size of 20 samples.

Table 4.1 Frequency Estimate Standard Deviation, $F_s = 4\ F_c$, Block Size = 160 Samples

	SNR = 5 dB			SNR = 10 dB	
F_c (GHz)	σ (MHz)	% F_c		σ (MHz)	% F_c
0.5	6.35	1.27		2.55	0.51
0.9	11.28	1.25		4.70	0.52
2.5	31.88	1.28		12.91	0.52

Table 4.2 Frequency Estimate Standard Deviation, $F_s = 4\ F_c$, Block Size = 20 Samples

	SNR = 5 dB			SNR = 10 dB	
Fc (GHz)	σ (MHz)	% Fc		σ (MHz)	% Fc
0.5	22.61	4.52		11.38	2.28
0.9	40.11	4.46		20.65	2.29
2.5	113.14	4.53		56.78	2.27

Maximum Likelihood Estimation

A similar analysis is provided for maximum likelihood estimation (MLE) as was given for the method of moments technique. As would be expected block size again reduces the variance of the estimate. Figures 4.9 and 4.10 provide plots of the estimate mean and variance for increasing block size with a sampling rate of $F_s = 8F_c$. Due to the lengthy program runtime required to simulate this estimation, the simulation could only be run over 200 iterations per SNR value. Therefore the plot of the mean is a little noisy, however for more iterations the plots are expected to more closely estimate the actual frequency.

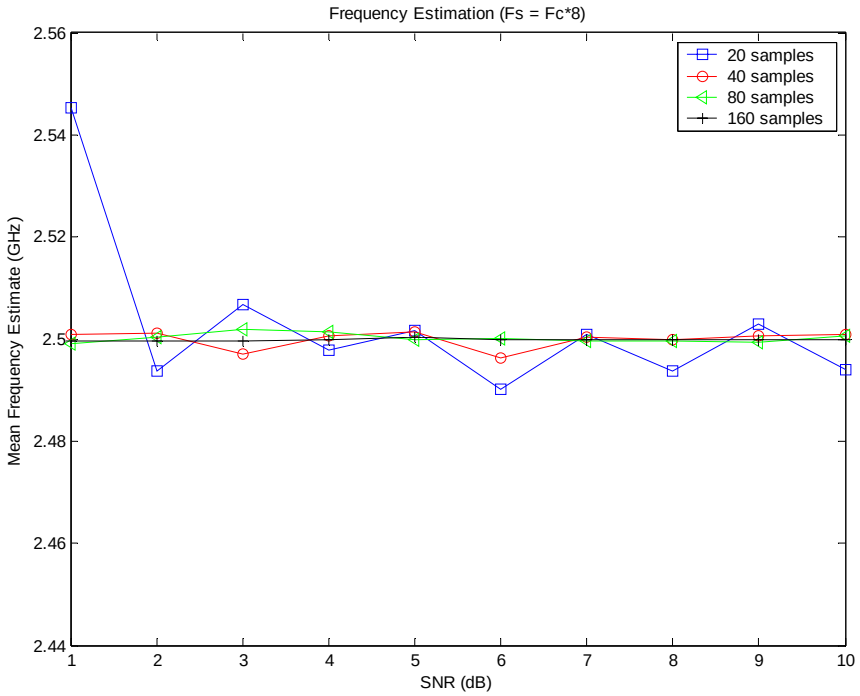

Figure 4.9 Maximum Likelihood Estimate Mean vs. Block Size for $F_s = 8F_c$

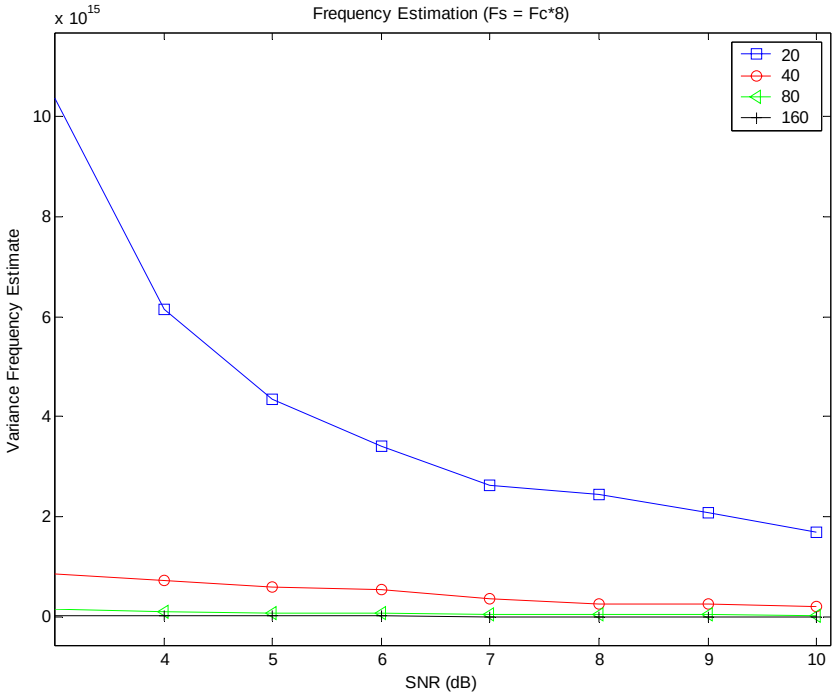

Figure 4.10 Maximum Likelihood Estimate Variance vs. Block Size for $F_s = 8F_c$

It is also of interest to examine the effect of the sampling frequency. Unlike the method of moments estimation, the MLE does not see a change in the mean estimate as the sampling rate increases (as f_0 approaches 0) but it does exhibit the same type of increase in variance. In order to better demonstrate the trade off between sampling frequency and block size, Table 4.3 provides the mean and variance values for increasing block size and sampling rate for an SNR values of 10 dB. Examining the mean values it can be seen that they all display similar accuracy. However examining the variance it is observed that the values increase with sampling rate and decreased block size but are much more sensitive to block size.

Table 4.3 MLE Mean and Estimate Values for SNR = 10 dB

		MLE Estimate Mean (SNR = 10 dB)				MLE Estimate Variance (SNR = 10 dB)			
		Relative Sampling Frequency				Relative Sampling Frequency			
		4	6	8	10	4	6	8	10
Block Size	20	2.4989	2.4990	2.4941	2.5035	408566.8	796205.8	1683976.3	2574540.0
	40	2.4998	2.5002	2.5009	2.5001	43741.7	101828.4	198946.6	311004.9
	80	2.5002	2.5003	2.5005	2.5000	6209.8	15398.1	25587.0	37845.3
	160	2.5000	2.5000	2.4998	2.5000	762.9	2120.0	3592.4	4708.5

* Values are in GHz

*Values are 10^9

Tables 4.4 and 4.5 provide the standard deviation of the estimate along with its percentage of the center frequency. These are given for F_c = 0.5, 0.9, and 2.5 GHz with an SNR = 5 dB and 10 dB and for block sizes of 160 and 20 samples respectively.

Table 4.4 Frequency Estimate Standard Deviation, $F_s = 4\ F_c$, Block Size = 160 Samples

	SNR = 5 dB			SNR = 10 dB	
Fc (GHz)	σ (MHz)	% Fc		σ (MHz)	% Fc
0.5	0.33	0.07		0.17	0.03
0.9	0.55	0.06		0.34	0.04
2.5	1.65	0.07		0.87	0.03

Table 4.5 Frequency Estimate Standard Deviation, $F_s = 4\ F_c$, Block Size = 20 Samples

	SNR = 5 dB			SNR = 10 dB	
Fc (GHz)	σ (MHz)	% Fc		σ (MHz)	% Fc
0.5	6.84	1.37		4.04	0.81
0.9	12.68	1.41		6.81	0.76
2.5	34.19	1.37		20.21	0.81

Conclusion

Comparing the two methods reveals that the mean estimates are fairly comparable but that the MLE technique offers an estimate which has a much lower standard deviation when compared to the method of moments. This suggests that MLE should be the method of choice. However the maximum likelihood estimation calculations are computational intensive simply because of the matrix inversion involved. Also the matrix inversion will increase in difficulty as the block size increases. In practice this would need to be taken into consideration. So for high SNR scenarios it may be acceptable to use the method of moments. Averaging could also be used to improve the estimate. It also should be noted that the Method of Moments technique provides fairly good estimation.

Note also that these results tend to suggest that a very high sampling rate is required to estimate the interference. In practice however the signal could be down-converted to an intermediate frequency using a nominal value. This does not affect the estimation of the frequency but eases sampling rate requirements for the system. Also note that these estimation techniques do not account for multiple interferers.

4.3 Simulation Assumptions

The results presented later in this chapter attempt to quantify the performance of the narrowband canceller in terms of bit error rate (BER). Before presenting those results it is important to provide the general assumptions and definitions used in the simulations.

In general the simulation is performed in two separate blocks, baseband and RF. The motivation for this approach is simply to ease the processing burden on the simulation. The NBIC can be performed using complex baseband. The residual interference resulting from the cancellation is then injected into the UWB demodulation. Figure 4.11 provides the general simulation flow.

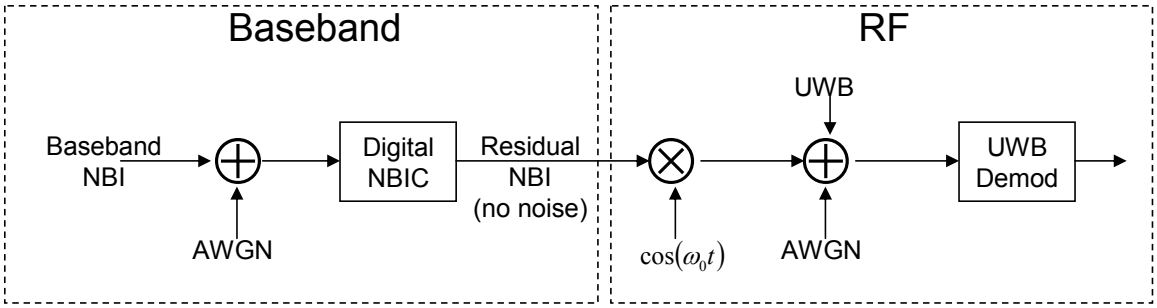

Figure 4.11 Time Domain Front End NBIC Simulation Flow

4.3.1 Noise and Interference

The most important definitions are in regards to calibrating the addition of noise to the system. Note that all BER simulations performed relate the error performance as a function of signal to interference ratio (SIR) for a given signal to noise ratio (SNR). The SNR for the system is defined as

$$SNR = \frac{E_b}{N_0} \tag{4.18}$$

where E_b is the energy per bit of the UWB system and N_0 is the noise power spectral density. Note that it was assumed that each bit was represented by a single pulse and therefore the energy per bit is given by the energy in one pulse. The energy per pulse is always normalized to one. SIR then is defined as the ratio of the UWB signal energy to the narrowband interferer energy. For these simulations narrowband signal energy was defined as a function of the pulse repetition rate (PRR), i.e. the number of UWB pulses per second, and the spreading gain of the UWB system. PRR refers to the number of pulses transmitted per second and spreading gain refers the number of pulses representing a single bit. However as previously mentioned the spreading gain is simply one and therefore is not a factor in the calculation of SIR. (The effects of spreading gain will be further discussed with the results.) Therefore, SIR is then simply a function of PRR and is defined as

$$SIR = \frac{E_b}{E_t} \tag{4.19}$$

where E_t is the energy in the tone. E_t is defined by

$$E_t = \sum_{n=0}^{N-1} \sin^2\left(2\pi \frac{n}{F_s}\right) \quad \text{where } N = \frac{F_s}{PRR} \tag{4.20}$$

where Fs is the sampling frequency. Energy is therefore calculated over the interval $\frac{1}{PRR}$. This calculation is also identical to the ratio of the average UWB power to the average interferer power.

As noted, the simulator was constructed by combining a complex baseband simulation block with an RF simulation block. The complex baseband block performs the interference estimation using either the LMS algorithm or the transversal filter. This was accomplished by representing the down-converted I and Q channels of the narrowband interferer in complex baseband notation in which case the channels are represented by

$$\begin{aligned} I &= A\cos(\phi) \\ Q &= A\sin(\phi) \end{aligned} \tag{4.21}$$

where ϕ is the random phase term of the narrowband interferer.

So to keep the noise power consistent in the separate simulation blocks noise was added to the complex baseband samples based on the specified SNR for the UWB signal. The ratio of the energy in the interferer to this noise is referred to as the interference to noise ratio (INR). The value of INR is not directly used to add noise to the system but for comparison purposes, some means of quantifying the INR ratio is necessary. INR is therefore defined as

$$INR_{dB} = SNR_{dB} - SIR_{dB} \tag{4.22}$$

4.3.2 LMS Cancellation Algorithm

After adding noise, the LMS portion of the simulation is performed, producing as its output the error signal of the LMS algorithm. This error signal represents the residual narrowband interferer power after cancellation.

Before moving on to the description of the RF simulation block it is important to describe the effect the noise has on the choice of λ. As mentioned in the introduction given in Section 4.1.1, the value of λ directly impacts the rate of convergence of the LMS algorithm and therefore the ability of the circuit to cancel the interference. The performance of the circuit is obviously also affected by the noise in the system and consequently the noise affects the choice of λ. For instance, if the system has a poor INR value, then a large λ will cause large fluctuations in the estimate of the interference and will actually add interference to the system. In this situation it is more advantageous to have a smaller value of λ thereby letting the algorithm gradually converge. The converse is also true. In a high INR scenario it is suboptimal to have a lower value of λ as the

system will converge very slowly and the full potential of the algorithm will not be realized. It is better to have a larger value of λ letting the error converge faster and canceling more of the interference. Therefore depending on the INR there exists an optimum λ that provides the maximum amount of interference cancellation. Quantifying this optimum λ is most precisely done by measuring the mean of the LMS error signal. This signal directly reflects the amount of cancelled interference. Simulations were run using a 400 kHz sampling rate and a PRR = 1 MHz. Note that using the provided definition of INR, changing the PRR will simply shift the plots. Specifically, increasing the PRR, which corresponds to an increase in interferer amplitude for the same SIR value, provides the same results for lower values of INR. Decreasing the PRR will cause a shift to higher values of INR. Figure 4.12a plots the optimum λ value versus INR for a tone interferer using the definition given in equation (4.22). Figure 4.12b plots the corresponding mean of the error signal in dB. Similarly, Figure 4.13 plots the same information for a QPSK signal with a data rate of 10 kHz. Note that there is a difference in the λ versus INR relationship for a tone and a modulated interferer. The modulated interferer requires a larger λ value for a smaller value of INR. Due to the need to track the interferer when there is an abrupt change in the phase of the interferer (i.e. a change in the symbol) the λ value must be larger in order to change more rapidly. Notice that there is also a decrease in the amount of cancelled narrowband interference, which directly relates to a worsening in BER performance.

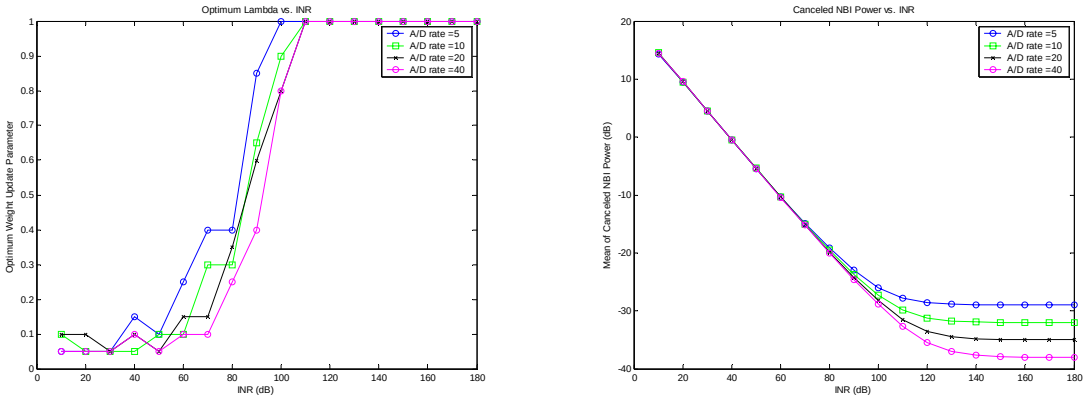

(a) (b)

Figure 4.12 Tone Interferer (a) Optimum λ vs. INR and (b) Mean of Error Signal

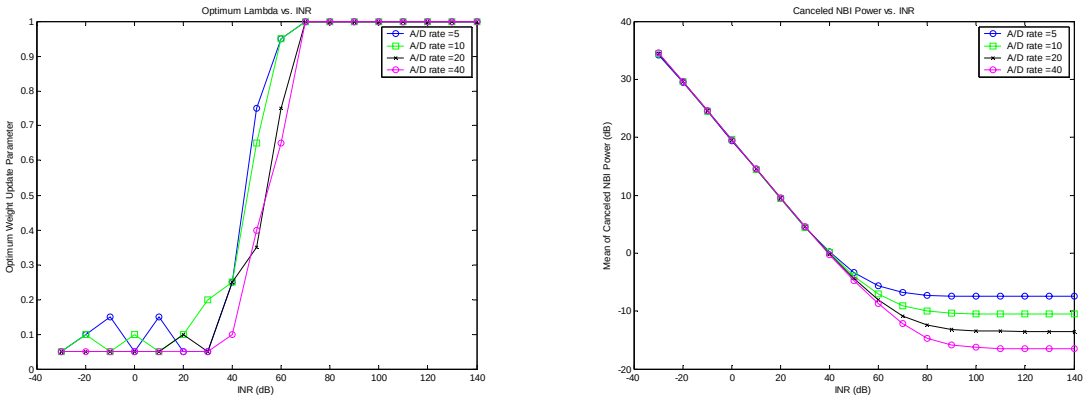

(a) (b)

Figure 4.13 QPSK Interferer (a) Optimum INR vs. λ and (b) Mean of Error Signal

4.3.3 Transversal Filter Cancellation

The transversal filter simulation is performed using the same methodology as the LMS cancellation. The cancellation blocks are simply interchanged. The addition of noise is handled in the exact same manner as previously described. Note also that the modulated interference was created using a square root raised cosine pulse shape with a roll-off factor of 0.35 and a symbol overlap of 10 symbols, since this represents a practical implementation.

4.3.4 UWB Demodulation

The RF simulation block performs the UWB demodulation and consequently determines the error performance of the system. Demodulation is performed in two types of channels, a purely AWGN channel and an AWGN channel with multipath. Regardless of the channel the samples of the error signal are converted into an RF narrowband signal and added to the UWB signal.

The demodulation procedure in the AWGN channel is rather straightforward. A unit energy pulse is corrupted by both the addition of Gaussian noise and the appropriate level of narrowband interference (either the original narrowband interferer or the residual of the LMS cancellation). Correlation is subsequently performed using a unit energy pulse and the error performance is calculated.

The demodulation of the multipath channel is less straightforward. First the channel is described. The multipath channel is simulated using a channel impulse response (CIR) of the form (as described in Chapter 2)

$$h(t) = \sum_{k=0}^{N-1} a_k \delta(t - t_k)$$

where the polarity of a_k is determined by a binary random variable. In Chapter 2, modeling results were presented based on CIRs of this form. These results were extracted from actual indoor line of sight (LOS) and non-line of sight (NLOS) measurements. [Venk04] presented a channel model based on these measurements which could be used to statistically emulate the measured channel. This model is referred to as the Split-Poisson model and is used to generate the CIR for the results presented in this work. The Split-Poisson model is similar in definition to the common Saleh-Valenzuela indoor channel model [Sale87] except that it defines multipath as arriving in two clusters, where the Saleh-Valenzuela model randomly determines the number of multipath clusters. For the Split-Poisson model each cluster is defined by the arrival of paths according to a Poisson distribution meaning that the paths have exponential inter-arrival times. The probability distribution of the *k*th path within a cluster is then defined by

$$p\left(\tau_k \mid \tau_{(k-1)}\right) = \lambda \exp\left[-\lambda\left(\tau_k - \tau_{(k-1)}\right)\right], \quad k > 0 \tag{4.23}$$

in which *k* paths are generated according to the mean arrival rate λ. The path amplitudes within a cluster are assumed to decay exponentially and therefore the mean path amplitudes are given by

$$\beta_k = e^{-\tau_k/\gamma} \tag{4.24}$$

where γ defines the rate of decay for the cluster. The amplitudes of these paths have been shown to follow a log-normal distribution about their expected value and therefore the path amplitudes varied according to the standard deviation of the distribution, σ. The Split-Poisson model creates a CIR by generating two separate clusters defined by the parameters $\left[\lambda_1, \gamma_1, \sigma_1\right]$ and $\left[\lambda_2, \gamma_2, \sigma_2\right]$ respectively. These clusters are then added together with the second cluster delayed by time, t_1. The first cluster is expected to have greater amplitude and is therefore scaled by a factor α in order to keep the decay of energy consistent. For the performed simulations the parameter values were set to those which matched the NLOS Bicone measurement data. These values were $\lambda_1 = 1/4\times10^{-9}$, $\gamma_1 = 18\times10^{-9}$, $\sigma_1 = 3.3$, $\lambda_2 = 1/0.9\times10^{-9}$, $\gamma_2 = 22\times10^{-9}$, and $\sigma_2 = 6$.

When using the multipath channel it is desired to obtain performance curves which represent the average performance of the statistical channel model (Note that all CIRs are normalized to unit energy so as to not artificially add energy to the received signal). In order to obtain the average performance of the multipath channel a total of 1000 CIRs were generated for each SIR value. Each channel realization was then simulated using 100 bits resulting in BER curves which were calculated as an average of the 1000 CIRs per SIR value and a total of 100,000 bits. Note that the narrowband interferer will fade differently with each CIR, causing both better and worse performance. However for simulation purposes this was not incorporated and the value of the interferer remained constant, keeping the SIR for a particular SNR constant across the CIRs.

When simulating the multipath channel it is also of interest to evaluate the performance of a Rake receiver. Therefore a Rake receiver's performance for 1, 5, and 10 fingers was examined. It has been shown that for a Rake receiver maximal ratio combining (MRC) is the optimal combining technique, in terms of maximimizing SNR, and is therefore the combining technique used. However MRC requires the use of channel estimation. This was accomplished by sending 20 pilot pulses through the channel. The channel estimates for each finger were determined as an average of the estimates of the pilot symbols. This estimation was performed in the presence of the narrowband interferer but not AWGN noise. Note that this does not represent a practical scenario however it is done to isolate the degradation caused by the narrowband interferer.

4.4 Simulation Results

One of the most important metrics for measuring a communication system's performance is the bit error rate (BER). BER results are presented here as a means for demonstrating the potential improvement in system performance when using a digital LMS or transversal filter narrowband interference cancellation circuit. The following system parameters remained constant for the ensuing analysis: f_c = 6 GHz, $f_{c,UWB}$ = 6 GHz, T_p = 1 ns, PRR = 1 MHz, and $F_{s,LMS}$ = 400 kHz (40 times the data rate).

4.4.1 AWGN Calibration

Before examining any interference scenarios, the performance is first provided for a purely AWGN channel in order to validate the proper operation of the simulation. Figure 4.14 provides these results for biphase (or polarity) modulation with the SNR = 3 dB and SNR = 6 dB. The plot displays the simulated values versus the theoretical values (The theoretical values are the same as BPSK). Similarly Figure 4.15 provides results for a binary PPM case which are also compared against the theoretical results (The PPM scheme used was orthogonal and binary so the performance was compared with BFSK). The correct operation of the UWB demodulation was verified. Note that in the figure the straight lines represent the theoretical values and the symbols represent the simulation results.

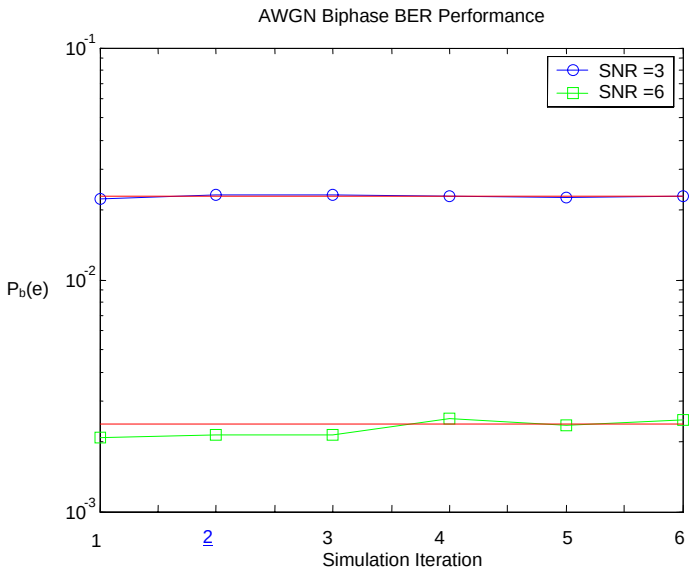

Figure 4.14 Biphase AWGN Performance

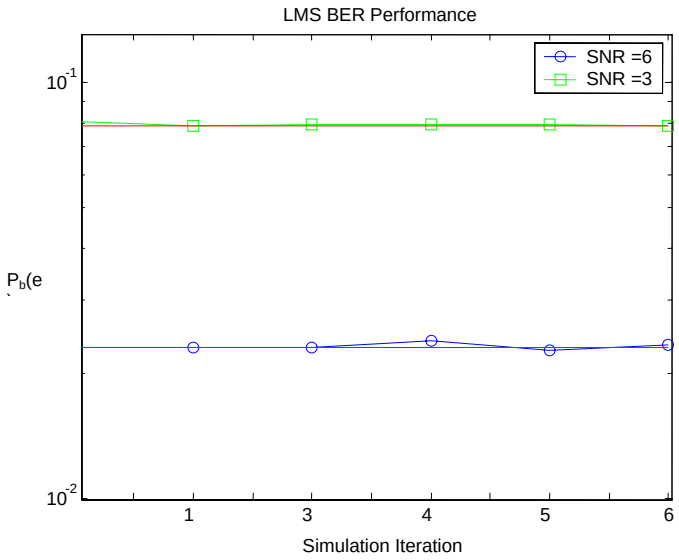

Figure 4.15 PPM AWGN Performance

4.4.2 Performance of Approach 1: The Single Tap LMS Canceller

First it is of interest to look at the performance of the LMS algorithm in an AWGN channel with narrowband interference. This can be thought of as a means of calibration and demonstrates the potential usefulness of the LMS algorithm. It also provides some insight into the performance of λ. As mentioned in section 4.3 there exists a λ which is optimum depending on the level of noise observed. However using the optimum λ would

require INR estimation and would considerably increase the complexity of the system. Therefore it is desirable to maintain a constant value of λ for which a small value of performance loss will be tolerated. Figure 4.16 provides a plot of the BER performance in an AWGN channel, in the presence of a tone interferer, and with a system SNR = 5 dB. The plot demonstrates that there is the potential for considerable performance improvement using the LMS algorithm (Note this was done using a tone interferer). The plot also demonstrates that the performance gain is dependent on the value of λ. If λ is too large the system is limited by the amount of noise. It is possible to reduce this value to achieve improved cancellation. However as λ is continually decreased eventually the performance at higher INR values (lower SIR values) will deteriorate. This is the result of adapting at a slower rate resulting in the algorithm mitigating less of the interference. On the other hand at lower INR values (higher SIR values) if the rate of change is too fast then additional noise will be added to the system. So examining the plot it can be seen that as λ is decreased from 0.15 to 0.01, the performance at -40 dB is degraded but the performance at the higher INR values is slightly improved. The value of λ should be chosen based on a tolerable amount of interference being added to the system.

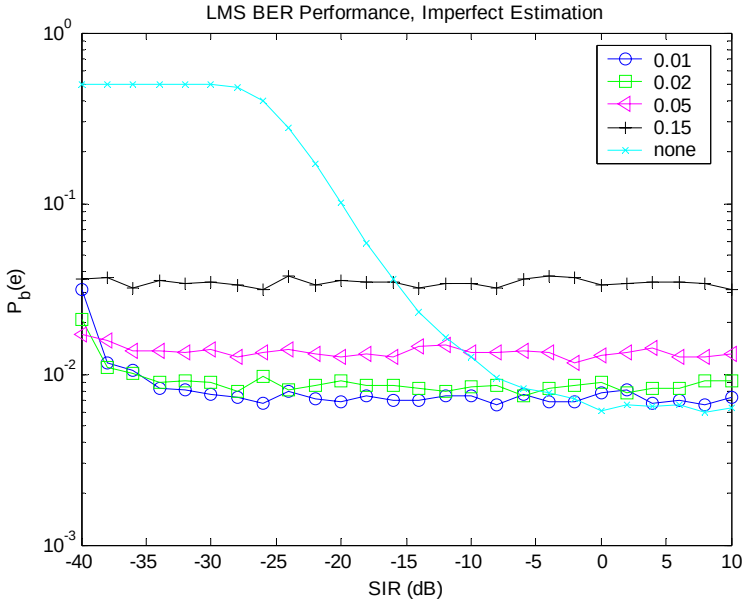

Figure 4.16 LMS Performance for a AWGN Channel, SNR = 5 dB

For communication systems, especially UWB, the performance in a multipath channel is of significant interest as it represents many practical situations. Here the performance is evaluated in terms of a Rake receiver using the CIRs described in Section 4.3. The first analysis assumes MRC with perfect channel estimation (i.e. complete knowledge of the channel). Figure 4.17a provides these results for 1, 5, and 10 fingers and for an SNR = 9 dB. BER results are given for both a tone and a modulated signal with equal λ values. Note the drastic difference in performance for a modulated signal and a tone interferer. The modulated case must adjust with every change in the symbol and is therefore unable to cancel the interference as well. However, these are for equal values of λ. Recall from Figure 4.13 that a modulated interferer requires a much larger value of λ than a tone

interferer. Figure 4.17b demonstrates this fact. However notice that as before with Figure 4.16, with a constant λ there is a trade off in performance at the higher and lower values of SIR.

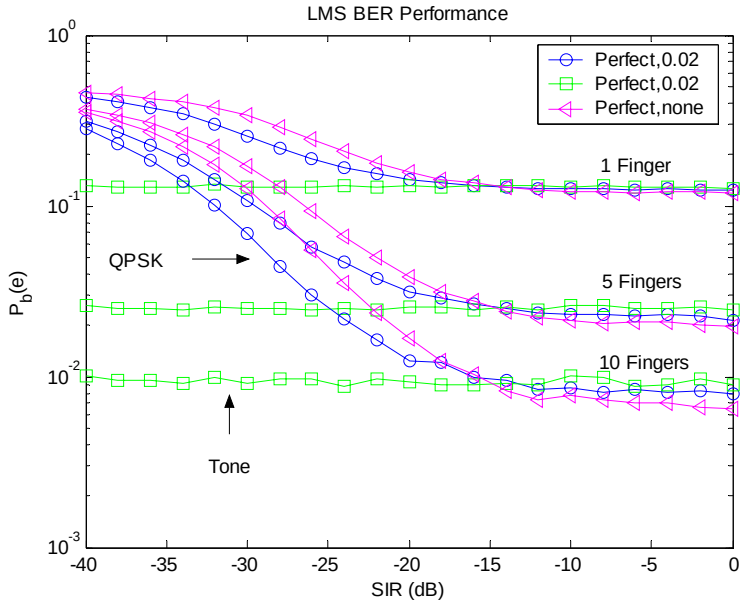

(a)

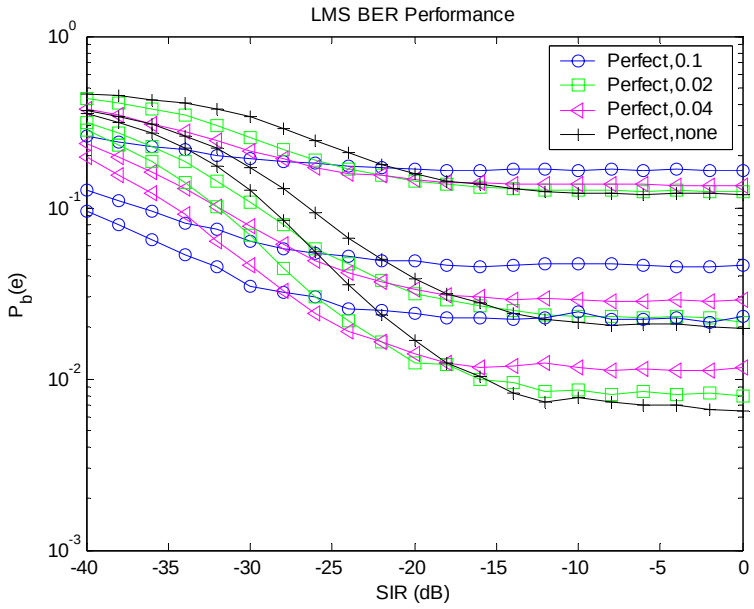

(b)

Figure 4.17 LMS Performance for a Multipath Channel, SNR = 9 dB (a) Tone vs. QPSK and (b) QPSK with Increasing λ

The previous plot assumed perfect channel estimation. Figure 4.18 demonstrates the impact of using imperfect channel estimation when a narrowband interferer is present

(without cancellation). At a BER of 0.03 there is a loss of over 10 dB in SIR when using 10 Rake fingers and imperfect channel estimation. Note that when using 1 Rake finger the impact is much less significant. This is likely due to the fact that the first path is the most dominant path. It is interesting to note that the imperfect estimation completely eliminates the Rake gain.

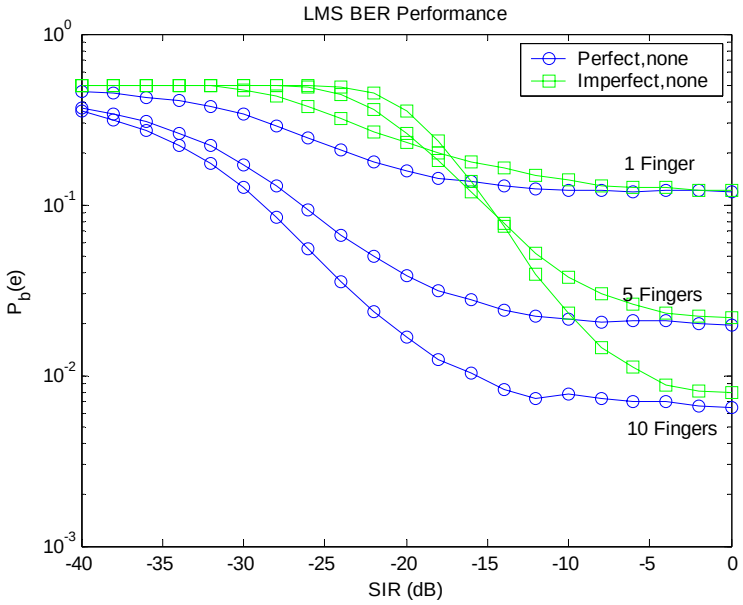

Figure 4.18 LMS Performance, Perfect vs. Imperfect Channel Estimation (no interference cancellation)

Figure 4.19 below shows the performance of imperfect channel estimation with interference cancellation for a tone and a modulated interferer. The plots show results for 1, 5, and 10 fingers. Notice that the trade off mentioned for Figure 4.16 is present when canceling the modulated interferer. Note that the required λ for sufficient cancellation in the case of the tone is much lower for the multipath channel than for the AWGN case. This is because the CIR and the pulse have been normalized to unit energy, so instead of all the energy being concentrated in one pulse (the AWGN case) it is spread over all the multipath components. However the amplitude of the interferer remains the same and therefore the multipath channel is more sensitive to the interference and must converge more slowly and more smoothly, requiring a smaller value of λ (Note this is just an effect of the simulation setup). Also, observe that the performance with a modulated interferer is extremely poor. This is due to the fact that the LMS algorithm converges too slowly over the 40 samples representing one modulated symbol.

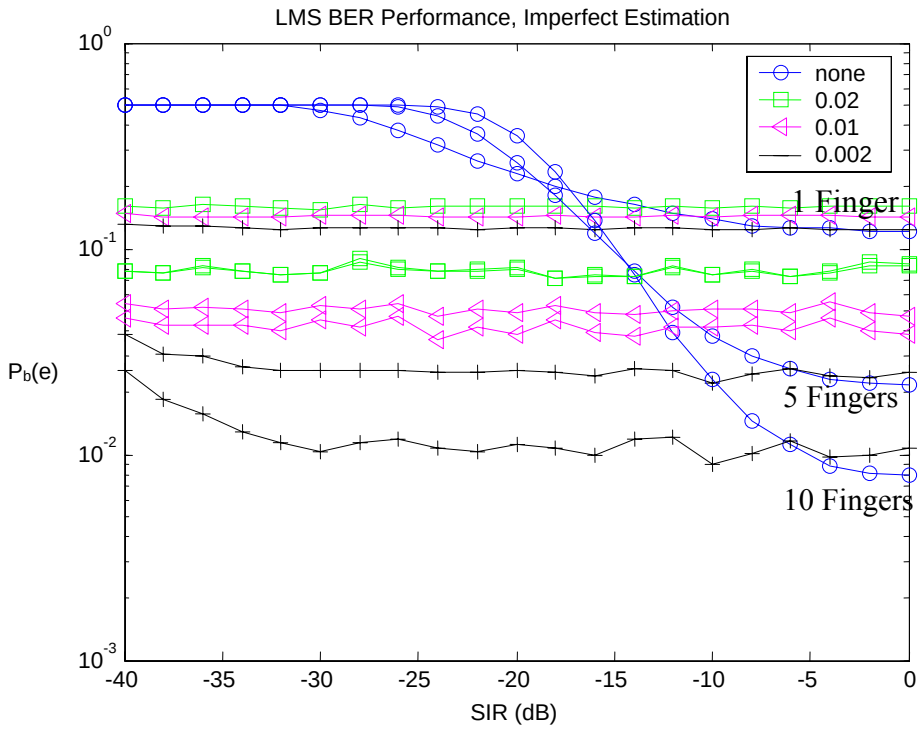

(a)

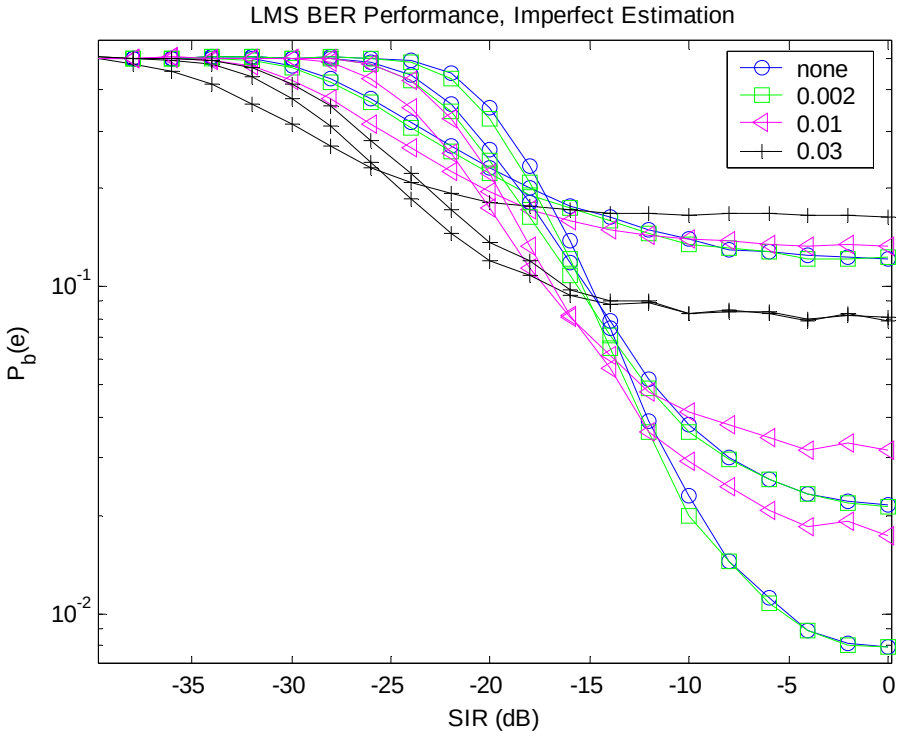

(b)

Figure 4.19 LMS Performance, Imperfect channel Estimation (a) Tone and (b) Modulated Interference for 1, 5, and 10 Rake Fingers

Note that the presented results for modulated interference were performed using a square pulse to create the modulated interference. In order to represent a practical scenario the simulation was rerun using a square root raised cosine pulse shape with roll-off factor of 0.35. However there was no change in performance for the LMS algorithm.

4.4.3 Performance of Approach 2: The Transversal Filter

As demonstrated in the Section 4.4.2 the LMS cancellation performs rather poorly in the presence of a modulated interferer, specifically QPSK. Therefore it is necessary to investigate techniques more suited to the abrupt phase changes associated with BPSK and QPSK modulation. Figure 4.20 plots the potential improvement when using a 30 tap two-sided transversal filter capable of predicting a square root raise cosine BPSK modulated interferer. Note however that the values of μ were not constant for the plot. The particular values used for this plot were $\mu = 0.001$ for $-55 > SIR > -30$ and $\mu = 0.01$ for $-30 > SIR > -5$. As SIR increases, meaning INR decreases, the filter's estimate of the signal becomes worse and actually adds a small bit of error to the system. However overall the method shows significant gains in performance.

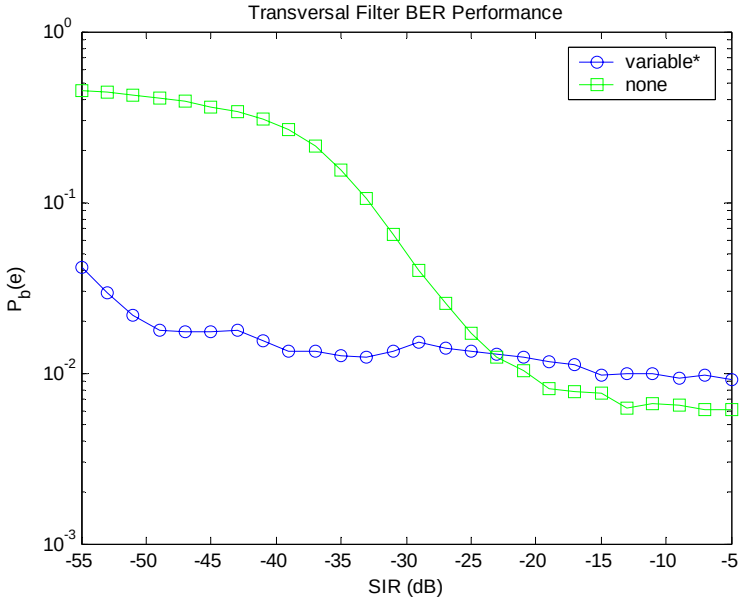

Figure 4.20 Transversal Filter NBIC BER Performance for SNR = 5 dB

Figure 4.21 plots the results for an SNR of 7 and 8 dB. The values of $\mu = 0.001$ for $-55 > SIR > -30$ and $\mu = 0.01$ for $-30 > SIR > -5$ were again used. Again significant performance gains are exhibited.

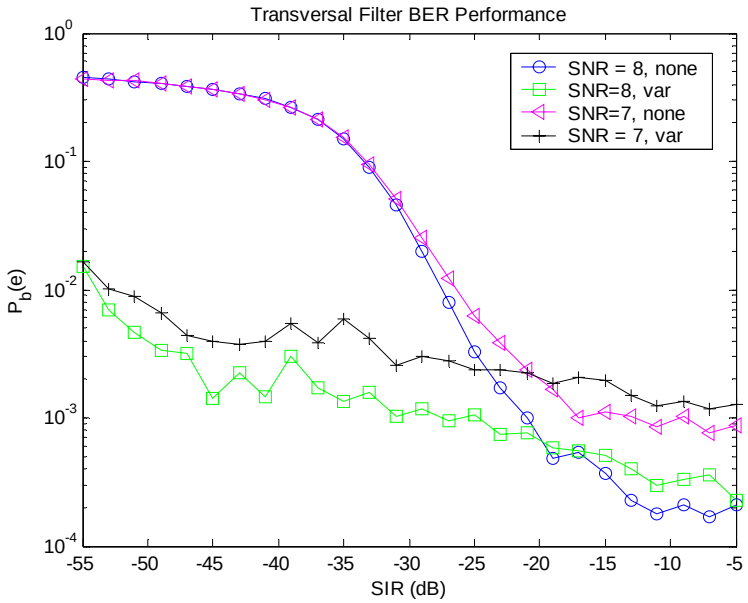

Figure 4.21 Transversal Filter NBIC BER Performance for SNR = 7 dB and 8 dB

It is also of interest to consider the mulitpath channel and Rake receiver performance. Consider the CIRs used in Section 4.4.2 and described in Section 4.3.4. Figure 4.22 illustrates the Rake receiver performance for the transversal filter (again using the previously mentioned values of μ) for SNR = 5 dB. Notice that there is a tremendous improvement when NBIC is used. Note that the NBIC results used Rake finger estimation in the digital backend. This demonstrates the transversal filter's ability to sufficiently cancel the interference so that estimation can be performed.

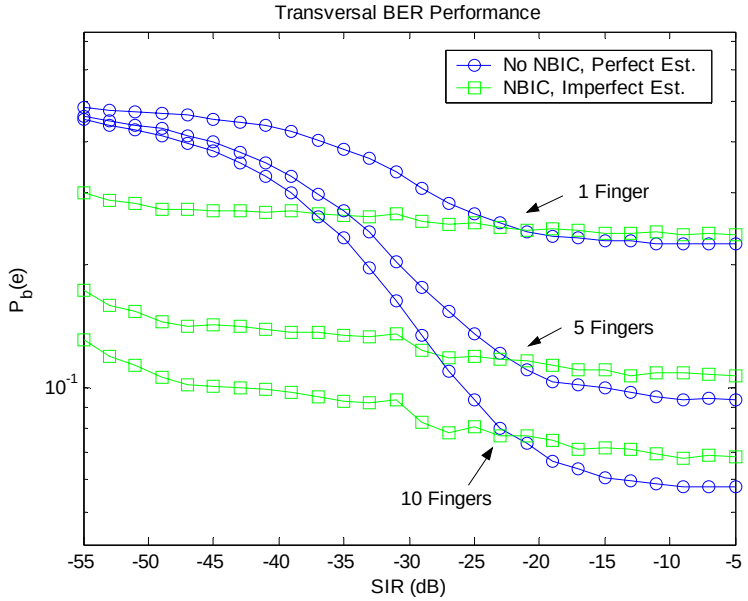

Figure 4.22 Transversal Filter Rake Receiver Performance SNR = 5 dB

4.4.3.1 INR Estimation

The previous results demonstrate the possible need for the ability to turn the cancellation on or off or to adapt the update parameter, μ, depending on the INR. This can be accomplished by estimating the INR of the signal using the signals autocorrelation matrix.

The autocorrelation matrix, R_{xx}, is estimated as follows.

$$R_{xx}[n] = (1-\gamma) R_{xx}[n-1] + \gamma (r'r) \tag{4.25}$$

where r is a vector of received samples and γ is the update parameter. It is expected that the diagonal elements will represent the signal and noise power and the off diagonal elements will represent only the signal power since the noise is uncorrelated from one sample to the next. The INR is then defined by $\frac{X_2}{X_1 - X_2}$ where $R_{xx} = \begin{bmatrix} X_1 & X_2 & \cdots & \cdots \\ \vdots & \ddots & & \\ \vdots & & \ddots & \\ \vdots & & & \ddots \end{bmatrix}$. Figure 4.23 below shows the autocorrelation of a square root raised cosine modulated waveform. The plot shows that the estimate of the INR is not the actual INR. However comparing the INR values it can be seen that the relative differences between the estimates and the actual INR values are the same. This technique could therefore be used to determine the need for cancellation. If the INR is low then it is not desirable to perform the cancellation. It is also possible that the INR estimate could be used to adjust the update parameter, γ.

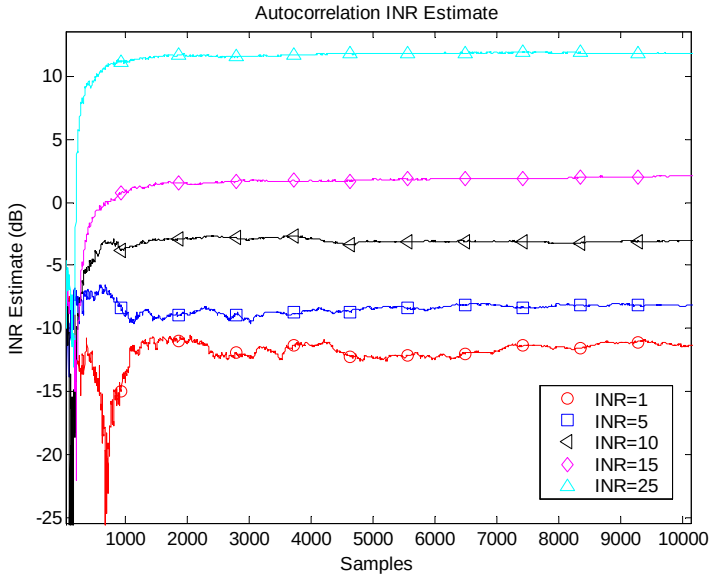

Figure 4.23 INR Estimation using the Signals Autocorrelation Matrix

4.4.3.2 Frequency Uncertainty

The effect of frequency uncertainty on the performance of the transversal filter cancellation also needs to be considered. The transversal filter is capable of tracking any residual frequency inserted by the narrowband interference down-conversion process. The residual frequency results from a non-exact center frequency estimate of the narrowband interferer. Note that high frequency components would not affect the baseband signal since they would be filtered after the down-conversion. However lower frequency components that can not be filtered are of interest. Consider the following example. Figure 4.24 shows the ability of the transversal filter to track the interferer in a very high SNR situation. The plot represents a 10 kHz baseband signal with a 5.6 kHz residual carrier frequency. The transversal filter is the same as above, with the number of taps equal to 30.

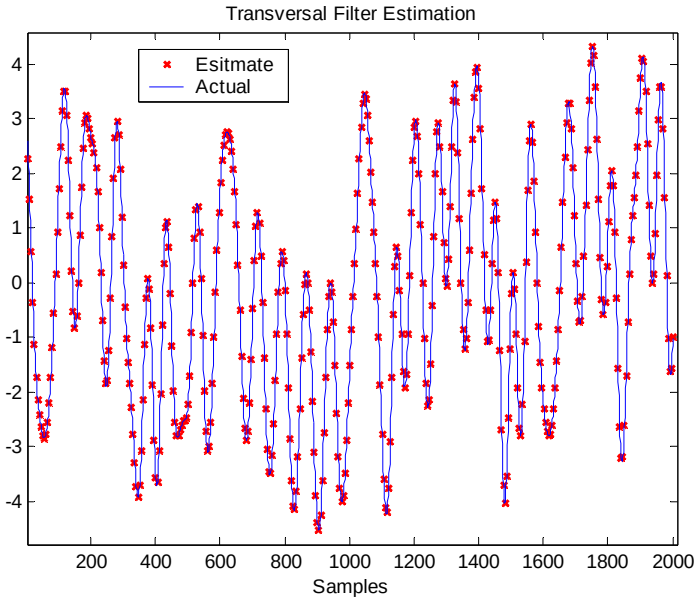

Figure 4.24 Effect of Frequency Uncertainty on Transversal Filter Estimation

Figure 4.25 demonstrates that the transversal filter has no problem estimating the baseband signal when a residual sinusoidal term is present. However since the signal estimate must be upconverted and subtracted from the actual narrowband signal the frequency uncertainty caused by the frequency estimation process will cause the subtraction to be suboptimal and the cancellation will be less effective.

4.5 Conclusions

In conclusion the LMS interference canceller doesn't seem to provide much promise. It performs satisfactorily for a tone interferer; however this doesn't represent a practical

situation. In a real world scenario the interferer will mostly likely be a modulated signal and in this case the cancellation circuit provides little benefit, if any at all. This is due in large part to the slow convergence of the LMS algorithm and consequently its inability to adequately track the narrowband interferer. This highlights the need for an algorithm with a much faster convergence. Therefore a two-sided transversal filter was examined. This implementation shows much promise for canceling narrowband interference. There is a drastic improvement over the LMS algorithm when a modulated interferer is present. Note that it may be worth while to investigate a block LMS or normalized LMS algorithm. The normalized LMS algorithm is helpful in situations where an adaptive update rate parameter is necessary.

Also note that frequency estimation could prove to be a challenging aspect of the circuit. Since there is a need to estimate the frequency of carriers in the gigahertz ranges this could require extremely high sampling rates. However it is possible to perform the estimation of the interferer's frequency using an intermediate frequency, therefore reducing the sampling rate requirements. Note also that there may be other means of estimating the narrowband center frequency, such as an analog transform, or the approximate carrier frequency may be known.

Chapter 5
Transform Domain Processing

5.1 Introduction

Real time transform domain processing is an analog signal processing technique capable of determining the spectral components of a signal as a function of time. The transformed signal can subsequently be processed. The processing is generally a type of filtering operation performed in the "frequency" domain. Typically transform domain processing is implemented using linear FM chirps (an in depth discussion of this will be given shortly). As mentioned in the interference cancellation background section in Chapter 3 this technique dates to the early days of spread spectrum when digital hardware did not yet provide a viable digital signal processing solution. Milstein authored several papers in the late 1970's and early 1980's which provide a nice introduction to the technique of transform domain processing [Mils77][Mils80]. A book by Kino is also an excellent source for the fundamentals of signal processing using linear FM chirps [Kino97]. The subsequent discussion provides an explanation of the real time Fourier transform processing technique.

The linear FM chirp is the basic component of real-time Fourier transform domain processing. A linear FM chirp is a sinusoidal signal whose frequency increases or decreases linearly with time. These signals are referred to as up-chirps or down-chirps respectively. A down-chirp can be represented mathematically as

$$c(t) = \cos\left(\omega_a t - \beta t^2\right) \tag{5.1a}$$

or in complex baseband notation

$$c(t) = \mathrm{Re}\left\{e^{j\left(\omega_a t - \beta t^2\right)}\right\} \tag{5.1b}$$

where ω_a is the initial frequency and β is the rate of change. The characteristics of the transform are directly impacted by the choice of ω_a and β. This is discussed in detail in section 5.2.

In general the real time Fourier transform of $x(t)$ is produced by first modulating the signal of interest by $c(t)$ given in equation (5.1). The modulation introduces the frequencies of $x(t)$ into the signal $c(t)$ in the form of sidebands on either side of the

chirp's original frequencies. For example, if $x(t)=\cos(\omega_c t)$ then the resulting signal formed by modulating $x(t)$ by the chirp $c(t)$ is

$$\cos(\omega_c t)\cos(\omega_a t-\beta t^2)=\frac{1}{2}\cos(\omega_a t-\beta t^2+\omega_c t)+\frac{1}{2}\cos(\omega_a t-\beta t^2-\omega_c t) \qquad (5.2)$$

This signal is simply two down-chirps with shifted initial frequencies. Using the modulated signal in equation (5.2) and a matched filter, a real time Fourier output can be obtained. The filter is matched to the original chirp given in equation (5.1). The matched filter is simply the time reverse of equation (5.1) and is therefore an up-chirp. Figure 5.1 represents the processing used to produce the real time Fourier output, $F(t)$, where the box in the figure is a filter with impulse response $\cos(\omega_a t+\beta t^2)$.

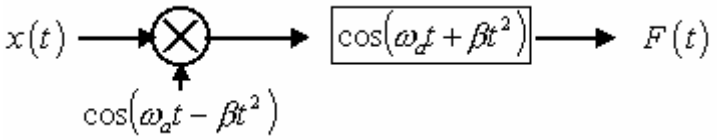

Figure 5.1 Real Time Fourier Transform Block Diagram

This process is now inspected more closely. Consider first the result of simply passing $c(t)$ through its matched filter. The output is the autocorrelation of $c(t)$, peaking at the instant when the chirp is completely contained within the filter. Now consider this in the context of producing a real time Fourier output. Examining equation (5.2) we see that because $x(t)$ is a tone the result of the modulation is two chirps with shifted initial frequencies (specifically $\omega_a+\omega_c$ and $\omega_a-\omega_c$). Accordingly this suggests that a pulse will result when these chirps align with their matched filter. Therefore a real time Fourier transform matched filter must contain the frequencies of these new chirps. The ability to represent a range of frequencies is therefore contingent on the filter length being longer than that of the modulating chirp. It is the ratio of the lengths of the modulating chirp and the filter which will determine the resolution of the system. (Filter length and the impact of the chosen chirps will be discussed in sections 5.2 and 5.3) The matched filter operation just described can be represented mathematically by the convolution operation. Let the signal to be transformed be $x(t)$. The output of the operation depicted in Figure 5.1 is given by [Mils80]

$$\begin{aligned}F(t)&=\int_0^T x(\tau)\cos(\omega_a\tau-\beta\tau^2)\cos(\omega_a(t-\tau)+\beta(t-\tau)^2)d\tau\\&=\frac{1}{2}\cos(\omega_a t+\beta t^2)\int_0^T x(\tau)\cos(2\beta t\tau)d\tau+\frac{1}{2}\sin(\omega_a t+\beta t^2)\int_0^T x(\tau)\sin(2\beta t\tau)d\tau \qquad (5.3)\\&\quad+\frac{1}{2}\int_0^T x(\tau)\cos(2\omega_a\tau-2\beta\tau^2+2\beta t\tau-\omega_a t-\beta t^2)d\tau\end{aligned}$$

which is approximately

$$F(t) \approx \frac{1}{2}F_R(2\beta t)\cos\left(\omega_a t+\beta t^2\right)-\frac{1}{2}F_I(2\beta t)\sin\left(\omega_a t+\beta t^2\right) \tag{5.4}$$

where $F_R(\cdot)$ and $F_I(\cdot)$ represent the real and imaginary parts of the Fourier transform of $f(t)$.

Notice that the Fourier transform is represented by the first two terms in equation (5.3). This is expressed in equation (5.4). The third term in equation (5.3) can be ignored in practical systems since it can be effectively filtered out. It is also possible to configure a system where the third term is canceled [Mils80]. However for the purposes of the system discussed here the third term is not important as we are only interested in the magnitude of the spectral components as they relate to one another and not the absolute transform.

Interference can be mitigated by applying an appropriate filtering operation to a real time Fourier signal. This is accomplished by either limiting or notching the real time Fourier output whenever it exceeds a specified threshold. The threshold is represented by $H(2\beta t)$ in Figure 5.2 below.

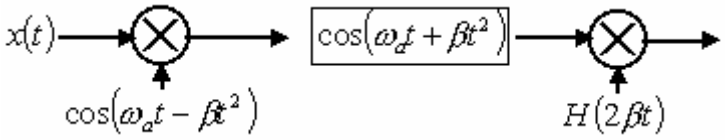

Figure 5.2 Block Diagram of Interference Cancellation

Following the cancellation of the interference, the signal is inverse transformed using the time reverse of the matched filter (in this case a down-chirp). The output is then modulated again by the original down-chirp to "down-convert" the signal. Figure 5.3 gives the block diagram for the complete interference canceller using a real time Fourier transform. The output of this circuit is passed to the UWB receiver for synchronization and detection.

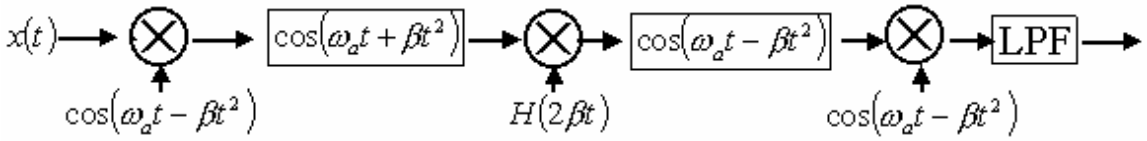

Figure 5.3 Real Time Fourier Transform Interference Cancellation Receiver

Note the lowpass filter required after "down-conversion". This is necessary to remove the double frequency term introduced by the "down-conversion". These frequencies can be removed using an appropriate lowpass filter. Consider modulating equation (5.2), again by the down-chirp. This results in equation (5.5). (Note that this analysis does not represent all of Figure 5.3. The transform and inverse transform do not need to be

represented in the equation. It is only intended to validate the need for the low pass filter).

$$\cos(\omega_c t)\cos^2(\omega_a t - \beta t) = \frac{1}{2}\cos(\omega_c t) + \frac{1}{4}\cos\left((\omega_c - 2\omega_a)t + 2\beta t^2\right) + \frac{1}{4}\cos\left((\omega_c + 2\omega_a)t - 2\beta t^2\right) \tag{5.5}$$

Examining equation (5.5) the second two terms are chirps that have shifted to higher frequencies as a result of the modulation. Precisely, the chirps have been shifted to twice the initial frequency of the original chirp and also by the frequency of $x(t)$, resulting in down-chirps with twice the rate of change of the original down-chirp. These terms can be effectively removed using a proper lowpass filter.

5.2 Chirp Parameters

As mentioned in the previous section, the chirp filter and the modulating chirp are both finite in length. The parameters of these signals must be correctly chosen in order to properly represent the frequencies of interest and correctly perform the inverse transform. First the parameters are briefly introduced. The linear FM chirp is defined by its initial frequency, ω_a, and its linear rate of change, β. This is accomplished by providing a starting frequency f_0, an ending frequency f_1, and a time duration for the chirp, T_c, such that

$$\beta = \frac{|f_0 - f_1|}{T_c}, \quad \omega_a = f_0 \tag{5.6}$$

The bandwidth of the chirp is then given as $B = |f_0 - f_1|$. Often a center frequency, $f_{c,chirp}$, is also specified which is defined as $f_{c,chirp} = \frac{f_0 + f_1}{2}$. The time-bandwidth product of the chirp, given as $TB = B \cdot T_c$, is a metric often used to characterize these devices. In general, larger time bandwidth products will provide better frequency resolution for the system. However just looking at the time bandwidth product does not give information about the actual frequencies, bandwidths, and lengths of the chosen chirps, which are of vital importance. It is more important to choose the chirp filters based on these values.

As previously mentioned, the spectral content of the output is directly related to the frequencies contained in the chirp matched filter. As shown in equation (5.2), modulating by a chirp results in both lower and upper sidebands being introduced around the initial chirp. These sidebands can be thought of as representing positive and negative frequencies of the signal. Negative frequency of course does not exist but it is often times used in Fourier analysis. Figure 5.4 provides an illustration of this where f = 0

represents the position of the original chirp and f_c is the frequency of the modulated signal.

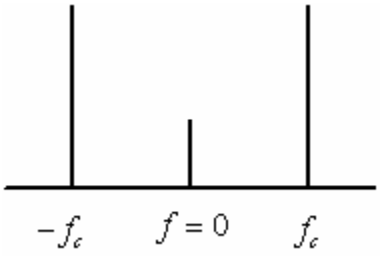

Figure 5.4 Representation of Sidebands

It is unnecessary to represent both sidebands in the Fourier output because they represent the same frequency. Recall that for a given modulating chirp signal the resulting Fourier output is completely controlled by the definition of the matched filter (Note the matched filter will be discussed in relation to the original down-chirp but bear in mind that it is really just the time reversed version of the down-chirp discussed). It was mentioned in section 5.1 that the region for which the real time Fourier transform is valid is directly related to the length of the matched filter. This is because a valid output is only obtained when the modulated signal is fully contained within the matched filter. Consider a filter whose initial frequency is ω_a, rate of change is β and length is T_c. If the matched filter has length T_s then the range of frequencies that can be represented is given as $\left[0, \beta\left(T_s - T_c\right)\right]$, which is simply the bandwidth of the filter minus the bandwidth of the modulating chirp. This represents a situation where the matched filter includes the frequencies of the modulating chirp. But, as can be envisioned, this range can be shifted so that only a specific range of frequencies is represented. For instance it may be of interest to only represent the operating frequencies specified by the FCC for UWB operation (3.1 – 10.6 GHz). In this case the initial frequency of the matched filter would be defined as $\omega_a - 3.1\,\text{GHz}$ which would result in the frequency range of $\left[3.1\text{ GHz},\ 3.1\text{ GHz} + \beta\left(T_s - T_c\right)\right]$ being observed. The length of T_s can be adjusted accordingly to control the upper portion of this frequency range.

It is imperative that the chirp filter has the proper bandwidth and operating frequency range in order to not only observe the spectral components but also to properly perform the inverse transform. In general, for the case of the down-chirp, being able to do so is dependent on the lowest frequency component of the modulating chirp being greater than the largest spectral component of the signal of interest. This is because the lower sideband of the modulated signal is used for the processing. For instance consider Figure 5.5 which provides the real time Fourier output and its corresponding inverse transform. These results were produced with a matched filter bandwidth of 12 GHz and a modulating chirp with a bandwidth of 4 GHz. The signal was a 1 ns RF pulse with f_{cUWB} = 6 GHz. The signal is inverse transformed without distortion and notice that this is possible with a small portion of the spectrum not being represented. Figure 5.6 shows a

similar analysis for a filter bandwidth of 8 GHz instead of 12 GHz. In this example the frequency range for which the signal needs to be observed is not chosen properly. The modulating chirp is 4 GHz, the matched filter is 8 GHz, and therefore the real time Fourier output can represent a bandwidth of 4 GHz. Because of the matched filter starting frequencies the output represents a range of 0 to 4 GHz but the UWB signal has a center frequency of 6 GHz. The real time Fourier output therefore cannot represent the majority of the spectrum. This causes distortion in the inverse transform of the pulse. This illustrates the need to choose the frequencies of the match filter such that all the frequencies of interest are represented. This will allow interference anywhere in the band to be mitigated and improve the result of the inverse transform.

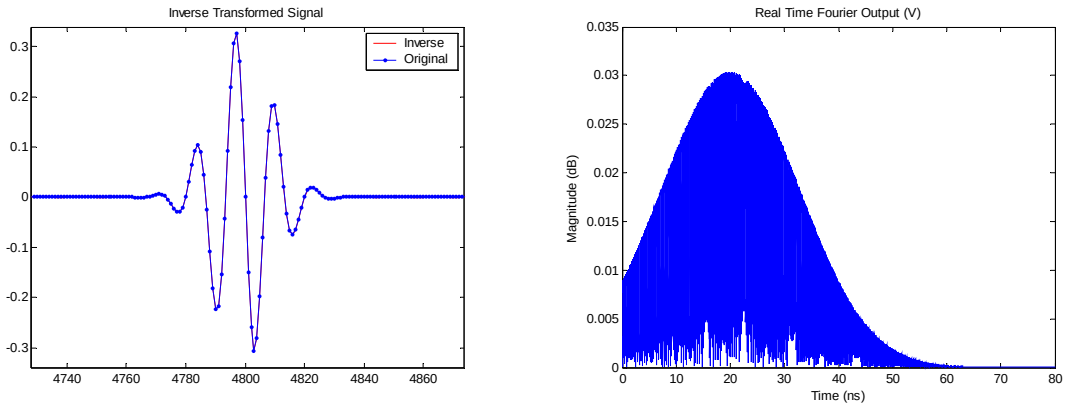

(a) (b)

Figure 5.5 (a) Example RF UWB Pulse and Inverse Transform and (b) the Corresponding Transform Domain Output

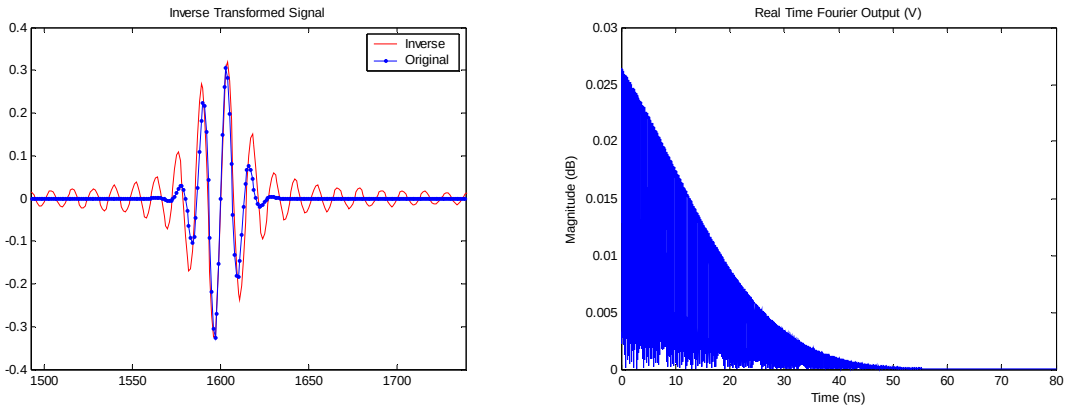

(a) (b)

Figure 5.6 (a) Example RF UWB Pulse and Inverse Transform with Improper Parameters and (b) the Corresponding Transform Domain Output

5.3 Finite Length Effects

As mentioned in section 5.1 the length of the signal of interest compared to the matched filter has an effect on the representation of frequencies and correct computation of the inverse transform. It also directly affects the shape of the output spectrum, especially as it relates to narrowband interference.

Consider the case where only the linear FM chirp is passed through its matched filter where $u(t) = e^{j(\omega_0 t - \beta t^2)}$ is an up-chirp and $h(t) = e^{j(\omega_0 t + \beta t^2)}$ is the matched filter, down-chirp. Note that UWB is not generally considered in the context of complex baseband, however it is used here to ease analysis. In the end only the magnitude of the result is of interest. The output of the matched filter is then the convolution of $u(t)$ and $h(t)$ and is given by [Kino87]

$$y(t) = \int_{-\infty}^{\infty} u(\tau) h(t-\tau) d\tau = \int_{-\infty}^{\infty} e^{j(\omega_0 \tau - \beta \tau^2)} e^{j(\omega_0 (t-\tau) + \beta (t-\tau)^2)} d\tau \tag{5.7}$$

However since the input chirp is time limited with length T the integral becomes

$$y(t) = \int_{-T/2}^{T/2} e^{j(\omega_0 \tau - \beta \tau^2)} e^{j(\omega_0 (t-\tau) + \beta (t-\tau)^2)} d\tau \tag{5.8}$$

This yields $y(t) = e^{j(\omega_0 \tau + \beta \tau^2)} \int_{-T/2}^{T/2} e^{-j2\beta t \tau} d\tau$. After integration the result becomes

$$y(t) = T \frac{\sin(\beta T t)}{\beta T t} e^{j(\omega_0 \tau - \beta \tau^2)} \tag{5.9}$$

Note that the result contains a term in the form of $\sin(x)/x$ which is the sinc function. This term contributes side lobes in the real-time Fourier output. The width of the main lobe is determined by the bandwidth of the modulating chirp signal. Just for reference the 4 dB and 10 dB lobe widths will be discussed. Based on the definition of the sinc function the 4 dB and 10 dB points occur at approximately π/2 and 0.74π respectively or when $2\beta T t = \pi$ and $2\beta T t = 3\pi/2$. The times associated with these points are therefore $t = \pi/2\beta T$ and $t = (3\pi/2)/2\beta T$. Accordingly the pulse widths are double this and given by

$$\tau_p = 2\left(\frac{\pi}{2\beta T}\right), \quad \tau_p = 2\left(\frac{3\pi/2}{2\beta T}\right) \tag{5.10}$$

In terms of spectral analysis it can be seen that the side lobes can make it problematic to distinguish between individual frequency components. For the purposes of interference

cancellation it is not of interest to actually distinguish between spectral components but rather just to cancel or mitigate them. The mitigation is performed by limiting the power of the narrowband interferer according to a threshold. The threshold is defined relative to the UWB's signal power, as discussed in section 5.1. However the side lobes will adversely affect this process as they contribute energy over the entire band of the UWB signal and are difficult to remove. Note that notching the interference is not an option as it would remove a large portion of the UWB signal energy. Consider the output shown in Figure 5.7. This portrays an example real time Fourier transform of a UWB RF pulse with $f_{c,UWB}$ = 4 GHz. The chirp filter parameters were f_0 = 20 GHz, f_1 = 8 GHz, and T_s = 120 ns and the modulating chirp parameters were f_0 = 20 GHz, f_1 = 16 GHz, T_c = 40 ns. Figure 5.8 shows the output for a 4 GHz tone interferer with an SIR = -40 dB at a PRR of 1 MHz, as well as a magnified plot which displays the side lobes. Observe that the side lobes have magnitudes which are greater than the largest magnitude of the UWB spectrum. Figure 5.9 shows a magnified portion of the tail of the tone's spectrum from Figure 5.8 along with the corresponding portion of the UWB spectrum. Even in these portions of the spectrum, the magnitude of the tone's contribution is greater than the UWB signal's.

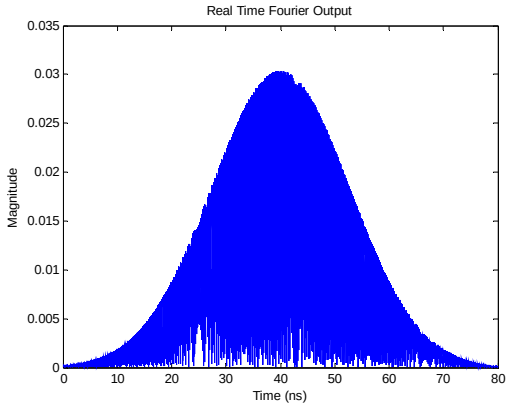

Figure 5.7 Real Time Fourier Output, UWB RF Pulse f_c = 4 GHz

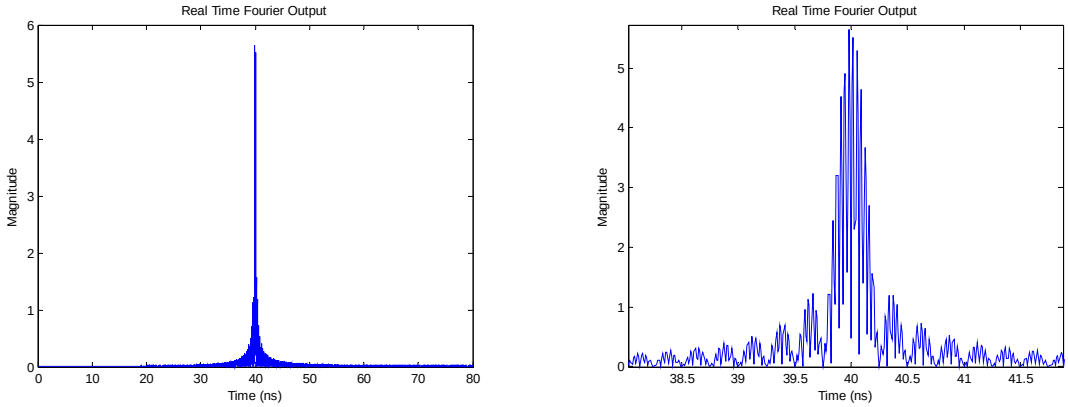

Figure 5.8 Tone (f_c = 4 GHz), (a) Real Time Fourier Output and (b) Magnified to Show Side Lobes

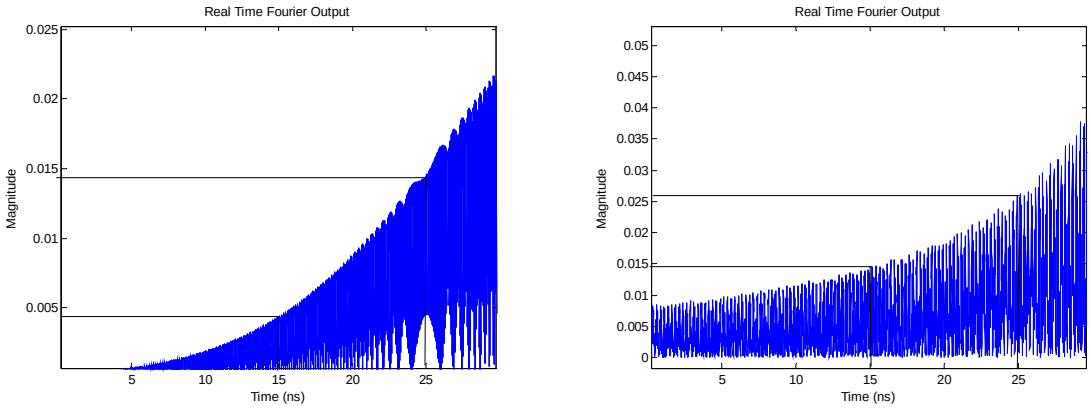

(a) (b)

Figure 5.9 (a) Magnified UWB Spectrum and (b) Magnified Tone Spectrum

When trying to mitigate the interference it is not possible to remove all the energy contributed by the side lobes. Accordingly this results in residual narrowband interference after cancellation. The remaining interference is concentrated in certain areas. Consider again the plots shown in Figure 5.8. The frequency output, which is shown as a function of time, actually corresponds directly to portions of the signal in the time domain. For instance if the main lobe of the spectral output was excised this would leave portions of the narrowband signal at the ends of the signals. This is shown in Figure 5.10 where the main lobe and several of the side lobes on either side have been excised. It does not always make sense to notch the interference in a practical scenario since it could result in the majority of the UWB signal energy being removed, however it is done here purely to demonstrate the contribution of the side lobes. Since the interference suppression is a front end process and intended to be used before the UWB receiver the residual interference could causes problems with acquisition and synchronization eventually leading to an increased bit error rate. However, if we are using a system that estimates pulse shape the distortion to the UWB pulse may be tolerable.

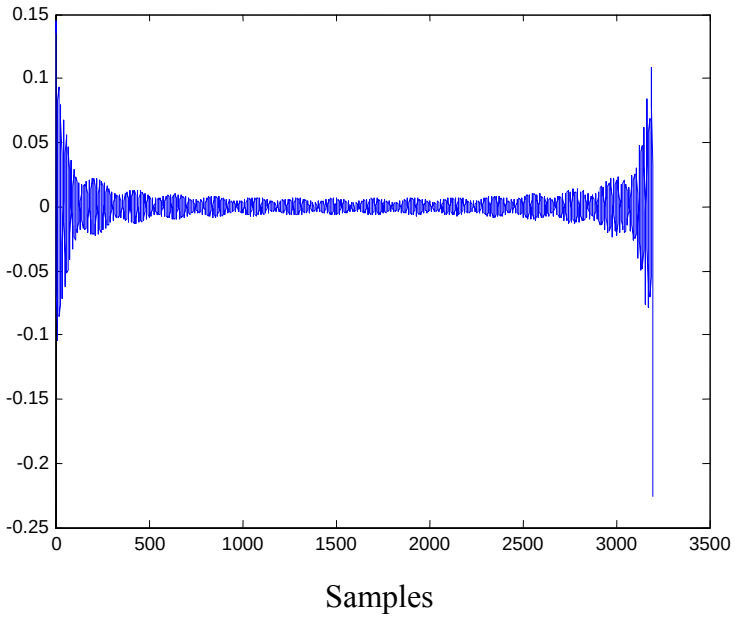

Figure 5.10 Time Domain Residual Narrowband Signal After Main Lobe Excision

It is possible to reduce the side lobes by windowing the transformed signal. This windowing is analogous to windowing utilized in FIR filters. The effect of using these functions is a reduction in the amplitude of the side lobes and a widening of the main lobe. This trade off is present with all windowing functions. Therefore a window must be chosen that provides a tolerable main lobe width and at the same times has acceptable side lobe levels. Table 5.1 gives some common windowing functions with their corresponding main lobe widths and side lobe levels. BT is the bandwidth of the modulating chirp multiplied by the main lobe width, in time. For example a chirp with a bandwidth B, and using a rectangular window, would have a main lobe width at 3 dB of T = 0.89(1/B).

Table 5.1 Window Types

Weighting Function	Peak side lobe level (dB)	BT (3dB)	BT (6dB)	Far sidelobe falloff rate
Rectangular	-13	0.89	1.21	1/t
Bartlett	-27	1.28	1.78	$1/t^2$
Hanning	-32	1.44	2	$1/t^3$
Hamming	-43	1.3	1.81	1/t
Finite Gaussian	-42	1.33	1.86	1/t
Blackman	-58	1.68	2.35	$1/t^3$

Figure 5.11 provides a comparison of the side lobes for a rectangular window and a Hanning window using the same chirp parameters specified for Figures 5.8 – 5.10. The 6 dB bandwidths for these windows are 30.25 MHz and 50 MHz respectively (Note that

these values are specific to the chirps used). Relative to the UWB spectrum, the increase in the main lobe width is negligible. However the reduction in the side lobe levels is significant and can lead to considerable improvement in the cancellation performance. Figure 5.12 provides an example of this. The cancellation was performed by limiting the real time Fourier output according to the output of the UWB signal in the presence of an interferer with an SIR = -50 dB. Reducing the side lobes allows the UWB pulse to be recovered more accurately while still canceling the interference.

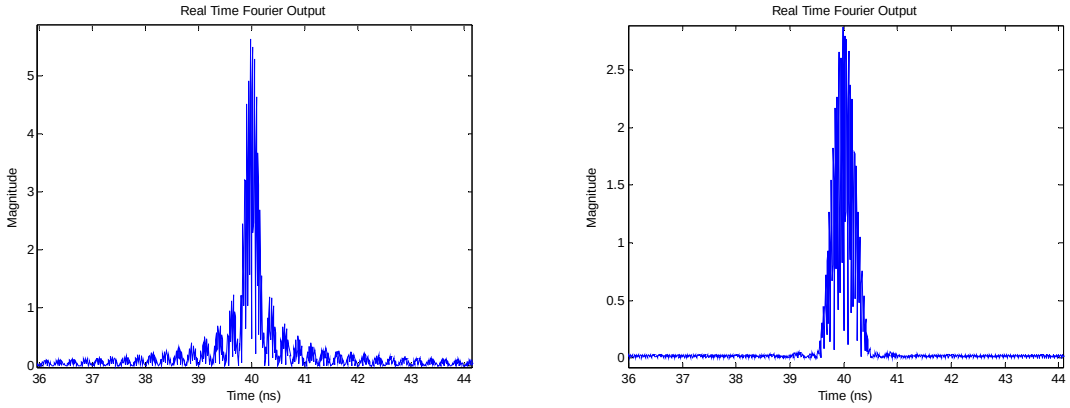

(a) (b)

Figure 5.11 Real Time Fourier Output (a) Rectangular and (b) Hanning Window

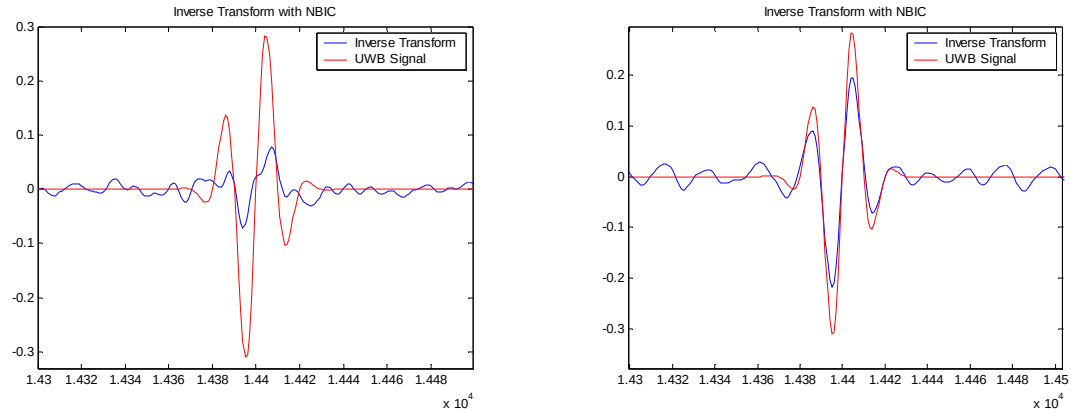

(a) (b)

Figure 5.12 Recovery of UWB Pulse after Cancellation (a) Rectangular and (b) Hanning Window

Note that using windowing does improve performance but it also presents other challenges. Applying windowing results in a scaling and shaping of the time domain signal being transformed. The effect is that the beginning and end of the transformed signal are significantly attenuated in the time domain. Proper operation would require the UWB signal to be centered in the window. Otherwise the signal would be attenuated and the error performance would increase. This would also be problematic if it was desired to

use a rake receiver as multipath components would be rendered less significant near the edges of the window. Figure 5.13 shows an example of the effect of the Hanning window used for the analysis in Figure 5.12. The plot represents the result of the inverse transformation. This demonstrates the need for the UWB signal to be positioned in the center of the transform window.

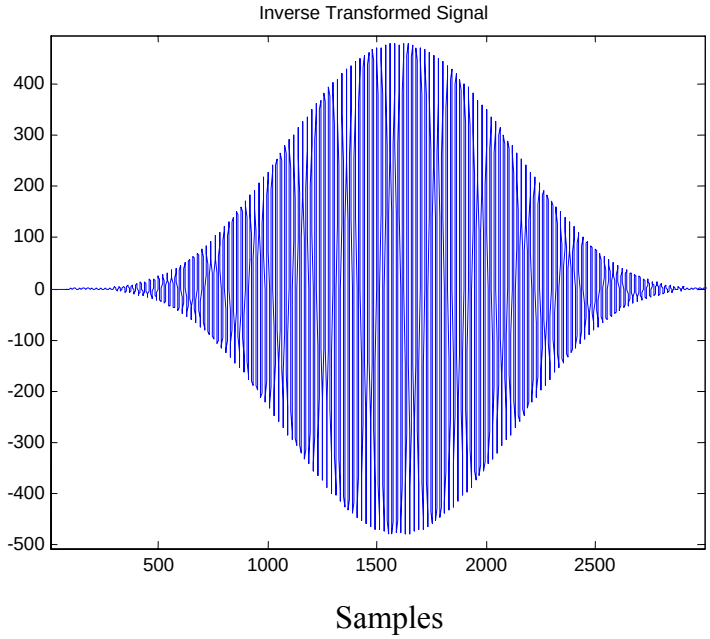

Figure 5.13 Effect of Windowing in the Time Domain

One last quick note concerning the main lobe of the Fourier output. Referring to equation (5.10) it can be seen that the width of the main lobe is reduced if the bandwidth of the modulating chirp is increased. It is possible to increase the chirp bandwidth in two ways, by either increasing β or increasing the length, T_c. Both of these result in the width of the main lobe being reduced in terms of time, however the interpretation for each is different. If β is increased then both the bandwidth of the filter and the modulating chirp are increased. Therefore even though this reduces the width of the main lobe, the bandwidth which it represents remains the same. On the other hand, increasing the length of the chirp results in both a decrease in the width of the lobe and a decrease in the spectrum it covers, which is desirable. So by increasing the length of the modulating chirp it may be possible to improve performance. However doing so may require the filter to be lengthened as well since it will reduce the frequency range of the output.

5.4 Applicability of SAW Filters.

Several industry professionals have been contacted and it doesn't appear that there are any readily available commercial SAW chirp filters. Previous uses for these devices, such as radar compression, can now use digital processing techniques, and as stated by one of the contacts, the chirp Fourier transform industry is "virtually dead". This

particular contact says, "(they) haven't developed a new pulse compression system in the last 15 years". So for now acquiring these devices may be difficult and expensive.

Also the limits on these devices do not meet the requirements for a UWB system. For example, the UWB signals would be occupying the 3.1 – 10.6 GHz portion of the spectrum, but the highest center frequency mentioned is 1.5 GHz. These center frequencies and likely bandwidths would not be suitable UWB. The type of materials and construction limit the achievable center frequencies and bandwidths.

5.5 Simulation Assumptions

The following provides a description of the assumptions made when simulating the BER performance using the transform domain processing technique. The determination of SIR is the same as the description provided in Chapter 4 however the definitions are reproduced here for completeness.

All BER simulations performed relate the error performance as a function of signal to interference ratio (SIR) for a given signal to noise ratio (SNR). The SNR for the system is defined as

$$SNR = \frac{E_b}{N_0} \tag{5.11}$$

where E_b is the energy per bit of the UWB system and N_0 is the noise power. Note that it was assumed that each bit was represented by a single pulse and therefore the energy per bit is given by the energy in one pulse. The energy per pulse is always normalized to one. SIR then is defined as the ratio of the UWB signal energy to the narrowband interferer energy. For these simulations narrowband signal energy was defined as a function of the pulse repetition rate (PRR) and the spreading gain of the UWB system. PRR refers to the number of pulses transmitted per second and spreading gain refers the number of pulses representing a single bit. However as previously mentioned the spreading gain is simply one and therefore is not a factor in the calculation of SIR (The effects of spreading gain will be further discussed with the results). Therefore SIR is simply a function of PRR and is defined as

$$SIR = \frac{E_b}{E_t} \tag{5.12}$$

where E_t is the energy in the tone. E_t is defined by

$$E_t = \sum_{n=0}^{N-1} \sin^2\left(2\pi \frac{n}{F_s}\right) \quad \text{where } N = \frac{F_s}{PRR} \tag{5.13}$$

and F_s is the sampling frequency. The energy in the tone is therefore simply the sum of its squared samples over the period between UWB pulses (i.e. 1/PRR).

The simulations performed the interference cancellation using transform domain processing to limit the real time Fourier output, thereby reducing the effects of the interference. The simulation was calibrated such that the process of transforming and inverse transforming did not artificially add or remove energy. This was accomplished by passing a UWB pulse through the transform domain operation and forcing the pulse amplitudes to be equal at the input and output of the operation. Note that this was done with a UWB pulse alone. Any loss incurred from adding the UWB signal and performing cancellation was not modified. Once calibrated, the cancellation was performed by adding narrowband interference to a series of 1000 UWB RF pulses, with each pulse being centered in the middle of the modulating chirp window. Using the transform domain processing technique interference cancellation was performed by hard limiting the interference. This results in an output which could be demodulated. AWGN noise was then added to this resulting signal and demodulation was performed in a series of iterations. If it was desired to simulate 100,000 bits then 100 iterations were performed on the 1000 UWB pulses.

5.6 Simulation Results

This section presents a BER performance analysis in order to evaluate the usefulness of interference cancellation using transform domain processing. Because of the challenges discussed in section 5.3 these results are preliminary and are to serve as a proof of concept. First however Figure 5.14 provides plots which serve as a form of calibration by demonstrating the simulation properly performs demodulation on the UWB signal. This is provided for both biphase and PPM modulation. Note this does not include interference mitigation or transform domain processing. This was simply done to verify that proper operation of the demodulation.

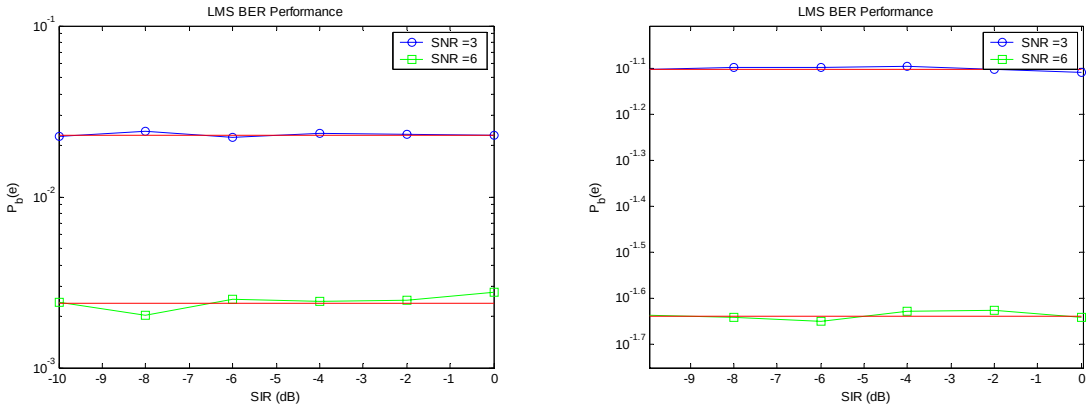

(a) (b)

Figure 5.14 Simulated and Theoretical (a) Biphase AWGN Performance and (b) PPM AWGN Performance

Figure 5.15 provides plots which demonstrate the performance of interference cancellation. These simulations were conducted using, f_0 = 20 GHz, f_1 = 8 GHz, and T_s = 120 ns for the chirp filter and f_0 = 20 GHz, f_1 = 16 GHz, T_c = 40 ns for the modulating chirp. The signal was a UWB RF pulse with $f_{c,UWB}$ = 6 GHz in the presence of a narrowband interferer with a f_c = 6 GHz. The figures are for SNR = 3 dB and 6 dB respectively. Notice that when using the Hanning window the performance is improved considerably. Figure 5.15a also compares the effects of using a rectangular window versus a Hanning window. As expected the rectangular window performs considerably worse.

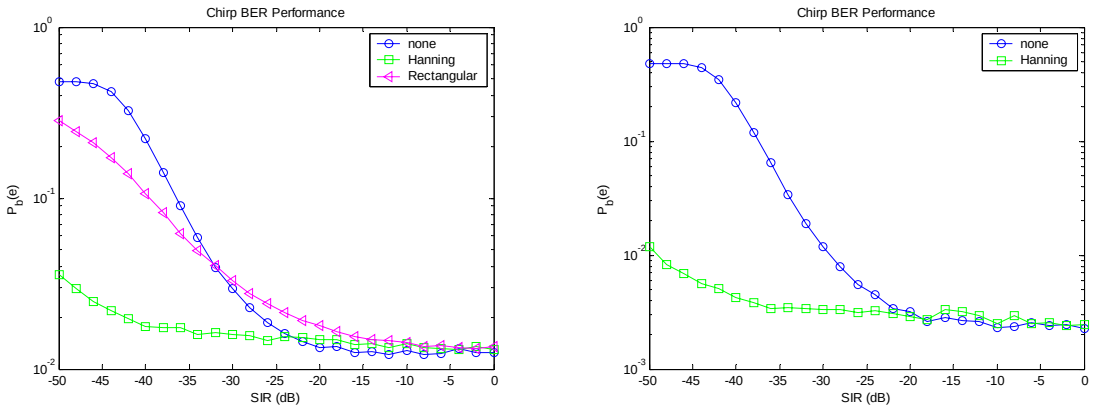

(a) (b)

Figure 5.15 BER Performance with interference cancellation (a) SNR = 3 dB and (b) SNR = 6 dB

Recall that with the LMS cancellation circuit the presence of a tone interferer versus a modulated interferer had a large impact on the performance of the interference cancellation. However for the case of transform domain processing the window over which the real time Fourier transform is being performed is considerably smaller than symbol duration of any modulated interferer. Therefore the bandwidth of the narrowband signal will not be visible in the spectrum output and performance will not be affected. Additionally, we consider magnitude-based cancellation which would not be affected by modulation. Figure 5.16 illustrates that the cancellation performs equally well in the presence of a BPSK signal when compared to a tone.

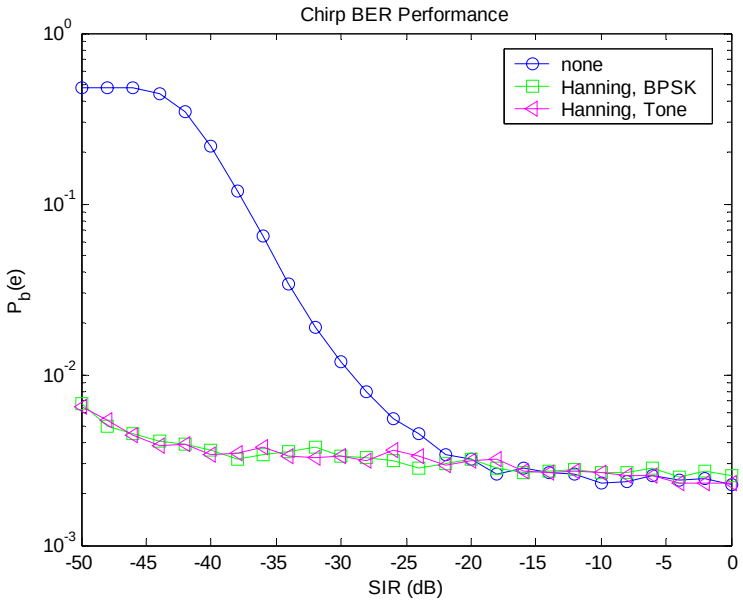

Figure 5.16 BER Performance with Interference Cancellation for a Tone and BPSK Signal

A simple simulation was also conducted to illustrate previous issues concerning multipath. Consider the multipath signal shown in Figure 5.17. The signal was created using 3 taps at 0, 10, and 16 ns, with amplitudes of 0.74278, -0.37139, and 0.55709 respectively. This CIR has unit energy and the UWB pulses had center frequencies of 6 GHz and a pulse width of 1 ns.

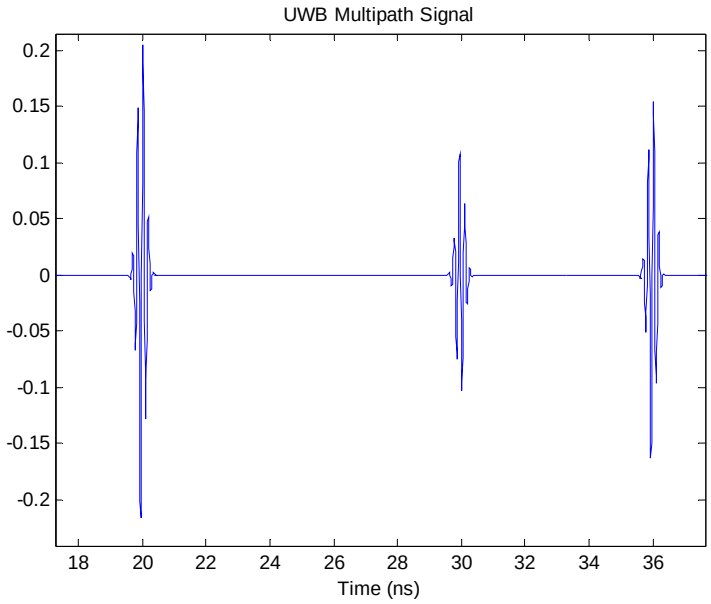

Figure 5.17 UWB Multipath Signal

Figure 5.18 shows the effects of transform domain processing when using a Hanning window (The same effect was demonstrated in Figure 5.13). Note that this result assumes that the first path was aligned in the center of the chirp modulating signal, (i.e. the first path's amplitude was not affected).

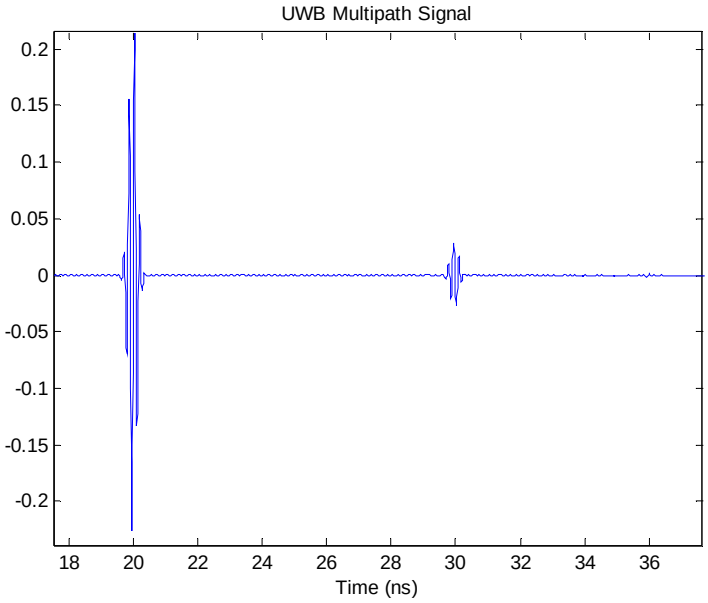

Figure 5.18 UWB Multipath Signals after Applying a Hanning Window

Figure 5.19 shows the results of the performing simulations with the above multipath signal. The simulations were run assuming perfect knowledge of the paths after the transform domain processing. As shown the processing severely attenuates the last two multipath components. The second multipath component is barely noticeable and the third component is no longer noticeable. This results in the receiver being unable to use all the paths that were initially available. This is shown in the plot where only two paths are available for use after cancellation. Also the two finger case does not offer much of an improvement over the 1 finger case.

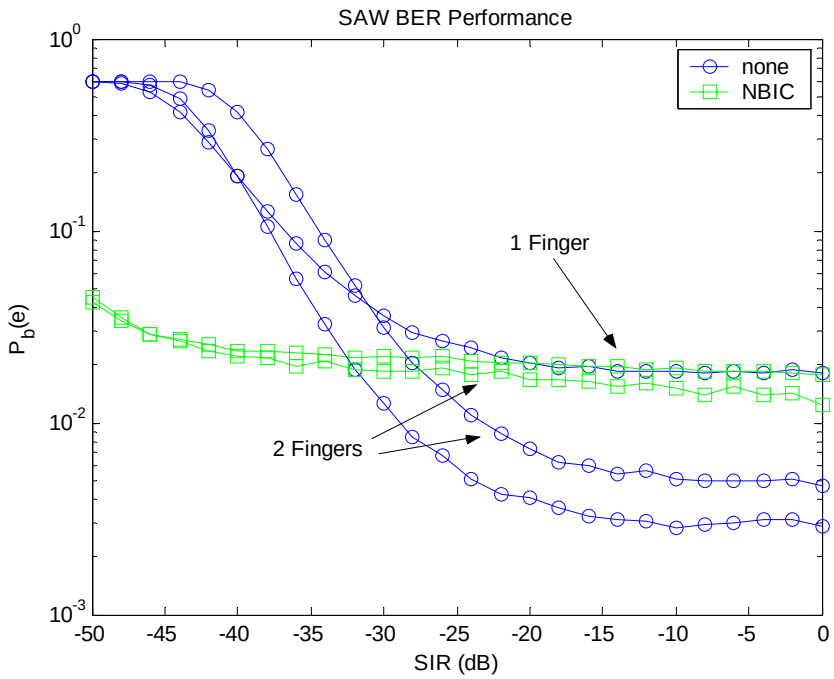

Figure 5.19 BER Performance for 3 Finger UWB Rake Receiver

Note also that these simulations were conducted with the interferer's center frequency equal to the UWB signal's center frequency. This represents a worse case scenario as this frequency will be the most detrimental to system performance. As shown in Chapter 3, as the narrowband interferer's center frequency moves further away from the UWB signal's center frequency the impact of the interferer lessens.

5.7 Conclusion

The analog nature of the transform domain circuit makes it attractive for UWB systems. For an environment with AWGN and narrowband interference simulation results show that a significant improvement can be achieved in terms of error performance. However it was found that to achieve satisfactory performance windowing must be performed. The windowing reduces the interferer's sidelobes in the "frequency" domain and allows the inverse transform of the UWB pulse to be more accurate after cancellation. However this also requires that the UWB signal be positioned close to the center of the modulating chirp window. This is required because these windowing functions inherently reduce the amplitude of the signal near the edges of the transform domain processing window. Since this amplitude reduction is observed in the time domain, this could cause problems in a multipath or single path scenario. This was demonstrated using the simple multipath simulation in Section 5.6. The rectangular window does not suffer from this, however the hard limiting cancellation leaves some residual interference near the edges of transform domain processing window and does a poor job of reproducing the UWB signal. Lastly a major challenge is to find devices suitable for performing the chirp Fourier transform. It is not believed that SAW chirp filters can achieve the necessary

center frequencies for the UWB signal and there is no active commercial market for these devices. Note that the bandwidths and center frequencies are limited by the materials used to make the SAW devices. There is literature concerning superconductive filters, which have higher center frequencies and bandwidths, and are capable of performing chirp Fourier transforms. However these devices do not appear to be in the commercial market. Note that it is possible that this technique may be applicable to optical processing.

Chapter 6 Conclusions and Future Work

This thesis presents analysis of two very relevant UWB topics, channel modeling and interference cancellation. The channel modeling work builds on previous results and provides insight for both large and small scale modeling. The narrowband interference cancellation sections analyze two types of front end cancellation circuits, one time domain and one frequency domain technique.

General background information on ultra-wideband was presented in Chapter 1, covering pulses, modulation, multiple access, and current FCC regulations. Chapter 3 provided background information on interference and previously researched techniques for mitigating interference. The majority of the presented background research covered topics initially suggested for spread spectrum communications with the thought that these techniques could also be applied to UWB. Some background was given for UWB techniques as well, although there are far fewer articles as of yet.

Chapter 2 presented the results pertaining to channel modeling. The NLOS measurement campaign and the data processing methodologies were described for the large and small scale results. The large scale work mainly focused on frequency dependent path loss and ultimately concluded that UWB may exhibit some dependency due to the antennas but that the channel is not frequency dependent (Note that it is possible that certain materials could cause pulse distortion). The data's path loss exponent and standard deviations were calculated and compared with preciously reported results. The values matched reasonably well.

The small scale analysis also presented traditional statistical calculations, such as RMS dealy spread, mean excess dealy, and max excess delay. These results were compared with previously reported values and were found to match reasonably well. Further analysis looked at the statistical distribution of the small scale statistics. Comparing the CDFs it was found that the small statistics in general adhere to a Gaussian distribution.

Chapter 4 looked at the time domain NBIC technique. The proposed technique attempts to estimate the narrowband interferer in the digital domain and cancel it in the analog domain. This allows sampling to be commensurate with the narrowband signal. Two cancellation algorithms were investigated, an LMS algorithm and a transversal filter. The LMS circuit was determined to be inadequate for cancellation because of its slow convergence. The cancellation circuit offered no significant gains in the presence of a modulated interferer. However the transversal filter performed very well and has some promise. It was found to offer significant gains in both an AWGN and multipath channel in the presence of a modulated interferer. Future work in this area would include characterization of a transversal filter with an adaptive weight update parameter, μ. Using the signal's autocorrelation matrix to estimate INR for this purpose was briefly

discussed. Further investigations of the effects of filter length and sampling rate would also be of use.

Chapter 4 also investigated two frequency estimation techniques, a method of moments and a maximum likelihood estimation algorithm. These techniques were both capable of estimating the frequency of a tone, however there were some tradeoffs. The maximum likelihood estimation performs better than the method of moments estimation but suffers from being much more computationally intensive. The method of moments on the other hand suffers from a higher variance and a worsening performance with increased sampling rate. If the inverse matrix computation required by the MLE can be tolerated it is the definite choice. Future work in this area would include looking into the performance of other frequency estimation techniques, possibly in the frequency domain and possibly analog.

Lastly, in Chapter 5 the frequency domain cancellation technique, transform domain processing, was discussed. Transform domain processing uses a chirp Fourier transform to facilitate cancellation. The chirp Fourier transform produces the spectrum of the inputted signal as function of time. This allows the interference to be mitigated in the "frequency" domain by limiting its power. The results determined that it is possible to achieve significant performance improvement using transform domain processing. However it was also found that there are some limitations. First there are limitations on SAW filter technology that currently make it inapplicable to UWB. Also it was found that to achieve reasonably good performance windowing must be performed. Windowing causes attenuation in the time domain and possibly causes loss of signal energy if the transform is not properly synchronized. Future work could include determining other means of implementing the chirp Fourier transform besides using SAW technology. Also performing synchronization in the transform window could be investigated.

References

[Alva03] A. Alvarez, G. Valera, M. Lobeira, R. Torres, and J. L. Garcia, "New Channel Impulse Response Model for UWB Indoor System Simulations," *The 57th IEEE Semiannual*, vol. 1, pp. 22–25 , April 2003.

[Boub03] N. Boubaker and K. B. Letaif, "A Low Complexity MMSE-RAKE Receiver in a Realistic UWB Channel and in the Presence of NBI," *IEEE*, pp. 233 – 137, 2003.

[Bueh03] R. M. Buehrer, W. Davis, A. Safaai-Jazi, and D. Sweeney, "Characterization of the Ultra-Wideband Channel," *2003 IEEE Conference on Ultra-Wideband Systems and Technologies*, pp. 26–31, Nov. 2003.

[Bueh04] R.M. Buehrer, W.A. Davis, A. Safaai-Jazi, and D. Sweeney, "Ultra-wideband Propagation Measurements and Modeling," DARPA NETEX Program Final Report, Jan. 2004.

[Cass01] D. Cassioli, M Z. Win, and A. F. Molisch, "A Statistical Model for the UWB Indoor Channel," in *Proc. IEEE VTS 53rd Vehicular Technology Conference*, vol. 2, pp. 1159–1163 , May 2001.

[Cass02] D. Cassioli, M.Z. Win, and A. F.Molisch, "The Ultra-Wide Bandwidth Indoor Channel: From Statistical Study to Simulations," *IEEE Journal on Selected Areas in Communications*, vol. 20, no. 6 , pp. 1247–1257, Aug. 2002

[Cram99] R. J.-M. Cramer, R. A. Scholtz, and M. Z. Win, "Spatio-Temporal Diversity in Ultra-wideband Radio," in *Proc IEEE Wireless Communications and Networking Conference*, vol. 2, pp. 888-892, 1999.

[Cram00] R.J.-M. Cramer, "An Evaluation of Ultrawideband Propagation Channels", PhD Dissertation, Dept. Elect. Eng., Univ. of Southern Calif., Los Angeles, CA, Dec. 2000.

[Cram02a] R. J.-M. Cramer, R. A. Scholtz, and M. Z. Win, "Evaluation of an Ultra-Wide-Band Propagation Channel," *IEEE Transactions on Antennas and Propagation*, vol. 50, no. 5, pp. 561–570, May 2002.

[Cram02b] R. J.-M. Cramer, R. A. Scholtz, and M. Z. Win , "Evaluation of an Indoor Ultra-Wideband Propagation Channel (doc.: IEEE P802.15-02/286-SG3a and IEEE P802.15-02/325-SG3a)," submitted to IEEE P802.15 Working Group for Wireless Personal Area Networks (WPANs), June 2002. Available: http://grouper.ieee.org/groups/802/15/pub/2002/Jul02/

[Donl04a] B. M. Donlan, S. Venkatesh, V. Bharadwaj, R. M. Buehrer, and J.-A. Tsai, "The Ultra-Wideband Indoor Channel," *IEEE Vehicular Technology Conference,* 2004.

[Donl04b] B. M. Donlan, D. R. McKinstry, and R. M. Buehrer, "The UWB Indoor Channel: Large and Small Scale Modeling," Submitted to *IEEE Transactions on Wireless Communications*, Sept 2004.

[Donl05] B. M. Donlan, R. M Buehrer and J. H. Reed, "Ultra-Wideband Wireless Systems," *Encyclopedia of RF and Microwave Engineering*, Hoboken, NJ: Wiley, 2005.

[FCC] Federal Communications Commission, First Report and Order, ET Docket 98-153, April 2002.

[Foer02a] J. Foerster, "Channel Modeling Sub-committee Report Final (doc.: IEEE 802-15-02/490r1-SG3a)," submitted to IEEE P802.15 Working Group for Wireless Personal Area Networks (WPANs), Feb. 2002. Available: http://grouper.ieee.org/groups/802/15/pub/2002/Nov02/

[Foer02b] J. Foerster and Q. Li, "UWB Channel Modeling Contribution from Intel (doc: IEEE P802.15-02/279-SG3a)," submitted to IEEE P802.15 Working Group for Wireless Personal Area Networks (WPANs), June 2002. Available: http://grouper.ieee.org/groups/802/15/pub/2002/Jul02/.

[Gart92] L. M. Garth and H. V. Poor, "Narrowband Interference Suppression in Impulsive Channels," *IEEE Transactions on Aerospace and Electronic Systems*, vol. 28, no. 1, pp. 15–34, Jan.1992.

[Ghas02a] S. S. Ghassemzadeh, L. J. Greenstein, and V. Tarokh, "The Ultra-wideband Indoor Multipath Loss Model (doc: IEEE P802.15-02/282-SG3a and IEEE P802.15-02/283-SG3a)," submitted to IEEE P802.15 Working Group for Wireless Personal Area Networks (WPANs), June 2002. Available: http://grouper.ieee.org/groups/802/15/pub/2002/Jul02/.

[Ghas02b] S. S. Ghassemzadeh, R. Jana, C. W. Rice, W. Turin, and V. Tarokh, "A Statistical Path Loss Model for In-Home UWB Channels," *2002 IEEE Conference on Ultra Wideband Systems and Technology*, pp. 59–64.

[Ghas03] S. S. Ghassemzadeh, Vahid Tarokh, "UWB Path Loss Characterization In Residential Environments," *2003 IEEE Radio Frequency Integrated Circuits Symposium*, pp. 501–504.

[Hash93] H. Hashemi, "The Indoor Radio Propagation Channel," *Proceedings of the IEEE*, vol. 81, no. 7, pp. 943–968 , July 1993.

[Hogb74] J.A. Hogbom. "Aperture Synthesis with a Non-Regular Distribution of Interferometer Baselines", *Astron. and Astrophys. Suppl. Ser,* vol. 15,1974.

[Hovi02] V. Hovinen, et. al., "A proposal for a selection of indoor UWB path loss model, http://grouper.ieee.org/groups/802/15/pub/2002/Jul02, 02280r1P802.15.

[Hsu78] F. M. Hsu and A. A. Giordano, "Digital Whitening Techniques for Improving Spread Spectrum Communications Performance in the Presence of Narrowband Jamming and Interference," *IEEE Transactions on Communications*, vol. 26, no. 2, pp. 209–216, Feb. 1978.

[Huan99] X. Huang and D. Liang, "Gradual RELAX algorithm for RFI suppression in UWB-SAR," *Electronic Letters*, Vol. 35, no. 22, pp. 1916 – 1917, Oct. 1999.

[Ilti84] R. A. Iltis and L. B. Milstein, "Performance Analysis of Narrow-Band Interference Rejection Techniques in DS Spread-Spectrum Systems," *IEEE Transactions on Communications*, vol. 32, no. 11, pp. 1169–1177, Nov. 1984.

[Juhe99] B. Juhel, G. Vezzosi, and M. Le Goff, "Radio Frequency Interference Suppression for Noisy Ultra Wide Band SAR Measurements," *Ultra-Wideband Short-Pulse Electromagnetics*, pp. 387 – 393, New York: Kluwer Academic/Pienum Publishers, 1999.

[Kay93] S. M. Kay, *Fundamentals of Statistical Signal Processing: Estimation Theory*, Upper Saddle River NJ: Prentice Hall, 1993.

[Ketc82] J. W. Ketchum and J. G. Proakis, "Adaptive Algorithms for Estimating and Suppressing Narrow-Band Interference in PN Spread-Spectrum Systems," *IEEE Transactions on Communications*, vol. 30, no. 5, pp. 913–924, May 1982.

[Kein02a] J. Keignart and N. Daniele, "Subnanosecond UWB Channel Sounding in Frequency and Temporal Domain," *2002 IEEE Conference on Ultra Wideband Systems and Technology*, pp 25–30, May 2002.

[Kein02b] J. Keignart, J. B. Pierrot, N. Daniele, and P. Rouzet, "UWB Channel Modeling Contribution from CEA-LETI and STMicroelectronics (doc: IEEE P802.15-02/444-SG3a)," submitted to IEEE P802.15 Working Group for Wireless Personal Area Networks (WPANs), Oct 2002. Available: http://grouper.ieee.org/groups/802/15/pub/2002/Nov02/.

[Kein03] J. Keignart, N. Daniele," Channel sounding and modeling for indoor UWB communications," *2003 International Workshop on Ultra Wideband Systems*.

[Kino87] G. S. Kino, *Acoustic Waves: Devices, Imaging, & Analog Signal Processing*, Prentice-Hall, NJ, 1987.

[Kuni02] J. Kunisch and J. Pamp, "Measurement Results and Modeling Aspects for the UWB Radio Channel," *2002 IEEE Conference on Ultra-Wideband Systems and Technologies*, pp. 19–23, May 2002.

[Last97] J. D. Laster and J. H. Reed, "Interference Rejection in Digital Wireless Communications," *IEEE Signal Processing Magazine*, vol. 14, no. 3, pp. 37–62, May 1997.

[Lee00] J. Lee and J. Yuan, "Interpolation Lattice Filters for Narrowband Interference Cancellation in PN Spread Spectrum Communications Systems," *IEEE 6th International Symposium on Spread Spectrum Techniques and Applications*, vol. 1, pp. 107–111, Sept. 2000.

[Li82] L. Li and L. B. Milstein, "Rejection of Narrow-Band Interference in PN Spread-Spectrum Systems Using Transversal Filters," *IEEE Transactions on Communications*, vol. 30, no. 5, pp. 925–928, May 1982.

[Li96] J. Li and P. Stoica, "Efficient Mixed-Spectrum Estimation with Applications to Target Feature Extraction," *IEEE Transactions on Signal Processing*, vol. 44, no. 2, pp. 281 – 295, Feb. 1996.

[Licu03] S. Licul, W. A. Davis, and W. L. Stutzman, "Ultra-Wideband (UWB) Communication Link Modeling and Characterization," *2003 IEEE Conference on Ultra-Wideband Systems and Technologies*, pp. 310–314, Nov. 2003.

[Ligh03] A. H. Light, "NETEX Task 1: Measured Effects of Ultrawideband (UWB) Emitters on Existing Narrowband Military Receivers," *2003 IEEE Conference on Ultra-Wideband Systems and Technologies*, pp. 10–14, Nov. 2003.

[Mart02] C. J. Le Martret, and G. B. Giannakis, "All-Digital Impulse Radio With Multiuser Detection for Wireless Cellular Systems," *IEEE Transactions on Communications*, vol. 50, no. 9, pp. 1440–1450, Sept. 2002.

[McKi03a] D. R. McKinstry, "Ultra-Wideband Small Scale Channel Modeling and its Application to Receiver Design," Master's Thesis, Dept. of Electrical and Computer Engineering, Virginia Tech, Blacksburg, VA, 2003.

[McKi03b] D. R. McKinstry and R. M. Buehrer, "LMS Analog and Digital Narrowband Rejection System for UWB Communications," *2003 IEEE Conference on Ultra-Wideband Systems and Technologies*, pp. 91–95, Nov. 2003.

[Mils77] L. B. Milstein and P. K. Das, "Spread Spectrum Receiver Using Surface Acoustic Wave Technology," *IEEE Transactions on Communications*, vol. 25, no. 8, pp. 841-847, Aug. 1977.

[Mils80] L. B. Milstein and P. K. Das, "An Analysis of a Real-Time Transform Domain Filtering Digital Communication System – Part I: Narrow-Band Interference Rejection," *IEEE Transactions on Communications*, vol. 18, no. 6, pp. 816–824, June 1980.

[Mils86] L. B. Milstein and R. A. Iltis, "Signal Processing for Interference Rejection in Spread Spectrum Communications," *IEEE ASSP Magazine*, vol. 3, no. 2, pp. 18–31, April 1986.

[Mils88] L. B. Milstein, "Interference Rejection Techniques in Spread Spectrum Communications," *Proceedings of the IEEE*, vol. 76, no. 6, pp.657-671, June 1988.

[Muqa03a] A. H. Muqaibel, A. Safaai-Jazi, A. M. Attiya, A. Bayram, and S. M. Riad, "Measurements and Characterization of Indoor Ultra-Wideband Propagation," *2003 IEEE Conference on Ultra-Wideband Systems and Technologies*, pp 295–299, Nov. 2003.

[Muqa03b] Muqaibel, A.; Safaai-Jazi, A.; Bayram, A.; Riad, S.M.; "Ultra wideband material characterization for indoor propagation", *2003 IEEE Antennas and Propagation Society International Symposium*, vol. 4, pp. 623–626.

[Odli] P. Odling, P. O. Borjesson, T. Magesacher, and T. Nordstrom, "An Approach to Analog Mitigation of RFI," *IEEE Journal on Selected Areas in Communications*, vol. 20, no. 5, pp. 974 – 986, June 2002.

[Paga03] P. Pagani, P. Pajusco, and S. Voinot, "A study of the ultra-wideband indoor channel: Propagation experiment and measurement results," in COST273., TD(030)060, Jan. 2003.

[Papo02] A. Papoulis, and S. Unnikrishna Pillai, *Probability, Random Variables, and Stochastic Processes*. Fourth Edition, Boston, MA: McGraw Hill, 2002.

[Pend02] M. Pendergrass and W. Beeler, "Empirically Based Statistical Ultra-Wideband (UWB) Channel Model (doc.: IEEE 802-15-02/240SG3a)," presented to IEEE P802.15 Working Group for Wireless Personal Area Networks (WPANs), June 2002. Available: http://grouper.ieee.org/groups/802/15/pub/2002/Jul02/

[Pret02] C. Prettie, D. Cheung, L. Rusch, and M. Ho, "Spatial Correlation of UWB Signals in a Home Environment," *2002 IEEE Conference on Ultra Wideband Systems and Technology*, pp. 65–69, May 2002.

[Proa96] J. G. Proakis, "Interference Suppression in Spread Spectrum Systems," *IEEE 4th International Symposium on Spread Spectrum Technology and Applications*, vol. 1, pp. 259–266, 1996.

[Qui02] R. C. Qui, "A Study of the Ultra-Wideband Wireless Propagation Channel and Optimum UWB Receiver Design," *IEEE Journal on Selected Areas in Communications*, vol. 20, no. 9, pp. 1628-1637, Dec. 2002.

[Rapp02] T.S. Rappaport, Wireless *Communications: Principles and Practice*, Second Edition, Upper Saddle River, NJ: Prentice Hall, 2002.

[Reed04] J. H. Reed, Ed., *An Introduction to Ultra Wideband Communication Systems*, Prentice-Hall, forthcoming.

[Rusc94] L. A. Rusch and H. V. Poor, "Narrowband Interference Suppression in CDMA Spread Spectrum Communications," *IEEE Transactions on Communications*, vol. 42, No. 2/3/4, pp. 1969–1979, February/March/April 1994.

[Rusc03] L. Rusch, C. Prettie, D. Cheung, Q. Li, M. Ho, "Characterization of UWB Propagation from 2 to 8 GHz in a Residential Environment," *IEEE Journal on Selected Areas in Communications*, submitted for publication

[Scha03] H. G. Schantz, "Introduction to Ultra-Wideband Antennas," *2003 IEEE Conference on Ultra-Wideband Systems and Technologies*, pp. 1–9, Nov. 2003.

[Scho98] R.A. Scholtz, M.Z. Win, J.M. Cramer, "Evaluation of the Characteristics of the Ultra-Wideband Propagation Channel," *1998 Antennas and Propagation Society International Symposium*, vol.2, pp.626–630.

[Seid92] S.Y. Seidel and T.S. Rappaport, "914 MHz Path Loss Prediction Models for Indoor Wireless Communications in Multi-floored Buildings," *IEEE Transactions on Antennas and Propagation*, vol. 40, no. 2, pp. 207-217, Feb. 1992.

[Silv03] C. da Silva and L. B. Milstein, "Spectral-Encoded UWB Communication Systems," *2003 IEEE Conference on Ultra-Wideband Systems and Technologies*, pp. 96-100, Nov. 2003.

[Turi72] G. L. Turin, F. D. Clapp, T. L. Johnston, S. B. Fine, and D. Lavry, "A Statistical Model of Urban Multipath Propagation," *IEEE Transactions on Vehicular Technology*, vol. VT-21, pp. 1-9, Feb. 1972.

[Venka04] S. Venkatesh, J. Ibrahim, and R. M. Buehrer, "A New 2-Cluster Model for Indoor UWB Channel Measurements," Presented at 2004 *IEEE International Symposium on Antennas and Propagation*, June 2004.

[Vija90] R. Vijayan and H. V. Poor, "Nonlinear Techniques for Interference Suppression in Spread Spectrum Systems," *IEEE Transactions on Communications*, vol. 38, no. 7, pp. 1060–1065, July 1990.

[With99] P. Withington, R. Reinhardt, and R. Stanley, "Preliminary Results of an Ultra-wideband (Impulse) Scanning Receiver," *1999 IEEE Military Communications Conference*, vol. 2, pp. 1186-1190.

[Yano02] S.M. Yano, "Investigating the Ultra-Wideband Wireless Channel," *IEEE 55th Vehicular Technology Conference*, pp. 1200–1204, May 2002.

[Zaso03] T. Zasowski, F. Althaus, M. Stager, A. Wittneben, And G. Troster, "UWB for Noninvasive Wireless Body Area Networks: Channel Measurements and Results," *2003 IEEE Conference on Ultra-Wideband Systems and technologies*, pp. 285-289, Nov 2003.

Vita

Brian Michael Donlan was born in Columbia, SC on November 17, 1979. He attended Clemson University from August 1998 to May 2002. In May 2002 he graduated with a Bachelor of Science degree in Electrical Engineering. At Clemson he was a Clemson Presidential Scholar, Clemson Sonoco Scholar, and a South Carolina Palmetto Scholar. From August 2002 to May 2004 he attended Virginia Polytechnic Institute and State University where he was a Bradley Fellow in the Department of Electrical and Computer Engineering. He was also a student of the Mobile and Portable Radio Research Group (MPRG) at Virginia Tech. His interest includes digital communications and wireless communications.